

**The Interaction Network of Lipids,
Peptides, and Receptors in Neuronal
Processes**

Inaugural-Dissertation

zur Erlangung des Doktorgrades
der Mathematisch-Naturwissenschaftlichen Fakultät der
Heinrich-Heine-Universität Düsseldorf

vorgelegt von

Marcel Falke

aus Lennestadt

Düsseldorf, Mai 2020

aus dem Institut für Physikalische Biologie
der Heinrich-Heine-Universität Düsseldorf

Gedruckt mit der Genehmigung der
Mathematisch-Naturwissenschaftlichen Fakultät der
Heinrich-Heine-Universität Düsseldorf

Berichtersteller:

1. Dr. Manuel Etzkorn

2. Prof. Dr. Karl-Erich Jaeger

Tag der mündlichen Prüfung: 17.07.2020

“We start off confused and end up confused on a higher level.”
Alan Francis Chalmers

Contents

| | |
|---|------------|
| List of Figures | iii |
| List of Tables | v |
| Abstract | 1 |
| Zusammenfassung | 3 |
| 1 General Introduction | 5 |
| 1.1 G protein-coupled receptors | 5 |
| 1.2 Melanocortin-4 receptor | 5 |
| 1.3 Signal transduction by MC4R | 6 |
| 1.4 cAMP kit for assaying GPCR activation | 7 |
| 1.5 Membrane protein solubilization and stabilization | 8 |
| 1.6 Recombinant protein expression in insect cells | 10 |
| 1.7 α -Synuclein and Parkinson's disease | 12 |
| 1.8 Regulation of EGFR | 13 |
| 1.9 Scope and objectives | 14 |
| 2 Insights into Hormone - GPCR Interactions: Enhancing eukaryotic MC4R ex- pression for structural studies | 17 |
| 2.1 Abstract | 17 |
| 2.2 Introduction | 17 |
| 2.3 Material and Methods | 19 |
| 2.4 Results and Discussion | 20 |
| 2.5 Conclusion | 30 |
| 3 Characterization of lipocalin 2 and its interaction with MC4R | 33 |
| 3.1 Abstract | 33 |
| 3.2 Introduction | 33 |
| 3.3 Material and Methods | 34 |
| 3.4 Results and Discussion | 37 |
| 3.5 Conclusion | 42 |
| 4 SMALPs as a tool for lipid-peptide interaction | 45 |
| 4.1 Abstract | 45 |
| 4.2 Introduction | 45 |
| 4.3 Material and Methods | 46 |
| 4.4 Results and Discussion | 46 |
| 4.5 Conclusion | 49 |

| | | |
|----------|--|------------|
| 5 | Interaction of α-Synuclein with α-Synuclein-derived lipoparticles | 51 |
| 5.1 | Publication information | 51 |
| 5.2 | Abstract | 51 |
| 5.3 | Introduction | 51 |
| 5.4 | Materials and Methods | 53 |
| 5.5 | Results and Discussion | 57 |
| 5.6 | Conclusion | 65 |
| 6 | Interaction of ARNO-Sec7 with juxtamembrane segment of EGFR | 67 |
| 6.1 | Publication Information | 67 |
| 6.2 | Abstract | 67 |
| 6.3 | Introduction | 68 |
| 6.4 | Results and Discussion | 69 |
| 6.5 | Conclusion | 77 |
| 6.6 | Material and Methods | 78 |
| | Conclusion and key achievements | 87 |
| | List of publications | 89 |
| | Supplementary data | 91 |
| | Bibliography | 103 |
| | List of Abbreviations | 127 |
| | Danksagung | 129 |
| | Erklärung | 131 |

List of Figures

| | | |
|-----|--|----|
| 1.1 | Schematics of MC4R signal transduction | 6 |
| 1.2 | Principle of FRET-based cAMP detection. | 8 |
| 1.3 | Membrane-mimetic systems for membrane protein stabilization | 9 |
| 1.4 | Overview of the Bac-toBac™ Baculovirus protocol | 12 |
| 1.5 | Summarizing scheme of this PhD thesis. | 14 |
| 2.1 | MC4R expression in different cell types. | 21 |
| 2.2 | MC4R expression optimization in <i>Tnao38</i> cells. | 22 |
| 2.3 | Optimization of assay parameters for performance of cAMP HTRF assay in HEK293 cells. | 23 |
| 2.4 | Amino acid sequence of classical melanocortin ligands. | 24 |
| 2.5 | Ligand selectivity of MC4R. | 25 |
| 2.6 | Functional characterization of MC4R in insect cells. | 26 |
| 2.7 | Solubilization of <i>Tnao38</i> membranes containing MC4R. | 28 |
| 2.8 | Purification of MC4R-SMALPs. | 30 |
| 3.1 | GST-hLCN2 construct, purification and functional characterization | 37 |
| 3.2 | SUMO-hLCN2 construct, purification and functional characterization. | 38 |
| 3.3 | Protein sequence alignment of human and murine LCN2 | 39 |
| 3.4 | Functional characterization of murine LCN2 in HEK293-MC4R cells. | 40 |
| 3.5 | Structural comparison of human and murine LCN2 | 41 |
| 4.1 | Preparation and characterization of SMALPs | 47 |
| 4.2 | Binding of ACTH to SMALPs. | 48 |
| 5.1 | Preparation and characterization of α Syn-LiPs | 58 |
| 5.2 | α Syn-LiPs in direct comparison to classical MSP-derived nanodiscs as a tool in aggregation assays. | 61 |
| 5.3 | α Syn-LiPs properties after SEC elution. | 62 |
| 5.4 | α Syn-LiPs can induce primary nucleation. | 63 |
| 5.5 | Sample properties at the end of the aggregation assays. | 64 |
| 6.1 | JM-Sec7 interaction as seen from the EGFR-JM side. | 70 |

List of Figures

| | | |
|------|--|-----|
| 6.2 | JM-Sec7 interaction as seen from the ARNO-Sec7 side. | 72 |
| 6.3 | JM-membrane interaction depends on anionic lipid content and follows a similar pattern as Sec7 binding with distinct differences. | 74 |
| 6.4 | Calmodulin (CaM) and ARNO-Sec7 share same binding site and compete for EGFR-JM binding <i>in vitro</i> | 75 |
| 6.5 | The interplay between possible modulators acting on EGFR-JM as central interface in the intracellular interaction network of the EGFR. | 76 |
| 6.6 | Solubilization screen of MC4R using Dot blot | 91 |
| 6.7 | Protein sequence alignment of human and murine MC4R | 92 |
| 6.8 | Verification of LCN2 refolding by NMR | 93 |
| 6.9 | Functional characterization of murine LCN2 in HEK293T-MC4R cells by Reporter Gene assay | 94 |
| 6.10 | FTIR data of α Syn-LiPs after SEC. | 95 |
| 6.11 | Preparative SEC data of freshly prepared α Syn-LiPs assembled with POPC (red) or POPG (blue) lipids. | 95 |
| 6.12 | DLS data of POPG α Syn-LiPs after SEC. | 96 |
| 6.13 | related to Fig. 6.1 and Fig. 6.2. | 97 |
| 6.14 | related to Fig. 6.2. | 98 |
| 6.15 | related to Fig. 6.3. | 99 |
| 6.16 | related to Fig. 6.4. | 100 |
| 6.17 | related to Fig. 6.2 and Fig. 6.5. Speculative model of known factors that could promote a potential ARNO-EGFR interaction <i>in vivo</i> | 101 |

List of Tables

| | | |
|-----|---|----|
| 3.1 | List of LCN2 constructs and PCR primers. | 35 |
| 6.1 | Acquisition parameters of the spectra used for Sec7 resonance assignment. . . . | 82 |
| 6.2 | Acquisition parameters of the spectra used for JM resonance assignment. | 82 |

Abstract

A large number of cellular processes is regulated by a complex interplay between several hormones, membrane-embedded proteins and lipids. Especially G protein-coupled receptors (GPCRs) are one of the most essential classes of pharmacological targets and analysis of GPCR structure, function, and organization is one of the major challenges in molecular biology. Membrane biochemistry has benefited in the past from improvements both in terms of sample preparation (protein expression and purification) and biophysical characterization. However, finding a suitable membrane mimetic system for membrane protein stabilization as well as for interaction studies with peptides remains still challenging.

This work explores approaches to overcome these limitations as demonstrated for the GPCR melanocortin-4 receptor (MC4R) which is known to play an important role in energy homeostasis and most cases of monogenic obesity. Eukaryotic MC4R expression (human and insect cells) was established to enable insights into the dynamic processes of MC4R-hormone interactions. Contrary to previous reports, our data suggest that bone-derived hormone lipocalin 2 does not activate MC4R.

With the aim to find a suitable membrane mimetic system for isolation of MC4R, we demonstrate detergent-free reconstitution of the receptor into styrene-maleic acid (SMA) lipid particles without removal from its native lipid environment. We further make use of the capability of the amphiphilic SMA copolymer to form lipid particles (SMALPs) out of synthetic lipids to characterize peptide-lipid interaction.

In a similar way, we investigated the effect of membrane-binding on aggregation of the amyloidogenic peptide α -Synuclein (α Syn). We show that α Syn-lipid particles (α Syn-LiPs) are able to effectively induce, accelerate or inhibit α Syn aggregation emphasizing α Syn-LiPs as additional tool to study various aspects of α Syn amyloid fibril formation.

Finally, we investigate interaction as well as binding modes of different epidermal growth factor receptor (EGFR) modulators in connection with nanodisc system enabling us to generate a network of possible EGFR modulators acting on the intracellular domain of the receptor.

Zusammenfassung

Eine Vielzahl an zellulären Prozessen wird durch ein komplexes Zusammenspiel aus verschiedenen Hormonen, Membranproteinen und Lipiden reguliert. Insbesondere G-Proteingekoppelte Rezeptoren (GPCRs) stellen eine der wichtigsten Klasse an pharmakologischen Zielen dar und die Untersuchung der GPCR-Struktur, -Funktion und -Organisation ist eine der großen Herausforderungen der Molekularbiologie. Die Membranbiochemie hat in den letzten Jahren von den Verbesserungen sowohl in der Probenvorbereitung (Proteinexpression und -aufreinigung) als auch in der biophysikalischen Charakterisierung profitiert. Trotzdem bleibt die Suche nach einem passenden biomembranähnlichen System für die Stabilisierung von Membranproteinen und für Interaktionsstudien mit Peptiden eine große Herausforderung.

Diese Arbeit untersucht Ansätze zur Lösung dieser Limitierungen am Beispiel des GPCRs Melanocortin-4-Rezeptor (MC4R), welcher eine wichtige Rolle in der Energiehomöostase und in den meisten Fällen von monogener Fettleibigkeit spielt. Die Expression von MC4R wurde in eukaryotischen Expressionssystemen (humane und Insektenzellen) etabliert mit dem Ziel, Einblicke in die dynamischen Prozesse der MC4R-Hormon Interaktion zu bekommen. Im Gegensatz zu vorherigen Berichten deuten unsere Daten darauf hin, dass das von Knochen stammende Hormon Lipocalin 2 nicht zur Aktivierung von MC4R führt.

Mit dem Ziel, eine passende Membranumgebung zur Isolierung von MC4R zu finden, demonstrieren wir die Rekonstitution des Rezeptors in Styrol-Maleinsäure (SMA) Lipidpartikel ohne ihn dabei aus seiner Lipidumgebung zu entfernen. Weiterhin machen wir uns die Fähigkeit des amphiphilen SMA Copolymers zur Bildung von Lipidpartikeln aus synthetischen Lipiden zu Nutze, um die Interaktion von Peptiden und Lipiden zu charakterisieren.

Auf ähnliche Weise haben wir den Effekt der Membranbindung auf die Aggregation des amyloidogenen Peptids α -Synuclein (α Syn) untersucht. Wir zeigen, dass α Syn Lipidpartikel (α Syn-LiPs) dazu in der Lage sind, die α Syn Aggregation effektiv entweder zu induzieren, zu beschleunigen oder zu blockieren, was die Relevanz von α Syn LiPs als zusätzliches Werkzeug in verschiedenen Aspekten der α Syn Fibrillenbildung unterstreicht.

Schließlich untersuchen wir die Interaktion und Bindemodi von verschiedenen Epidermal Growth Factor Receptor (EGFR) Modulatoren in Verbindung mit der Nanodisc-Technologie, was es uns erlaubt, ein Netzwerk möglicher EGRF Modulatoren, die auf die intrazelluläre Domäne des Rezeptors wirken, zu bilden.

1 General Introduction

1.1 G protein-coupled receptors

G protein-coupled receptors (GPCRs) are cell surface molecules embedded in the plasma membrane. Due to their ability to detect either physical (e.g. light) or in most cases chemical (e.g. hormones, neurotransmitters) stimuli, GPCRs are responsible for a large number of cellular responses to external signals [1]. They represent the largest and most diverse class of integral membrane proteins with almost 800 GPCRs encoded by the human genome, of which 460 are predicted to be olfactory receptors [2]. Despite this large variety, GPCRs share in common seven transmembrane helices of around 25 to 35 amino acids linked by extracellular and intracellular loops.

Upon binding of different ligands, such as organic molecules, peptides or proteins, GPCRs transmit the signal from the extracellular space of the cell to the cytosol by coupling to guanine triphosphate binding proteins (G-proteins). Ligands can either activate (agonist) or block (antagonist) the receptor. Some ligands act as an inverse agonists, they decrease the basal activity of the receptor.

Based on sequential and structural similarities, GPCRs can be divided into five main families: the rhodopsin family (701 members), the adhesion family (24 members), the frizzled/taste family (24 members), the glutamate family (15 members), and the secretin family (15 members) [2,3].

Their central role as well as their position on the cell surface, makes them a highly attractive target for pharmaceutical drugs. Approximately 50% of all modern drugs on the market are targeting GPCRs [4,5]. Remarkably, these drugs target only 5% of receptors, which highlights the pharmaceutical impact of GPCRs [6]. In the past years, much progress has been made in the structural characterization of membrane proteins. However, structures of membrane proteins are still largely underrepresented and it is crucial to further investigate their structural biology.

1.2 Melanocortin-4 receptor

The melanocortin-4 receptor (MC4R) is one of the five known melanocortin receptors and member of the G protein-coupled receptor (GPCR) family. Despite also being found in peripheral tissue, MC4R is predominantly expressed in the brain and therefore together with MC3R referred to as neural MCRs [7]. The physiological functions of MC4R include regulation of body weight via regulation of appetite as well as energy homeostasis, making it a potential therapeutic target in both anorexia and obesity [8–10].

The central agonists of MC4R belong to the melanocortin family, namely α -, β -, γ -melanocyte-stimulating hormone (MSH) and adrenocorticotrophic hormone (ACTH) which all result from post-translational processing of proopiomelanocortin (POMC) [7]. All ligands share in common a conserved tetrapeptide sequence His₆-Phe₇-Arg₈-Trp₉ [10–15], which is essential for receptor

activation [16,17]. Recently, constitutive MC4R activation by its own N-terminus was shown [18]. Unique to the melanocortin family is that they have endogenous inverse agonists for their target receptors, such as Agouti-related Protein (AGRP) and Agouti signaling proteins (ASIP).

Pathogenic mutations in the MC4R gene have been described as the most common monogenic cause of obesity [19]. Increased MC4R signaling is thought to cause a negative energy balance resulting in decrease in body weight despite the initial identification of activating mutations of MC4R in obese patients [20].

1.3 Signal transduction by MC4R

GPCR signaling can be seen as a three-component system consisting of a seven-transmembrane-domain receptor, a trimeric G-protein complex (G_{α} , G_{β} , G_{γ}) and an effector. After activation, GPCRs transmit information either by regulation of cyclic adenosine monophosphate (cAMP) or by changing the concentration of Ca^{2+} whose accumulation is triggered by inositol-1,4,5-triphosphate (IP3) [21]. Melanocortins are capable of triggering a broad range of signaling pathways upon activation [22, 23] from which the cAMP-stimulative $G_{\alpha s}$ -protein-signaling cascade is the most dominant. Activation of this type of G-protein subunit leads to an increase of cAMP upon GPCR stimulation. A schematic overview of the MC4R activation pathway is shown in Figure 1.1.

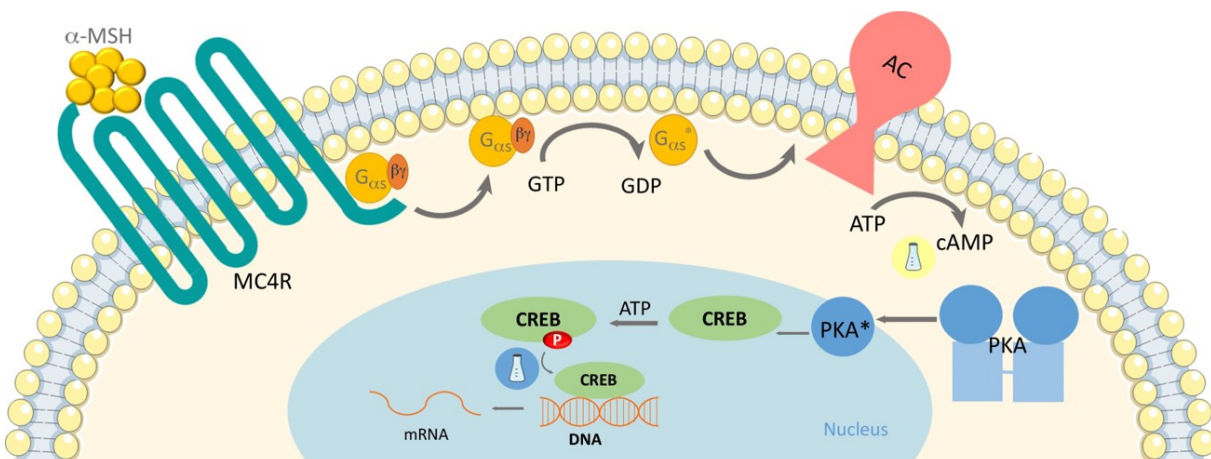


Figure 1.1: Schematics of MC4R signal transduction. Binding of alpha-melanocyte-stimulating hormone (α -MSH) to MC4R leads to activation of heterotrimeric G-proteins and subsequent dissociation of $G_{\alpha s}$ subunit. Activation of adenylyl cyclase (AC) leads to an increase in cAMP that triggers protein kinase A (PKA) mediated changes in gene expression via activation of cAMP response element-binding protein (CREB). The readout possibilities of GPCR activation are indicated by Erlenmeyer flasks and will be discussed in more detail in the next chapter. Figure adapted from [24]

Binding of an external signaling molecule, such as α -MSH, to MC4R leads to a conformational change of the receptor which in turn triggers the coupling of MC4R to the heterotrimeric

stimulatory G protein ($G_{\alpha s}$). Subsequent dissociation of $G_{\alpha s}$ leads to the activation of adenylyl cyclase (AC) enzymes, which convert ATP to cAMP. cAMP is capable of activating several classes of effector molecules [25]. The best characterized effectors of cAMP are the cAMP-dependent protein kinases. Increased cAMP levels lead to activation of protein kinase A (PKA) which results in the dissociation of the catalytic unit of PKA. Active PKA subunit translocates into the nucleus and regulates transcription by phosphorylation of the transcription factor CREB (cAMP response element-binding protein) located in the promoter regions of target genes [25].

1.4 cAMP kit for assaying GPCR activation

The most common method for exploring GPCR signaling is through measuring the changes of the second messenger cyclic adenosine monophosphate (cAMP). Agonist binding of receptors that are coupled to $G_{\alpha s}$ protein elevate cAMP levels, whereas activation of GPCRs coupled to $G_{\alpha i}$ protein leads to decrease in cAMP. MC4R neurons localized in the hypothalamus signal by $G_{\alpha s}$ -dependent increase of intracellular cAMP to increase energy expenditure [26].

A number of different kits are available on the market for measuring cAMP levels in the cell. A very common readout method is provided by reporter genes that contain a cAMP response element (CRE) that regulates the expression of an enzyme or a bioluminescent protein [27, 28]. An alternative approach is based on the use of antibodies that specifically recognize intracellular cAMP as well as exogenous labeled cAMP conjugate acting as competitor. Detection is based on a Förster resonance energy transfer (FRET) reaction. As this work utilizes the latter kit, the principle is consequently explained in more detail.

The cAMP dynamic 2 kit from Cisbio can be used for studying both $G_{\alpha s}$ and $G_{\alpha i}$ coupled GPCRs. It is based on cAMP accumulation which is achieved by inhibition of degradation to 5'-AMP by 3-isobutyl-1-methylxanthine (IBMX) (Fig. 1.2a). The assay makes use of Homogenous Time-Resolved Fluorescence (HTRF) technology that constitutes a FRET measurement in a time-resolved homogenous format [30]. Here, a time delay (50- 150 μs) between excitation of donor and readout of acceptor-emission is introduced to avoid autofluorescence from cells, buffer or ligands. For this reason the assays makes use of long-emitting donor molecules, such as europium which has a half-live of 300 μs to 1 ms [30, 31].

The cryptate is conjugated with the cAMP-antibody and exhibits emission at 620 nm, whereas exogenous cAMP is coupled with the acceptor d2. The measurement of endogenous cAMP occurs by competing with d2-labeled cAMP for the anti-cAMP antibody binding sites. The binding of the antibody to the d2-labeled cAMP brings the donor and acceptor into the proximity range (Fig. 1.2b). Upon excitation of europium at 340 nm, the energy can be transferred to d2. The energy of donor and acceptor are in resonance so that the spectral overlap causes the excitation of the acceptor with the resulting emission at 665 nm (FRET signal). The signal is inversely proportional to the concentration of endogenous cAMP that crowds out d2-cAMP to bind anti-cAMP antibodies [29]. An increased level of intracellular cAMP leads to disruption of the FRET signal, whereas inhibition of cAMP production by the cells results in a higher FRET signal. The

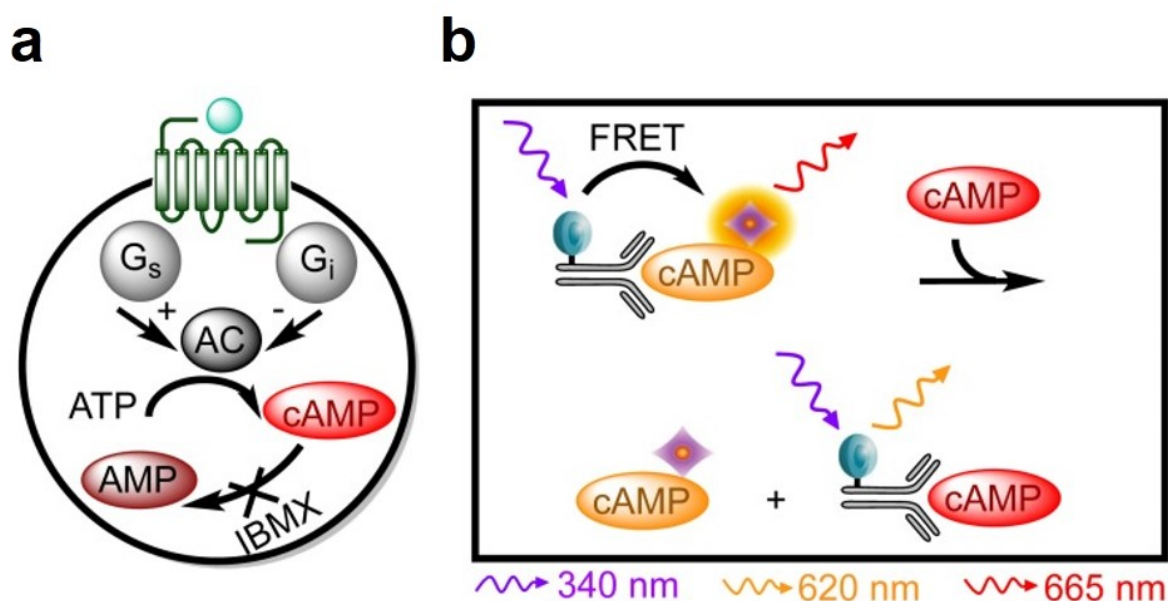


Figure 1.2: Principle of FRET-based cAMP detection. a) Activation of G-proteins occurs upon stimulation of GPCR and either activates ($G_{\alpha s}$) or inhibits ($G_{\alpha i}$) adenylyl cyclase (AC) which converts ATP into cAMP. b) Intracellular cAMP competes with exogenous acceptor-labeled cAMP for binding to donor-labeled cAMP antibody. Figure adapted from [29].

analysis of the HTRF assay output occurs in a ratiometric manner, where the signal detected at 620 nm is divided by the signal at 665 nm. The FRET ratio corrects for system errors and well-to-well variations caused by the optical properties of the compounds and medium [29].

HTRF based assays allow the direct measurement of cell lysate in the presence of cell culture medium [32] and can be easily adapted to high throughput screenings.

1.5 Membrane protein solubilization and stabilization

When alone in aqueous buffers, membrane proteins are not well folded and may lack full activity. For this reason, additional components which provide hydrophobic environment are needed. Finding a suitable environment with optimal properties for different downstream studies is one of the largest challenges in membrane protein solubilization. The ideal environment should accomplish the protein stability and should provide the option of purification to enable the study of its structural and functional properties.

There are different membrane-mimetic systems commonly used in membrane protein research (Fig. 1.3). These systems have been reviewed extensively [33–35].

The simplest and most popular method for membrane protein isolation is the solubilization of the biomembrane with detergents. Detergents consist of a hydrophobic tail and a hydrophilic head and thus act as a surfactant. Solubilization of lipid bilayer matrix with detergents leads to the formation of micelles which are arrangements of detergent molecules with their polar heads outside and their hydrophobic tails inside. Micelles are rather small in diameter (4-6 nm) and

shield the exposed hydrophobic parts of the membrane protein with detergent tails inside the micelle (Fig. 1.3a). Micelles are no static formations since detergent molecules are always exchanging with monomeric detergent molecules in the solution. As a result, membrane proteins show a lower stability and may be denatured in micelles [36,37].

Another possibility that provides a non-bilayer environment for stabilization of membrane proteins is the use of amphiphilic polymers (amphipols). These polymers adsorb onto the hydrophobic surface of membrane proteins and conserve their structure (Fig. 1.3b). Amphipols provide a more advanced platform since they improve the stability of membrane proteins (reviewed in [38]), especially this has been shown for 7-transmembrane proteins [39].

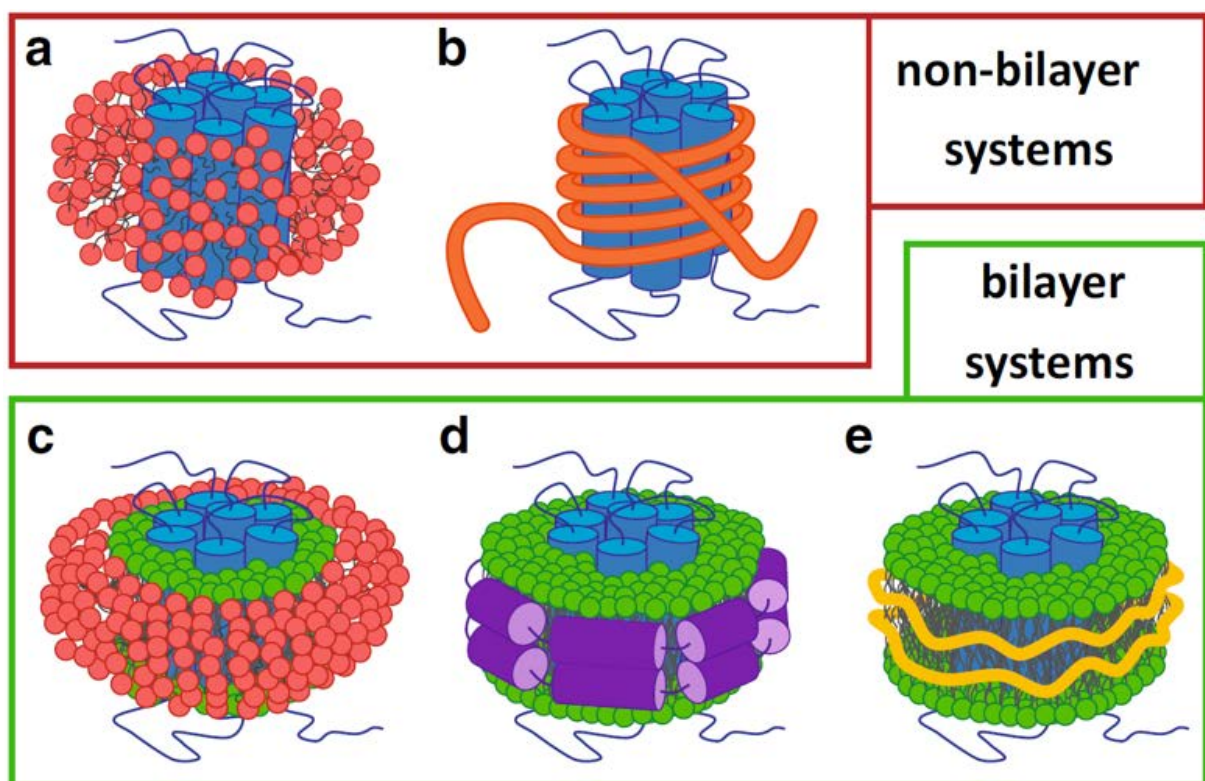


Figure 1.3: Membrane-mimetic systems for membrane protein stabilization. Models proposed for membrane protein stabilization in aqueous media. Protein can be stabilized in non-bilayer systems like detergent micelles (a) and amphipols (b) or by using bilayer systems such as bicelles (c), nanodiscs (d) or styrene-maleic acid (SMA) lipid particles. Figure from [34].

A huge drawback of using detergents and amphipols is the lack of lipid bilayer environment which can be an issue because of the importance of such an environment for structure, function, and stability of membrane proteins [37].

One strategy to overcome this issue is to reconstitute membrane proteins into systems of phospholipids, i.e. as vesicles or bicelles. Vesicles allow studying the effect of lipid composition on structural and functional properties of the proteins, however a great disadvantage is the

relatively large size which complicates optical spectroscopy due to light scattering [34]. Bicelles are discoidal formations obtained by mixing short-chain phospholipids with detergents in a defined ratio (Fig. 1.3c) [40]. Bicelles have sizes ranging from 8-50 nm in diameter [41] and are suitable for NMR spectroscopy [42]. However bicelles are limited in the choice of lipids and often lack stability.

A relatively new platform for stabilization of membrane proteins is the nanodisc technology which was developed by Sligar *et al.* [43,44]. Nanodiscs consist of an assembly of phospholipids wrapped around by an amphipathic apolipoprotein, called membrane scaffold protein (MSP) that shields the hydrophobic core of the lipids from the aqueous phase (Fig. 1.3d). Nanodiscs typically have a diameter of 10 nm, but specific MSP proteins have been engineered with the aim to form smaller nanodiscs [45]. The optimal control of size makes nanodisc an excellent platform for many biophysical studies characterizing membrane proteins.

The SMA copolymer

Even though there has been made a lot of progress in developing different membrane-mimetic systems for stabilization of membrane proteins, all these system as described above have the disadvantage that they require the use of a detergent for extraction of the protein from membranes. In order to reduce the problem of destabilization by detergents, alternative approaches have been developed from which the solubilizing effects of amphipathic styrene-maleic acid (SMA) is the most promising [46]. In contrast to detergents, addition of SMA to lipid membranes leads to the formation of discoidal particles with a diameter of approximately 10 nm retaining the bilayer organization (Fig. 1.3e) [47]. The most striking feature of SMA is its capability to extract and stabilize membrane proteins from membranes without the need of a solubilization with detergents [48].

SMA is synthesized by a radical chain reaction of styrene and maleic anhydride monomers which leads to the formation of styrene-maleic anhydride copolymers (SMAnh). By hydrolysis of SMAnh, the copolymer is transformed into its solubilization active form [49,50]. When changing the monomer ratio, the overall styrene-to-maleic anhydride ratio can be modified. In this thesis, we will focus on copolymers obtained by Polyscope, such as Xiran 25010, Xiran 30010, and Xiran 40005 with a styrene-maleic acid ratio of 3:1, 2.3:1, and 1.2:1 respectively. SMA with 2.3:1 and 3:1 ratio are the most commonly used polymers. For solubilization of lipid bilayers, the polymers are used at pH between 7 and 8, at which SMA adopts a random coil conformation with the best compromise between electrostatic interactions and hydrophobic effect [34].

1.6 Recombinant protein expression in insect cells

The use of eukaryotic cells has emerged as a popular system for recombinant protein expression. Especially when posttranslational modifications and correct disulfide-bond formation are important for protein folding and activity, eukaryotic expression systems are the preferred

choice. Among these systems, the baculovirus-infected insect cell platform has become a powerful tool to express for structural and functional studies.

The baculovirus expression vector system (BEVS) came up in the 1980s as a novel tool for heterologous protein expression [51]. The system uses insect cell lines, which are infected by baculoviruses (BV) to express the protein of interest. The most widely used BV is the lytic *Autographa californica* nuclear polyhedrosis virus (AcNPV) [51, 52]. AcNPV is able to infect a wide range of cell lines making it suitable for cell suspension culture expression.

At present, three main types of insect cells are used for recombinant protein expression - Sf9, Sf21 and Tn5. Sf21 cells were isolated from ovarian tissue of the American fall army worm's (*Spodoptera frugiperda*) pupal tissue, whereas Sf9 cell line is a substrain of Sf21 [53]. Tn5 (also called High-Five™) cells originate from the ovarian cells of the cabbage looper (*Trichoplusia ni*, *Tn*) [54]. The strains have different characteristics in terms of growth rate, virus production and protein expression. Sf9 cell line is the strain with the highest virus production, whereas Tn based cells have been described to be more efficient in overall protein yield and especially in terms of secretion [55–57]. A new *Trichoplusia ni* cell line BTI-Tnao38 has been established [58] and preliminary studies showed a tenfold susceptibility to baculovirus infection as well as a considerably higher protein expression yield compared to Sf9 cells [59].

Once in the cell, the BV infection cycle consists of three phases - the early, late and very late phase. The early phase is characterized by the attachment to the host cell and the release of the viral DNA into the host cell which results in a suppression of the cellular gene expression [60]. Virus entry is taking place via clathrin-mediated endocytosis in less than one hour. 10 to 20 hours post infection (hpi) viral DNA is replicated in the nucleus of the infected cell (late phase). During the very late phase (24-72 hpi) of the infection cycle, enveloped virions, which are embedded in a matrix comprised of polyhedrin are formed. The protein polyhedrin is expressed under the control of the very strong *polh* promoter and accounts for 50% of the total protein content on an infected cell. Polyhedrin is non-essential for virus replication, and its gene can be replaced by other genes to create a recombinant virus for foreign gene expression.

A milestone in the development of the BEVS was the observation that transfection of viral DNA alone could cause baculovirus infection [61]. This so called baculovirus shuttle vector system [62] (commercially available as Bac-to-Bac™, Invitrogen) is based on a modified *E. coli* strain (DH10Bac™), which produces by *in vivo* transposition recombinant bacmid from a donor plasmid containing the gene of interest (Fig. 1.4). The bacmid is used for transfection of insect cell lines to generate recombinant baculovirus which can be used for recombinant gene expression after multiple amplification steps to obtain high titer virus stocks.

Protocols for GPCR expression in several host systems have been established, but up to now, the baculovirus expression system has turned out to be the most suited and reliable host system for high amount GPCR expression, a large number of membrane protein structures have been solved from targets expressed in insect cells [63].

1 General Introduction

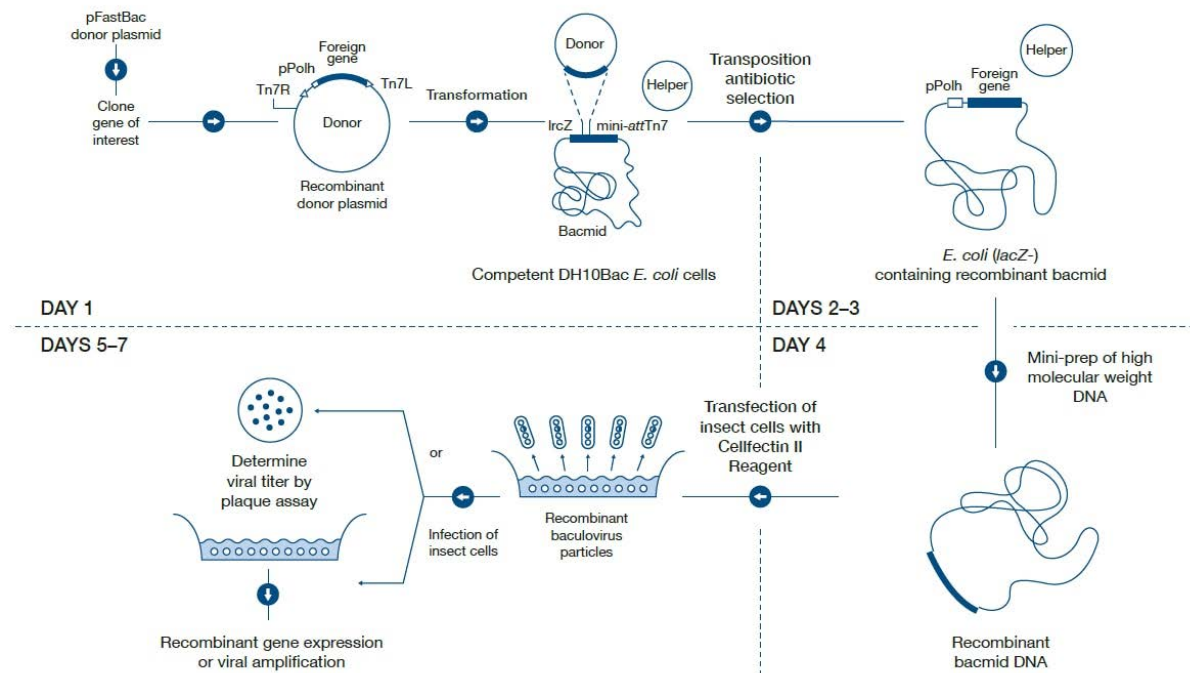


Figure 1.4: Overview of the Bac-toBac™ Baculovirus protocol. After cloning into donor plasmid, the gene of interest recombines with the parent bacmid in DH10Bac™ *E. coli* to form an expression plasmid. After selection via blue/white screening of positive recombinants, the bacmid is then transfected into insect cells for generation of recombinant baculovirus particles. Whole protocol can be accomplished in 5-7 days.

1.7 α -Synuclein and Parkinson's disease

Parkinson's Disease (PD) is the second most common neurodegenerative disease, the risk to develop PD is 2% for men and 1.3% for women [64]. The main characteristic symptoms of PD are muscle stiffness, slow movement, tremor and postural instability [65]. Pathophysiologically, PD displays a degeneration of dopaminergic cells in the *substantia nigra*, a region of the midbrain that is involved in motor control and reward [66]. A characteristic feature of PD is the intraneuronal formation of aggregated protein called Lewy bodies [67]. These formations mostly consist of aggregates of endogenous protein called α -Synuclein (α Syn).

The aggregation of α Syn is the central pathogenic characteristic of PD [68–73]. α Syn is a protein of 140 amino acids and 14.5 kDa that is expressed in the central nervous system (CNS). α Syn consists of an amphipathic N-terminus (residues 1-60), a hydrophobic, aggregation-prone middle region, the so-called non amyloid- β component (NAC region, residues 61-95) and a highly negatively charged C-terminus (residues 96-140). The NAC region has been shown to be involved in β -sheet and fibril formation, as reported recently upon structure determination by solid-state NMR [71].

The physiological role of α Syn is not fully clear to date, it is assumed that it is involved in synaptic vesicle homeostasis [74, 75] as well as in maintenance of soluble N-ethylmaleimide-sensitive-factor attachment receptor (SNARE)-dependent vesicle fusion [76]. In its cytosolic form, α Syn is an intrinsically disordered protein (IDP) which lacks a stable secondary struc-

ture and has a rather unfolded structure (random coil). However, it can form transient contacts between amino acids from the NAC region which leads to the formation of β -strands in α Syn fibrils [77].

The aggregation is indirectly toxic to cells, as the depletion of α Syn monomer leads to misfunction of vesicle trafficking which finally results in increased apoptosis [78].

α Syn is in an equilibrium between a cytosolic and a membrane-associated state which might be explained by its involvement in synaptic vesicle trafficking, where both membrane association and cytosolic solubility are needed. The presence of lipid membranes induces formation of a positively charged α -helix in the N-terminus and the NAC region of α Syn [79]. When binding to negatively charged lipids, α Syn forms an α -helical fold that spans residues 3 to 92 which contain repeats of lysine-rich sequences interspaced with hydrophobic residues [80]. Recent studies showed that the presence of lipids can modulate α Syn aggregation behaviour [81–83].

Interestingly, it has also been shown that α Syn, due to its amphiphatic character, can stabilize lipid bilayers analogous to the membrane scaffold protein (MSP) [84, 85] and that stable α Syn-lipid particles (α Syn-Lips) can be assembled *in vitro* using similar approach as for nanodisc preparations [86, 87].

Monitoring α Syn aggregation *in vitro* is commonly performed by usage of so called Thioflavin T (ThT) assays. ThT is a fluorescent dye that binds to β -sheet-rich structures of amyloid aggregates which enhances its fluorescence emission (~100-fold) [88]. ThT is a very popular tool in protein aggregation studies, due to its high sensitivity and the possibility to use it in high-throughput screens.

Other than that, atomic force microscopy (AFM) is a suitable method for analysis and characterization of amyloid aggregates. AFM is a very high-resolution type of scanning probe microscopy, where the information is gathered by scanning of a planar surface with a mechanical probe. AFM provides a resolution down to <0.1 nm which allows detailed imaging of amyloid fibrils.

1.8 Regulation of EGFR

The epidermal growth factor receptor (EGFR) is a major regulator of proliferation in epithelial cells acting as an interface between cells and their environment. Misregulated EGFR activation can lead to hyperproliferation and the development of cancer. So far, drug research focussed either on the extracellular sensory unit or on the intracellular kinase domain which transduces the signal to downstream effectors. The so-called juxtamembrane (JM) segment connects these two receptor domains and has been shown to be a site of modulation of EGFR activity by intracellular factors [89–92]. So far, little is known about possible interaction partners of JM. It has been shown that the cytosolic protein calmodulin (CaM) binds to the N-terminal part of the JM segment in a calcium-dependent manner [93, 94] enhancing EGFR activation [95, 96]. Identification and characterization of further binding partners allows to get better insights into EGFR activation.

1.9 Scope and objectives

A large number of cellular processes is regulated by a complex interplay between several hormones, membrane-embedded proteins and lipids. Membrane biochemistry has benefited in the past from improvements both in terms of sample preparation (protein expression and purification) and biophysical characterization. However, finding a suitable membrane mimetic system for membrane protein stabilization as well as for interaction studies with peptides remains still challenging.

This work explores approaches to overcome these limitations. Figure 6.17 summarizes the specific aims of this thesis.

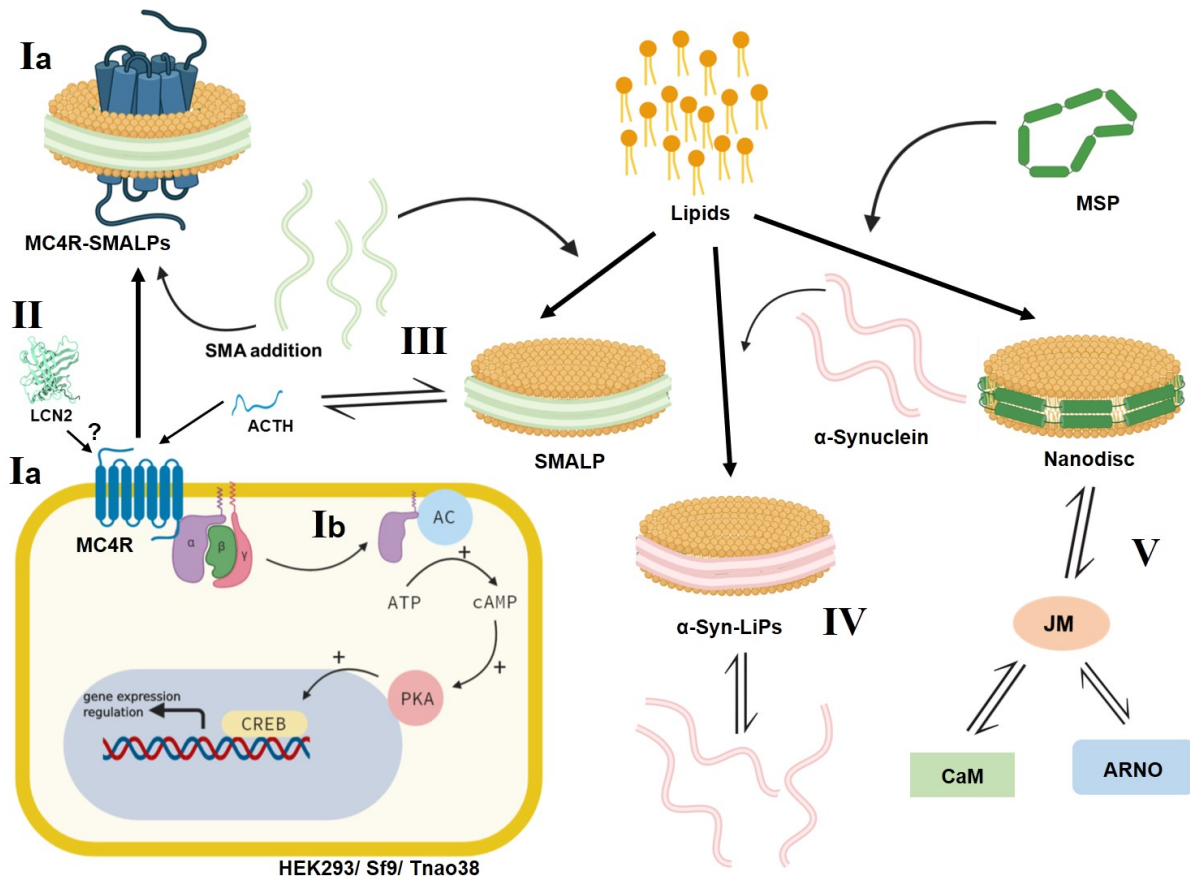


Figure 1.5: Summarizing scheme of this PhD thesis. The objectives can be classified into peptide-receptor interaction (I + II) and peptide-lipid interaction (III, IV, V). MC4R - Melanocortin-4 receptor, SMA - styrene-maleic acid, SMALPs - SMA lipid particles, AC - adenylyl cyclase, ATP - adenosintriphosphate, cAMP - cyclic adenosine monophosphate, PKA - protein kinase A, CREB - cAMP response element-binding protein, LCN2 - lipocalin 2, ACTH - adrenocorticotrophic hormone, αSyn-LiPs - αSynuclein-lipid particles, MSP - membrane scaffold protein, JM - juxtamembrane (segment of Epidermal Growth Factor), CaM - calmodulin, ARNO - ADP ribosylation factor nucleotide binding-site opener

The first objective is the expression and functional characterization of melanocortin-4 receptor (MC4R) in eukaryotic expression systems (Chapter 2). This study is divided into two main sections: the first one is focussed on expression and purification (Ia in Fig. 6.17) and the second one on functional characterization in cells (Ib). The latter is addressed by establishing a FRET-based cAMP accumulation assay that is applied to human and insect cell lines. MC4R expression is optimized in insect cells and extraction is explored using styrene-maleic acid (SMA) copolymer.

The second objective is testing the previously reported agonistic effects of lipocalin 2 (LCN2) on MC4R. This includes biophysical characterization of LCN2 as well as functional studies using cell-based cAMP assay (Chapter 3, II).

The third objective is establishing a method for determination of interaction of peptides with lipid membranes. This is addressed by combining SMA lipid particles with microfluidic diffusional sizing measurements (Chapter 4, III).

In a similar fashion, the fourth objective is to explore the effect of α Syn lipid particles (α SynLiPs) on α Syn amyloid fibril formation. We optimized and characterized α SynLiPs assembly with different lipids and use aggregation assays to investigate the influence of α SynLiPs in α Syn aggregation (Chapter 5, IV).

The fifth objective is the investigation of a network of possible epidermal growth factor receptor (EGFR) modulators. We explored interaction as well as binding modes of different modulators using microscale thermophoresis (MST) and nuclear magnetic resonance (NMR) in connection with nanodisc system (Chapter 6, V).

Overall, the objectives can be classified into peptide-receptor interaction (I + II) and peptide-lipid interaction (III, IV, V). Due to existing limitations for all objectives the development of new methods tailored to advance the respective field is a central element of the presented work.

2 Insights into Hormone - GPCR Interactions: Enhancing eukaryotic MC4R expression for structural studies

2.1 Abstract

Feeling hungry - or saturated is predominantly regulated in the brain by a complex interplay between several hormones and a membrane-embedded protein called melanocortin-4 receptor (MC4R). MC4R belongs to the pharmacologically extremely important class of G protein-coupled receptors (GPCRs) and so far there are no experimental high-resolution insights into the communication of the different ligands and accessory proteins that regulate receptor signaling.

Here we report successful improvements in MC4R expression by using baculovirus infected insect cells. Expression rates could be significantly increased in comparison to HEK293-based expression. The recently developed Tnao38 cell line showed evidence to give even more expression yields compared to commonly used Sf9 cell line. Furthermore we established a FRET-based cAMP accumulation assay for MC4R in both, HEK293 and insect cell lines, which allows reliable characterization of ligand interaction with the receptor.

We also demonstrate detergent-free reconstitution of MC4 receptor into styrene-maleic acid lipid particles (SMALPs) from Tnao38 cell membranes. This promising approach demonstrates that MC4R can be extracted and purified without removal from their native lipid environment for biophysical characterization.

2.2 Introduction

Expression of recombinant GPCRs

Study of integral membrane proteins is one of the major challenges in molecular biology. Membrane proteins play a key role in the biology of the cell, as e.g. 20-30% of all open reading frames in the human genome are predicted to encode for membrane proteins [97]. In the past years, much progress has been made in the structure determination of membrane proteins. However, structures of membrane proteins are largely underrepresented, according to the Protein Data Bank (PDB) out of 110,636 protein structures only 3,282 (2.9%) describe membrane proteins. Since it is estimated that membrane proteins, and especially GPCRs, represent more than 50% of drug targets [4] it is crucial to further investigate their structural biology.

The primary bottleneck for structural studies of membrane proteins is the requirement of high yields of pure and correctly-folded target protein. Progress has been made to produce sufficient quantity and quality in different host systems.

Mammalian cells provide the most native cellular environment, including correct trafficking and folding of GPCRs. Overexpressed proteins become usually post-translationally modified

correctly making mammalian cells ideal to characterize GPCR function and pharmacology [63]. The immortalized human embryo kidney 293 (HEK293) cell line can transiently express recombinant proteins and is the most popular cell line to use [98, 99]. HEK293 cells can be cultivated adherently or in suspension, the latter is used for protein production [98].

The baculovirus based insect cell expression system (mainly *Spodoptera frugiperda* (Sf) or *Trichnoplusia ni* (Tn) cells [100]) is a well-established expression system for expression of functional membrane proteins [63, 100]. Nearly all post-translational modifications are identical to mammalian cells and most GPCRs can be expressed actively [101]. Insect cells can be grown in serum-free shaker cultures which reduces costs and makes scale-up easier.

Protocols for GPCR expression in all host systems have been established, but up to now, the baculovirus expression system has turned out to be the most suited and reliable host system for high amount GPCR expression, and a large number of membrane protein structures have been solved from targets expressed in insect cells [63].

Purification of GPCRs

The second bottleneck for biophysical characterization of membrane proteins is the need to solubilization and purification of these proteins [36]. Both process should ideally maintain the protein's folding and activity for further downstream applications. Surfactant detergents are able to solubilize and extract membrane proteins due to their amphiphilic nature, improving the aqueous solubility of the protein [102, 103]. Detergents can be classified into three classes based on their polar head group - ionic, zwitterionic and non-ionic. Ionic reagents such as SDS are regarded as harsh, zwitterionic are milder (LDAO) while non-ionic detergents are considered mild [103]. The non-ionic alkyl maltopyranoside detergent DDM has been used most when solving membrane protein structures (approximately 45%) [104].

A huge drawback of using detergents is the lack of lipid bilayer environment, which can be an issue because of the importance of such an environment for structure, function, and stability of membrane proteins [37]. Replacing detergents with better membrane mimetics could prevent destabilisation of proteins.

Styrene-maleic acid (SMA) is an amphipathic copolymer that, when added to lipids, spontaneously assembles into nanoparticles of ~10 nm diameter in which the co-polymer surrounds a patch of lipid bilayer. Similarly, SMA can also be added to biological membranes which leads to the formation of styrene-maleic acid lipid particles (SMALPs) containing membrane proteins. The most striking feature of SMA is the possibility to directly extract membrane proteins from cells without a detergent solubilization step. This method has been used in various approaches demonstrating also usability of SMALPs for different biophysical and biochemical techniques to study membrane proteins [49, 105–108].

2.3 Material and Methods

HEK cell culture and MC4R expression

HEK293F cells (kindly provided by Dr. Sabine Schriek) were maintained in FreeStyle 293 expression medium (Gibco, Life Technologies) supplemented with 100 U ml^{-1} penicillin and $100 \mu\text{g ml}^{-1}$ streptomycin and cultured at 37°C in a 5% CO_2 atmosphere. For MC4R expression two different strategies were used: (I) stable transfection (II) transient transfection. In both cases, cells were transfected with pHL-IRES-MC4R vector, in which human wildtype MC4R is N-terminally flanked by signal peptide prolactin followed by a FLAG-tag and C-terminally by a hexahistidin-tag. Stably transfected HEK293F-MC4R cells were developed and kindly provided by Dr. Sabine Schriek and were cultivated as described above, but with addition of $400 \mu\text{g ml}^{-1}$ Geneticin (G-418 sulphate, gibco, Life Technologies) instead of penicillin/streptomycin.

For transient transfection, HEK293F cells were split one day before transfection at a density of 600 000 cells/ml. Next day cells were transfected using Lipofectamine 3000. $40 \mu\text{l}$ Lipofectamin reagent were mixed with 1 ml FreeStyle medium. Separately, $20 \mu\text{g}$ of MC4R expression vector were mixed with $40 \mu\text{l}$ P3000 Reagent in 1 ml FreeStyle medium. Subsequently, mixtures were combined, incubated for 20 min and then added straight to the cells, followed by incubation at 37°C for 48 h.

Insect cell culture and MC4R expression

MC4R gene with prolactin signal sequence, FLAG-tag and 6x His-tag was excised from pHLIRES vector using restriction enzymes *EcoRI* and *XhoI* (Thermo) und cloned into the *EcoRI-XhoI* site of pFastBac1 vector. The recombinant vector pFastBac1-MC4R was transformed into competent *E. coli* DH10Bac cells and plated out onto blue/white selective LB-plates containing $50 \mu\text{g/ml}$ kanamycin, $10 \mu\text{g/ml}$ tetracycline, $7 \mu\text{g/ml}$ gentamycin, $100 \mu\text{g/ml}$ X-gal, and $40 \mu\text{g/ml}$ IPTG, and incubated for 48 h at 37°C . Recombinant bacmid-MC4R DNA was isolated and integration of target gene into bacmid DNA was proved by PCR using M13 forward and reverse primer as described by the Bac-to-Bac Baculovirus Expression System kit user manual.

For generation of recombinant baculovirus, 9×10^5 Sf9 cells in mid-log phase were seeded per well of a 6-well plate in 2 ml Sf900III medium and allowed to attach. A mixture of $5 \mu\text{g}$ bacmid-MC4R DNA and $25 \mu\text{l}$ of CellFECTIN reagent was added to Sf9 cells in 1 ml Sf900III medium without antibiotics. After incubation for 5 h at 27°C , transfection mixtures were removed and replaced by 2 ml Sf900III medium containing antibiotics. p1 virus stock was harvested from cell culture medium 96 h post-transfection. For amplification of viral stock, a 50 ml Sf9 suspension culture was infected with 0.5 ml of p1 stock. p2 stock was harvested 48 h later and was used to generate high titer virus stock (500 ml).

For receptor expression, both Sf9 and Tnao38 cell lines were used. Cells were cultured at 27°C in Sf900III SFM medium supplemented with 50 U/ml Penicillin, $50 \mu\text{g/ml}$ streptomycin and $1 \mu\text{g/ml}$ amphotericin B. Cells at density of 1.5×10^6 per ml were infected with virus and

2 Insights into Hormone - GPCR Interactions: Enhancing eukaryotic MC4R expression for structural studies

incubated for optimal period of time. Cells were collected by centrifugation at 1000 *g* for 5 min and stored at -80 °C until further usage.

cAMP assay

cAMP accumulation was measured using the HTRF cAMP Dynamic kit (Cisbio, Codolet France) according to the manufacturer's protocol. In brief, cells were diluted in stimulation buffer (cell culture medium + 500 μ M 3-Isobutyl-1-methylxanthin (IBMX)) distributed to 384-well low volume microplate (Greiner) and treated with the indicated compounds for 30 min (if not indicated otherwise) at 37 °C. FRET-pair, consisting of cAMP-d2 and Anti-cAMP-Cryptate, was dissolved in lysis & detection buffer and added to the cell-ligand mixture. The plates were incubated for 60 min at room temperature, and fluorescence was measured at dual emission wavelengths (620 and 665 nm) on a Tecan Spark 10M plate reader. EC₅₀ values were calculated using non-linear regression in Origin.

MC4R purification

Frozen cell pellet was resuspended in lysis buffer containing 50 mM HEPES/NaOH, pH 7.4, 150 mM NaCl and EDTA-free protease inhibitor cocktail tablet, then lysed by nitrogen cavitation (500 psi, 15 min, 4 °C). Cell debris was removed by low-speed centrifugation (750 *g*, 20 min, 4 °C), then membranes were harvested by ultracentrifugation (100 000 *g*, 30 min, 4 °C). Membrane concentration was adjusted to 100 mg/ml (membrane weight). For SMA purification of MC4R, membranes were diluted to final concentration of 40 mg/ml with solubilization buffer containing 50 mM HEPES/NaOH, pH 8, 150 mM NaCl and SMA was then added to a final concentration of 2.5% (w/v). Samples were incubated at 25 °C for 2 h with gentle shaking. Insoluble material was removed by centrifugation (100.000 *g*, 5 min, 4 °C).

SMA-solubilized membranes were incubated overnight at 4 °C with Ni-NTA agarose (Macherey-Nagel) with gentle shaking. The sample was transferred to a gravity flow column, washed twice with 10 column volumes (CV) of solubilization buffer, then twice with 10 CV buffer supplemented with 40 mM imidazole. MC4R-SMALPs were eluted using buffer supplemented with 250 mM and 0.5 CV fractions were collected. Samples of various stages of the purification were analyzed by SDS-PAGE (12%) and visualized by coomassie G250 staining and immunostaining using Western Blot with anti-FLAG antibody.

2.4 Results and Discussion

Expression of MC4R in eukaryotic cells

Full length and wild type MC4R was expressed in human cell line HEK293 as well as in insect cells (Sf9 and Tnao38) with a signal sequence and a Flag-tag N-terminally and a 6x His-tag at the C-terminus.

The prolactin signal sequence, which mainly consists of a hydrophobic region, was added to ensure localization to the plasma membrane [18, 109, 110]. During the process of insertion into the membrane, the signal sequence gets proteolytically cleaved. Both, FLAG- and 6x His-tag were added for immunodetection and purification purposes, respectively.

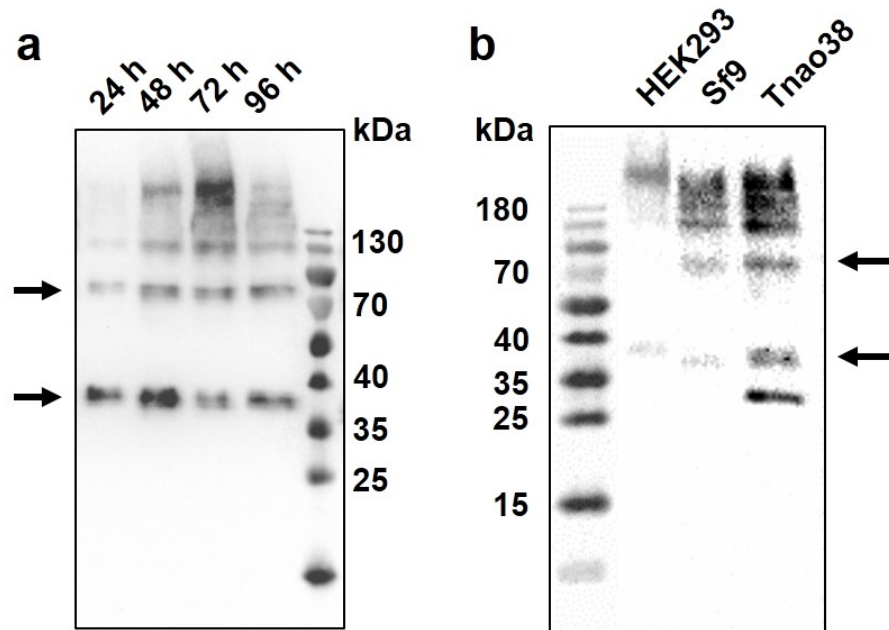


Figure 2.1: MC4R expression in different cell types. a) MC4R expression in HEK293F cells was monitored after transfection at timepoints as indicated. b) Comparison of MC4R expression in different cell types. Cell pellets (1×10^6 cells) were lysed with RIPA buffer and subsequently analyzed by SDS-PAGE and immunoblotting using a monoclonal anti-FLAG tag antibody.

As HEK293 cell line is commonly used for heterologous expression of GPCRs [98], we first examined this cell line for expression of MC4R. Cells were transfected with expression construct and incubated for 96 h taking samples in 24 h intervals. MC4 receptor expression was analysed by Western Blot using a monoclonal antibody against the FLAG-tag. As shown in Figure 2.1a, specific bands were observed, two most prominent were visible at ~37 kDa showing monomeric MC4R, and at ~80 kDa indicating a MC4R-dimer. MC4R expression reaches maximum at 48 h after transfection.

Next, we compared MC4R expression rates of HEK293 cells with those of insect cells. Figure 2.1b shows the result obtained from Western Blot. Both, Sf9 and Tnao38 cell lines were capable of producing higher rates of MC4R. Especially the newly developed Tnao38 cell line suits particularly well for expression of MC4 receptor (Fig. 2.1b).

For determination of optimal MC4R expression conditions in Tnao38 cells, we infected Tnao38 cells in small scale experiments with different dilutions (50x - 5000x) of p3 viral stock. Tnao38 cells were sampled at various timepoints post-infection and analyzed for MC4R protein

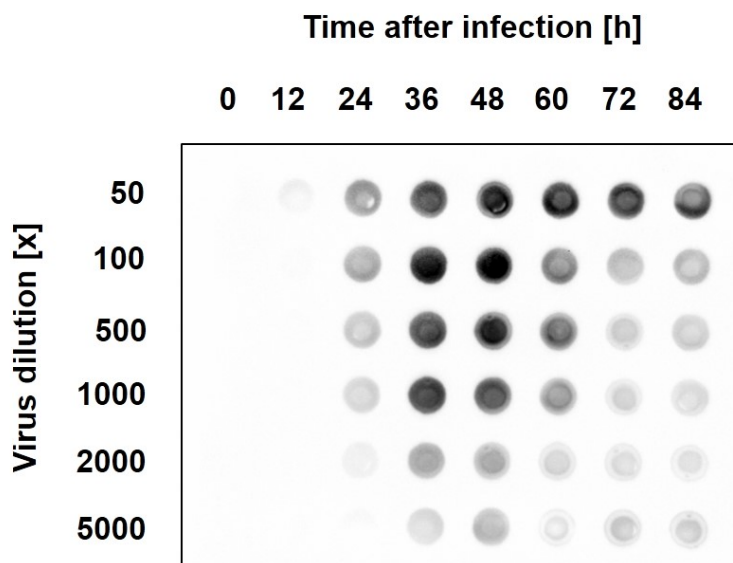


Figure 2.2: MC4R expression optimization in *Tnao38* cells. Insect cells are infected with different dilutions of virus (50x - 5000x) and harvested at different time points (0 - 84 h). Samples were analyzed by Dot Blot using an anti-FLAG tag antibody.

expression by dot-blot analysis (Fig. 2.2). Increasing amounts of baculovirus resulted in a slight, dose-dependent increase in MC4R expression with a peak around 36 and 48 h post-infection, especially when diluting virus 50-100-fold. MC4R expression is regulated by the polyhedrin promoter which gets activated in the very late phase of baculoviral infection [111]. Consistent with that, MC4 receptor protein expression starts 24 h after infection with virus.

Cell-based Assay for MC4R activity

Optimization process of cAMP assay in HEK293F cells

cAMP is a second messenger and one of the most important intracellular mediators. Changes in intracellular cAMP levels correlate with GPCR activation in particular for $G_{\alpha S}$ -coupled GPCRs. Measurements of cAMP levels can be used as an assay for GPCR activity. In this study we used the Cisbio Dynamic HTRF kit which is based on a competitive immunoassay between intracellular cAMP produced by the cells and cAMP labeled with the acceptor dye d2. Both cAMP molecules compete for binding to a cAMP-specific antibody labeled with a dye (europium cryptate) that acts as donor. The specific signal generated by Förster resonance energy transfer (FRET) is inversely proportional to the cAMP concentration in the sample. This kit allows the measurement of agonist and antagonist effects on $G_{\alpha S}$ - and $G_{\alpha i}$ -coupled receptors in different cell lines.

To optimize assay parameters, a cAMP standard curve was prepared with known cAMP concentrations to establish the relationship between the actual cellular response and the assay readout (Fig. 2.3a). The results are usually processed as ratio (Delta F) of acceptor wavelength (665 nm) and donor wavelength (620 nm). The measured signal has an inversal sigmoidal rela-

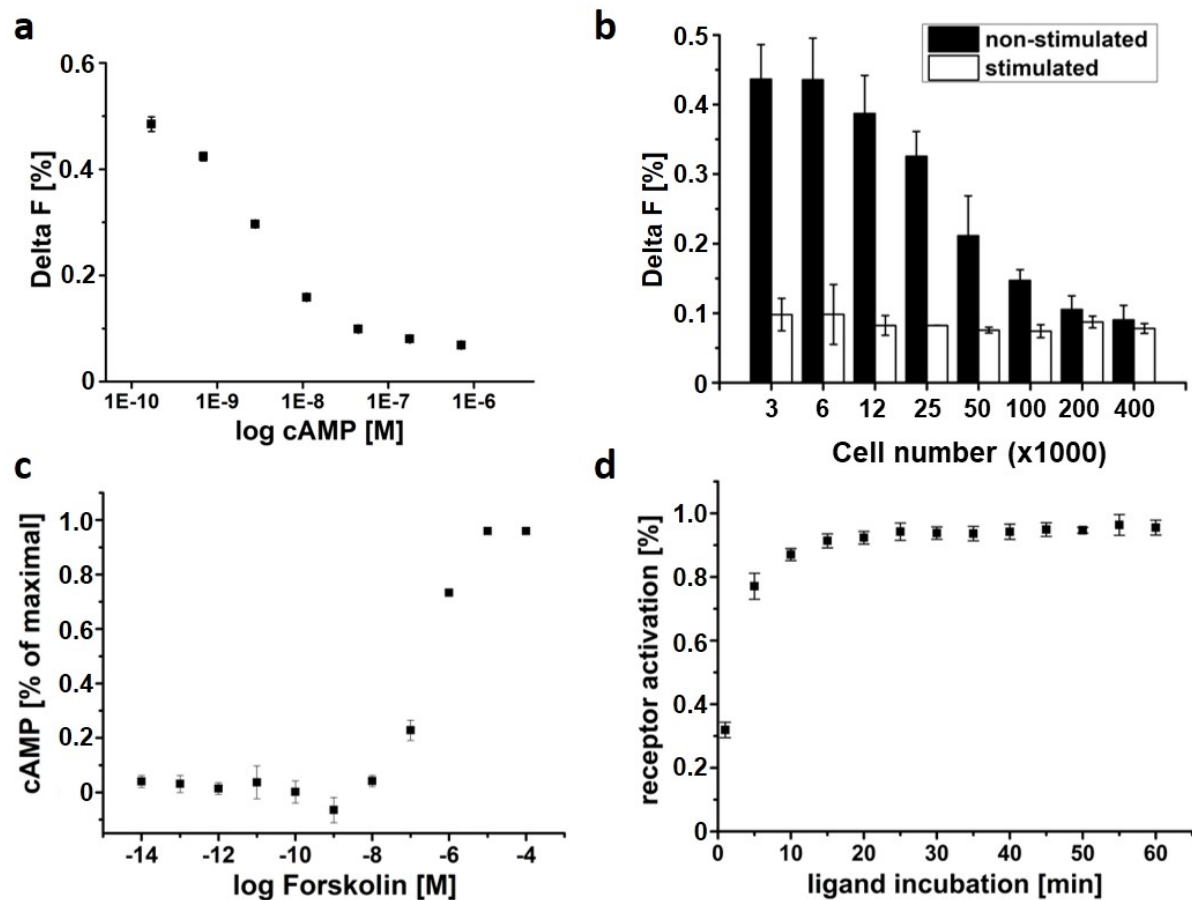


Figure 2.3: Optimization of assay parameters for performance of cAMP HTRF assay in HEK293 cells. a) Calibration curve for cAMP without cells. cAMP was used at concentrations from 0.17 to 712 nM. $n=3$ b) Optimization of cell number. Increasing numbers of HEK293F cells overexpressing hMC4 receptors were either incubated with 100 nM NDP- α -MSH (stimulated) or with stimulation buffer (non-stimulated). $n=2$ c) Cell response to Forskolin titration. A total of 5000 HEK293F cells expressing hMC4R were incubated with increasing concentrations of Forskolin. $n=3$ d) Optimization of incubation time. MC4R expressing HEK293F cells were incubated with 100 nM NDP- α -MSH. cAMP accumulation was measured in 5 min intervals. $n=3$

relationship with the log concentration of cAMP. The linear dynamic range of the assay is between a Delta F of 0.1 and 0.5. It is important that assay conditions are optimized so that the signal is in the linear range. Most importantly, the amount of cells that is used per well has to be optimized. The largest difference between non-stimulation and stimulation with NDP- α -MSH of MC4R expressing HEK293F cells is seen for 3000 and 6000 cells (Figure 2.3b). When cell number is too large, the sensitivity is too low to discriminate between cAMP upon activation and basal cAMP expression. For further experiments, 5000 cells were used, if not indicated otherwise. Forskolin is a cell-permeable activator of adenylyl cyclase (AC) and raises cAMP levels in the cell [112]. It is used as a positive control for G_s -based assays as it allows determination of maximal intracellular cAMP accumulation. We performed a titration of forskolin experiment with HEK293F-hMC4R cells. Upon treatment with forskolin, a dose-dependent cAMP accumulation could be observed with a maximal induction at 10 μ M (Fig. 2.3c). Finally, we optimized the duration of ligand incubation. Upon stimulation with NDP- α -MSH, maximal cAMP accumulation

2 Insights into Hormone - GPCR Interactions: Enhancing eukaryotic MC4R expression for structural studies

builds up after 20 min (Fig. 2.3d). The phosphodiesterase inhibitor IBMX was used during the assay to prevent degradation of cAMP. To ensure complete cAMP generation, an incubation period of 30 min was chosen for cAMP assays.

Characterization of MC4R activation

The evaluation of MC4R signaling pathways is of importance as it is one of the most important targets for antiobesity therapeutics. A variety of endogenous ligands interact with the melanocortin receptors. Agonists derive from the proopiomelanocortin (POMC) gene [113] and stimulate the receptors leading to increased cellular cAMP levels. A highly conserved His-Phe-Arg-Trp core sequence of the agonists is important for recognition and activation of the receptor (Fig. 2.4) [114].



Figure 2.4: Amino acid sequence of classical melanocortin ligands. Molecular recognition of POMC-derived naturally occurring agonists is based upon the conserved His-Phe-Arg-Trp (HFRW) motif.

Unique to the melanocortin system is the fact that the receptors have both naturally occurring agonists and inverse agonists. AgRP and ASP are the only known endogenous GPCR antagonists discovered to date [115–117].

α MSH is derived from the N-terminal 13 residues of ACTH (Fig. 2.4) and is N-terminally acetylated for increased stability [118]. Using the optimized cAMP assay we could demonstrate that MC4R gets activated by α -MSH with similar sensitivity as by ACTH. The corresponding EC₅₀ values are 6.52 nM (α -MSH) and 5.02 nM (ACTH) respectively which is consistent with values from literature [119]. This result confirmed the functionality and feasibility of the cAMP accumulation assay in context of MC4R activation.

Our results also show that potency of γ -MSH is at least tenfold reduced (EC₅₀ = 75.4 nM) when compared to α -MSH and ACTH. NDP- α -MSH is an α -MSH analog and was shown to have enhanced potency, increased resistance to proteolysis, and increased duration of action in comparison to α -MSH [120]. The methionine to norleucine substitution in position 4 and a replacement of D- for L-phenylalanine in position 7 lead to improved properties (Fig. 2.4). We can show that the synthetic ligand NDP- α -MSH leads to activation of MC4R with a half maximal effective concentration of 0.17 nM confirming significantly improved potency compared to α -MSH.

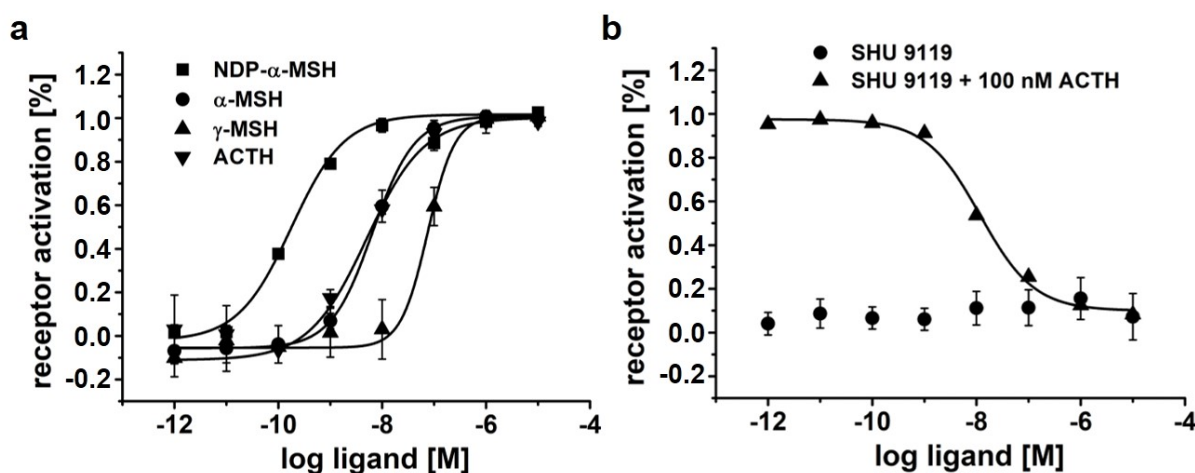


Figure 2.5: Ligand selectivity of MC4R. Functional activation of MC4R expressed in HEK293F cells after stimulation with different ligands. FRET-based cAMP accumulation assay was used in agonist mode (a) and antagonist mode (b). A total of 5000 cells expressing were incubated with increasing concentrations of ligands as indicated. n=3.

The assay can also be used for determination of antagonist activity of a G_s -coupled receptor. The procedure is essentially the same as for agonist detection. In the antagonist format, an agonist is added at concentrations that trigger activation and is displaced by the antagonist resulting in inhibition of cAMP accumulation.

We validated this by using SHU 9119 which is a synthetic derivative of α -MSH [121]. In the cyclic analog phenylalanine is substituted with a DNaI(2') residue (Fig. 2.4) which changed the pharmacological properties of the resulting ligand. While SHU 9119 shows agonist activity at MC1R and MC5R, it acts as antagonist for the MC3 and MC4 receptors [121, 122]. When incubated with MC4R expressing HEK293 cells, no changes in cAMP levels can be detected (Fig. 2.5b). Antagonist properties can be shown when simultaneously incubating with 100 nM ACTH resulting in a decrease of cAMP levels. ACTH is almost completely displaced by SHU 9119 in high nanomolar concentrations.

Taken together, we could successfully optimize and establish a FRET-based cAMP accumulation assay which enables characterization of agonist as well as antagonist activity of ligands. We could observe different potencies for MC4R agonists as well as inhibition of cAMP levels by SHU 9119.

MC4R activation in insect cells

Insect cell lines are not commonly used for functional GPCR assays even though they have been widely used as cell system for expression of several challenging eukaryotic proteins [123]. They provide proper protein folding as well as post-translational modifications such as glycosylation. However baculoviral infection of insect cells causes some difficulties for performance of cell based activity assays. On the one hand, the target protein is expressed very late in the viral life cycle when cell metabolism is mainly occupied by infection. On the other hand, the bac-

2 Insights into Hormone - GPCR Interactions: Enhancing eukaryotic MC4R expression for structural studies

uloviral expression is lytic for the insect cell and there is only a certain time window between target protein expression and cell lysis.

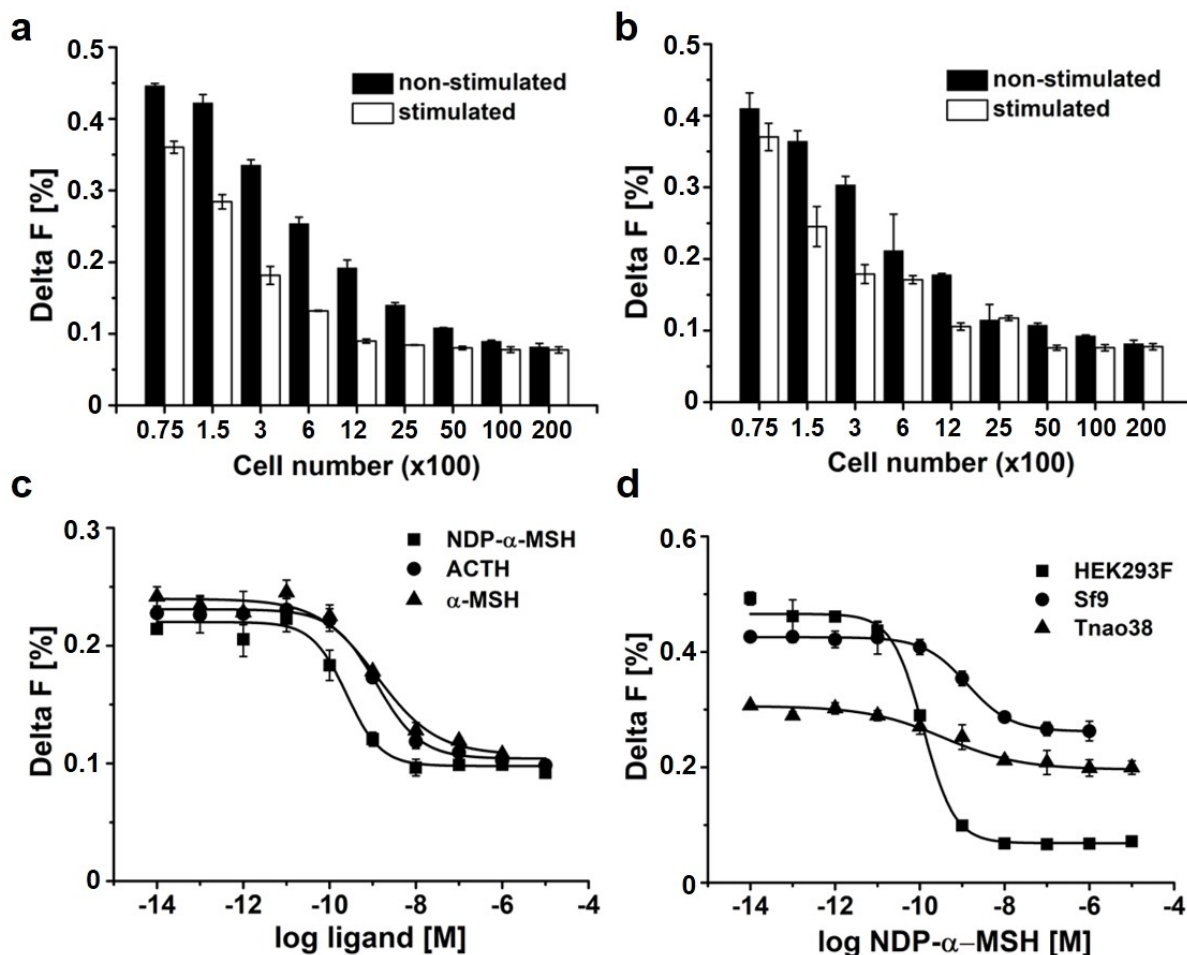


Figure 2.6: Functional characterization of MC4R in insect cells. a,b) Optimization of Sf9 (a) and Tnao38 (b) cell number for activation assay. Increasing numbers of cells overexpressing hMC4 receptors were either incubated with 100 nM NDP- α -MSH (stimulated) or with stimulation buffer (non-stimulated). n=3 c) Dose-dependent MC4R activation of different ligands in Tnao38 cells. A total of 500 cells were used per well. d) Comparison of dose-dependent MC4R activation by NDP- α -MSH in different cell lines. A total of 500 Sf9 and Tnao38 cells and 5000 HEK293F cells were used per well.

To study agonist-induced receptor activation in insect cells, Sf9 and Tnao38 cell line were infected with baculovirus encoding MC4 receptor. Functional studies with insect cell were carried out 48 h post-infection when cell viability was above 90%. Stimulation with synthetic agonist NDP- α -MSH lead to concentration-dependent cAMP formation in infected Sf9 and Tnao38 cells (Fig. 2.6a+b) with similar potencies compared to MC4R expressed in HEK293 cells (Fig. 2.6c). The corresponding EC₅₀ values are 0.24 nM (NDP- α -MSH), 1.23 nM (ACTH), and 1.26 nM (α -MSH) respectively.

Notably, when performing cAMP assay, optimal cell number using insect cells is lower as for HEK293 cells (Fig. 2.3b). This could be due to the higher amount of receptor produced in insect cells when compared to HEK293 cells (Fig. 2.1). Interestingly, the signal measured from the cAMP assay does not extend over the entire linear range (ΔF : 0.1 - 0.5) as observed for the cAMP standard curve (Fig. 2.3a) or for HEK293 cells (Fig. 2.6d). This is especially the case for cell numbers between 100 and 1000 where the cells are incapable of producing full amount of cAMP. Basal cAMP formation in Sf9 and Tnao38 cells is largely increased compared to HEK293 cells which might be due to increased cytosolic stress levels as a result of virus infection. Nevertheless, baculovirus infected insect cells are suitable for receptor activation studies, since the EC_{50} values are comparable to those obtained from HEK293 cells.

Taken together it can be ruled out, that the insect cell lines Sf9 and Tnao38 not only show higher expression rates than human cell lines, but also are capable of expressing functional MC4R. Moreover, the baculovirus expression system has proven to be a useful platform for performance of cAMP activity assays.

MC4R purification

Solubilization and purification of GPCRs from their native bilayer is an important step for *in vitro* studies [36]. The use of detergents is the most commonly used approach to mimic the hydrophobic environment for membrane proteins. Different detergents have been used so far for solubilization of GPCRs [124]. We performed a detergent screening for a range of detergents which can be divided into three groups: ionic, non-ionic, and zwitterionic [125]. 12 reagents that are generally used for solubilization and purification of membrane proteins were tested on solubilizing MC4R from Tnao38 cell membranes (Fig. 2.7a). Detergents have to be used in a concentration above their critical micelle concentration (CMC) to form micelles. 1% was chosen as standard concentration for all approaches, and for solubilization efficiency readout Dot-blot analysis was used.

The most effective detergent for solubilizing MC4 receptor was the denaturing ionic detergent sodium dodecyl sulfate (SDS) which provides a reference point as the maximum quantity of MC4R extracted from the cell membrane. Non-ionic reagents like DDM and Triton X-100 could be identified as very effective to solubilize MC4R. DDM has been most successful in solving membrane protein structures, approximately 45% of published structures used DDM [104].

The zwitter-ionic detergent family Fos-Choline has also been used for solubilization of GPCRs, Fos-Choline-16 was selected as suitable for human NK1 receptor extraction [126], and Fos-Choline-12 revealed excellent capabilities for solubilizing membrane proteins at similar levels with DDM [127]. However both members of Fos-Choline series showed rather bad efficiency when extracting MC4R from Tnao38 membrane, the efficiency level is more than three-fold decreased compared to that of DDM (Fig. 2.7a). Despite the benefit of reasonable solubilization properties, detergents have their limitations. The presence of lipid bilayer environment, has been shown to be essential for structure, function, and stability of many membrane proteins [37].

2 Insights into Hormone - GPCR Interactions: Enhancing eukaryotic MC4R expression for structural studies

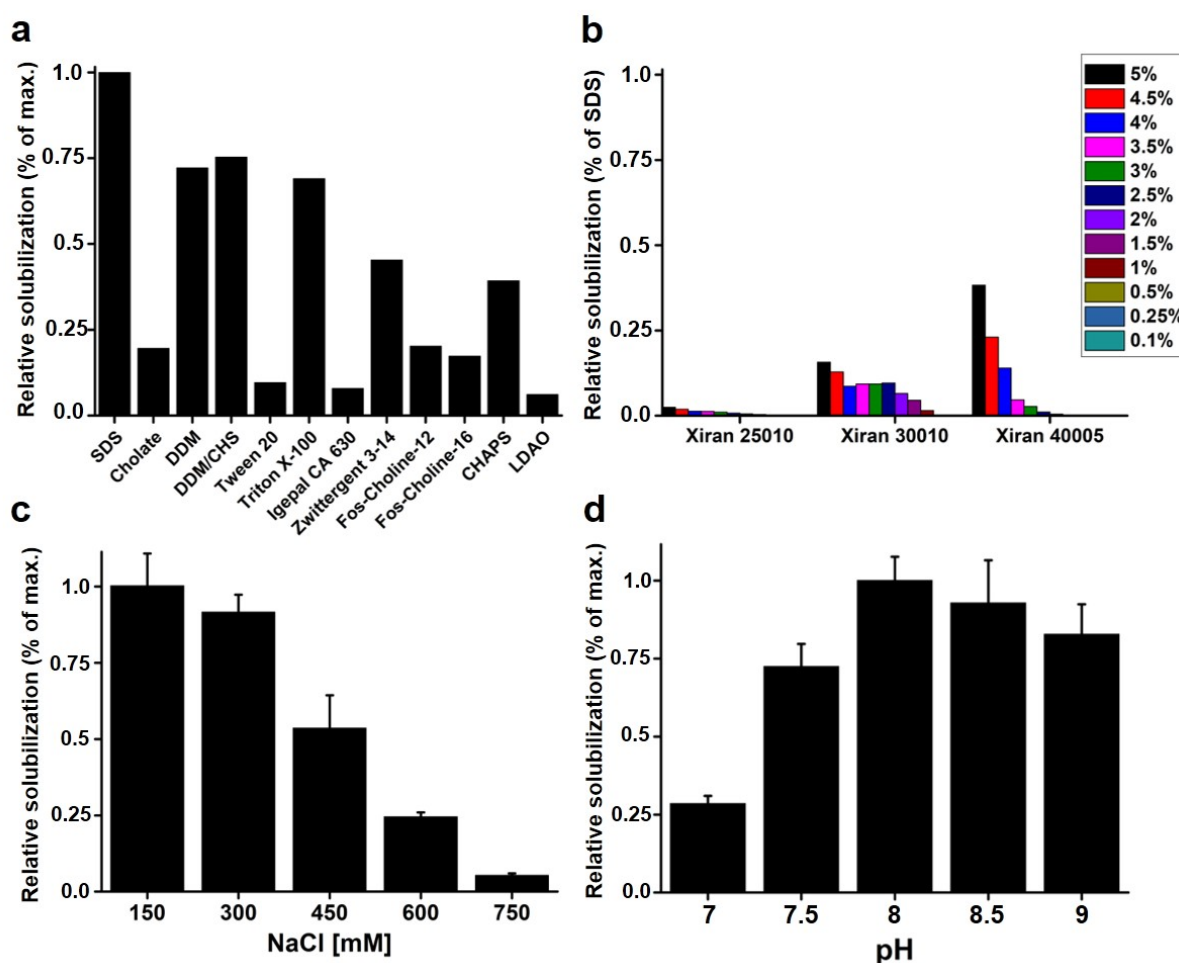


Figure 2.7: Solubilization of Tnao38 membranes containing MC4R. a, b) Effectiveness of different detergents (a) and styrene-maleic acid polymers (b) on solubilizing MC4R from Tnao38 cell membranes. Cell membranes with final concentration of 40 mg/ml were incubated either with final concentration 1% detergent (a) or with final polymer concentration as indicated (b). Samples were incubated for 1 h at 25 °C and analyzed using dot blot with anti-FLAG tag antibody. Dot blot raw data can be seen on Fig. 6.6 c, d) Influence of salt concentration (c) and pH (d) on solubilization efficiency of MC4R by Xiran 30010. All samples contained 2.5% SMA. Salt dependence was checked at pH 8. pH dependence contained buffer with 150 mM NaCl. Samples were incubated for 1 h at 25 °C centrifuged at 16 000 *g* for 30 min and supernatant was analyzed using dot blot with anti-FLAG tag antibody.

We thus studied the extraction of MC4R with styrene-maleic acid (SMA) which has the striking feature to directly extract membrane proteins from cells without an intermediate step of conventional detergent solubilization [48]. We tested different concentrations of the three most widely used Xiran Polymers (Polyscience), Xiran 25010, Xiran 30010, and Xiran 40005. They differ in average ratio of styrene to maleic acid repeat units which are 3:1 (Xiran 25010), 2.3:1 (Xiran 30010), and 1.2:1 (Xiran 40005) respectively. It can be seen that regarding solubilization efficiency, SMA polymers are less efficient when compared to detergents (Fig. 2.7b). When comparing among each other, the solubilization efficiency increases when ratio of styrene to maleic acid decreases. Xiran 40005 showed the best efficiency when using in higher concentrations (5%) but than dropped rapidly when decreasing polymer concentration below 3%. Xiran

30010 showed overall less efficiency compared to Xiran 40005, but showed better performance when used in lower concentrations. Xiran 25010 displayed significantly lower MC4R extraction capability (Fig. 2.7b).

In the further optimization process we focussed on Xiran 30010 polymer due to its better properties in lower concentration ranges. In order to avoid negative effects on further downstream processes due to excessive SMA concentrations we defined 2.5% as optimal SMA concentration for MC4R extraction from Tnao38 cells. This is also in line with reports from literature [48, 128–130]. For finding best solubilization conditions, environmental factors, such as ionic strength or pH have to be optimized as reported before [49, 50]. The effect of ionic strength was investigated by varying the NaCl concentration (Fig. 2.7c). Addition of increasing amounts of NaCl resulted in decreasing solubilization yields. Optimal amount of NaCl during solubilization is in a range between 150-300 mM.

In order to investigate the influence of pH on MC4R solubilization, we tested different pH and analyzed solubilization yields. The results show that yield is significantly lower when decreasing the pH from 8 to 7.5 or 7 (Fig. 2.7d). Increasing the pH to 9 does not lead to an increase in solubilization efficiency. The optimal pH for MC4R extraction from Tnao38 membranes by SMA is 8.

After optimizing the most important parameters for solubilization, we performed purification of MC4R with SMA. Membranes from Tnao38 cells expressing MC4R were used for larger scale solubilization and purification. Solubilization parameters were chosen as optimized before, final concentrations were 40 mg/ml membranes and 2.5% SMA, incubation was performed for 2 h at room temperature with gentle agitation [131]. The SMA extracted membranes were then subjected to affinity purification using Ni-NTA beads. Once, SMALPs are formed they are stable and do not require the addition of further polymer during purification. Figure 2.8 shows Coomassie stained gel and Western Blot using anti-FLAG tag antibody for detection.

No significant amount of receptor was detected in the flow through, indicating that the receptor was completely captured by the beads. The captured MC4R was eluted primarily in elution fractions 2-4 (Fig. 2.8a,b). Besides showing signal between 25 and 35 kDa (corresponding to monomeric MC4R), higher molecular weight migration of MC4R at 70 kDa was observed. This corresponds most probably to SDS-resistant dimers since protein samples were not boiled to avoid aggregation [132]. It was shown for GPCRs that they tend to migrate faster in SDS-PAGE due to their more compact shape after denaturation with SDS [133]. The presence of monomeric and dimeric forms of MC4R has been described for other GPCRs [134–136]. It has been shown that MC4R is able to form homodimers [137, 138]. Formation of dimers is supposed to be important for signal transduction [139]. The samples heterogeneity was assessed by negative stain electron microscopy (Fig. 2.8c). The resulting electron micrographs showed good particle distribution with mean diameters of particles of ~10 nm. However particles are rather heterodispers, which might be indication of collapsed or aggregated SMALPs. This outcome is in line with the SEC profile of MC4R-SMALPs (Fig. 2.8d) which also indicates that the particles are heterogenous in size distribution.

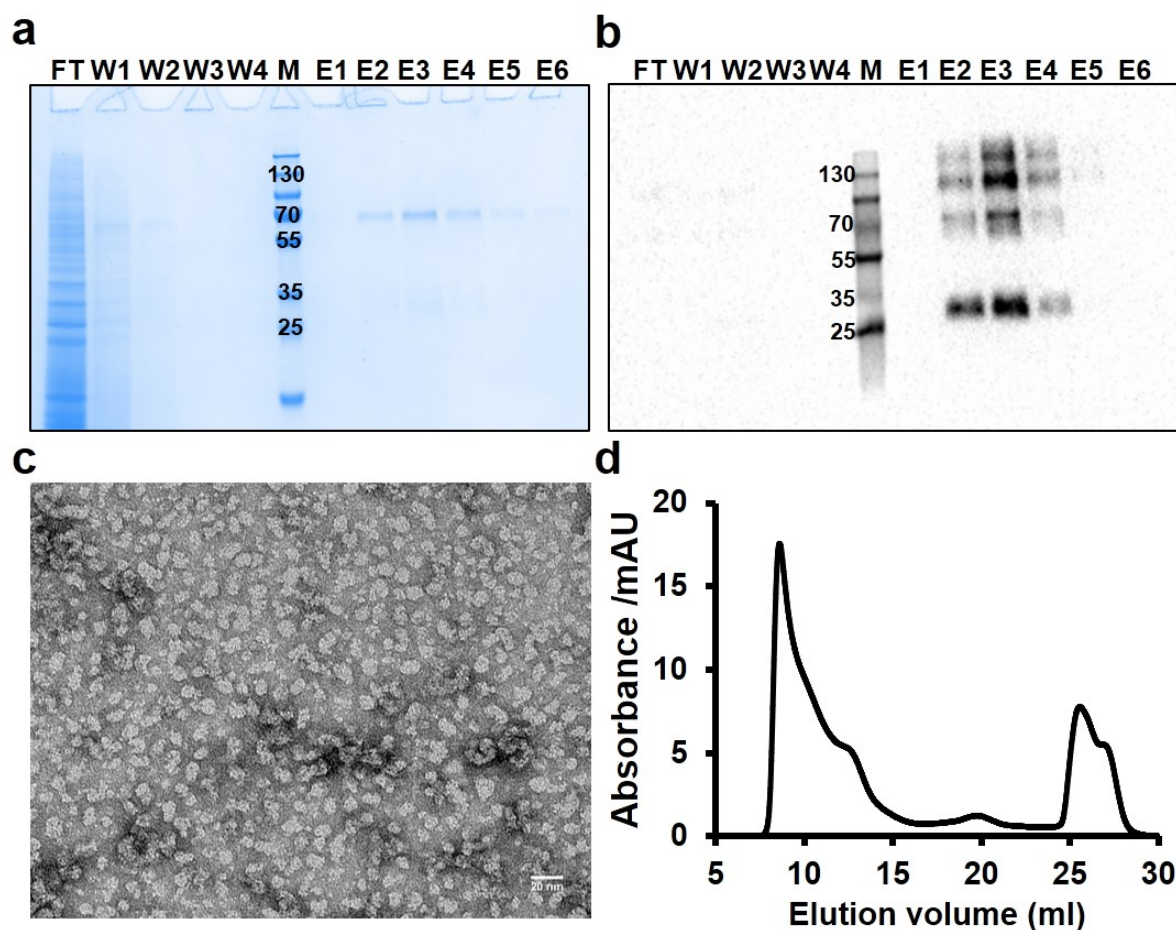


Figure 2.8: Purification of MC4R-SMALPs. SMA-solubilized fraction was purified by IMAC and analyzed by coomassie-stained SDS-PAGE (a) and Western Blot using anti-FLAG tag antibody (b). Abbreviations: FT, flow through; W, wash; E, elution. c) Representative negative stain micrograph of MC4R-SMALPs after IMAC. Scale bar represents 20 nm. d) Analysis of MC4R-SMALPs by size-exclusion chromatography using a Superdex 200 10/300 GL column with absorbance measured at 280 nm.

Overall, we could demonstrate the ability of styrene-maleic acid to solubilize Tnao38 membranes and the formation of MC4R containing lipid particles which could be purified via IMAC. However, further optimization work has to be done since the particles seem rather heterodispersers which makes a usage for biophysical characterization challenging.

2.5 Conclusion

In this study we were able to express MC4R in both HEK293 and insect cell lines. The use of the new cell line Tnao38 could further increase expression rates of MC4R as shown in Figure 2.1b. Insect cells provide a comprehensive folding machinery and provide post-translational modifications such as glycosylation. With the help of a FRET-based cAMP accumulation assay we could verify activity of receptor in HEK293 and insect cells and were able to characterize interaction of different ligands with MC4R. In comparison to Sf9 and Tnao38 cell lines, HEK293

cells turned out to be more suitable for monitoring signal transduction mediated by G-proteins (Fig. 2.6d). However, this is the first reported case of successful usage of Tnao38 cell line for cAMP-based activity assays.

Further we explored the potential of the SMA technology for the purification of MC4 receptor from baculovirus infected Tnao38 cell membranes. SMA solubilization is highly sensitive towards changes in environmental conditions. We found that salt concentrations in the range of 150-300 mM NaCl lead to most efficient solubilization whereas a high ionic strength decreases the efficiency. A certain ionic strength is needed to avoid repulsive electrostatic interactions between anionic membrane lipids and negatively charged SMA [49]. Salt ions shield this repulsion and accelerate solubilization. A (too) high ionic strength (< 300 mM NaCl) may lead to a reduced exposure of the hydrophobic styrene units which is essential for membrane binding and insertion. For Xiran 30010 the best solubilization efficiency was at pH 8. Decreasing the pH to 7 lead to a significantly reduced solubilization efficiency. SMA precipitates when pH of the solution is below the pK_a of maleic acid. At higher pH, electrostatic repulsion between the carboxylate groups dominate the hydrophobic effect and the polymer adopts a random coil formation that dissolves well in aqueous solutions [34].

Once the conditions for solubilization were optimized, we could use SMA for purification of MC4R from Tnao38 membranes (Fig. 2.8). IMAC could be performed successfully and MC4R could be found in different states in elution fractions. However, MC4R-SMALPs displayed heterogeneity in electron micrographs. Here, further optimization processes have to be performed to form more monodispers particles which then can be used for further downstream experiments.

3 Characterization of lipocalin 2 and its interaction with MC4R

3.1 Abstract

Melanocortin-4 receptor (MC4R) can be activated endogenously by binding of melanocyte-stimulating hormones (MSH), which leads to suppression of appetite (anorexigenic effect). In contrast, the agouti-related peptide (AgRP) suppresses MC4R signaling activity (orexigenic effect) since AgRP acts as an endogenous inverse agonist. MC4R plays a key role in the hypothalamic regulation of food intake and energy expenditure. Naturally occurring inactivating MC4R variants are the most common monogenetic cause underlying obesity. A recent study by Mosialou *et al.* reported that MC4R is activated by the bone derived hormone lipocalin 2 (LCN2) in mice as well as in HEK cells [140]. On the contrary, we show that neither human nor murine LCN2 trigger MC4R-dependent cAMP activity. In addition, we show that LCN2 does not influence activation of α -MSH suggesting that both molecules do not compete for the same binding site.

3.2 Introduction

Regulation of energy metabolism by bones

Bone fulfills a large variety of functions in vertebrates. Beside its key role as structural scaffold, it is also important as storage for minerals [141]. Since bone remodeling is an energy-consuming process a linkage has to be assumed to energy metabolism. It could be shown that anorexia nervosa, a state of low-caloric intake, is associated with osteoporosis in humans [142, 143], clearly indicating a relationship between energy intake and bone mass. Several hormones like leptin [144], insulin [145], adiponectin [146] and neuropeptides like NPY [147], orexin [148], AGRP [149] were identified to be involved in bone remodelling.

Recently, bone has been pointed out as an endocrine organ which regulates energy metabolism via secretion of bone-specific hormones, so called osteokines. This was shown first for the hormone osteocalcin, which is produced and secreted by osteoblasts and is involved in the regulation of glucose metabolism by influencing insulin secretion, insulin sensitivity and muscle function during exercise [145, 150–152]. There is at least one more osteokine that could be identified, the fibroblast growth factor 23 (FGF23) [153]. FGF23 acts on the kidney and is responsible for phosphate and vitamin D metabolism [154].

Lipocalin 2

Lipocalin 2 is a 24 kDa protein also known as neutrophil gelatinase-associated lipocalin (NGAL) due to its initial identification in association with neutrophil gelatinase [155]. Based on high

structural similarities to other lipocalin family members, it was originally thought to be the main function of LCN2 to be a carrier for small lipophilic compounds [156]. However, it could be shown that all proposed ligands have weak binding affinities [157]. The "true" native ligand of LCN2 was identified upon co-crystallization of LCN2 with enterobactin [158] which interacts with LCN2 through three positively-charged residues. This complex gave rise to the role of LCN2 as an antimicrobial protein that limits bacterial growth by preventing iron acquisition [158, 159]. Reports of immunological roles of LCN2 are quite frequent, such as the one by Zhang *et al.* by which LCN2 expression is upregulated in colorectal cancer patients [160]. It has also been reported that in response to inflammatory signals, LCN2 is expressed in epithelial cells [157].

LCN2 has been found in various states namely monomeric, as a homodimer, and as a heterodimer with matrix metalloproteinase-9 (MMP-9, 135 kDa) linked by a disulfide bond [157, 158, 161]. Structurally, LCN2 contains a signal peptide of 20 residues [155] enabling it to be secreted by the cell and a "lipocalin" domain, which structurally consists of an eight-stranded β -barrel with its loops running in an antiparallel direction, forming a barrel shaped structure. Due to non-polar residues (tryptophan, valine, phenylalanine) which are present in this region, this domain is able to bind small hydrophobic ligands like retinol, cholesterol oleate and oleic acid [162, 163].

Lipocalin 2 as a potential MC4R agonist

Recently Mosialou *et al.* revealed a previously unknown mechanism for regulation of energy metabolism. They reported that LCN2 is produced and secreted by osteoblasts and affects appetite and weight in mice [140]. Furthermore, Mosialou *et al.* showed that LCN2 crosses the blood-brain barrier, binds to MC4R in paraventricular nucleus (PVN) neurons of the hypothalamus and activates an MC4R-dependent appetite-suppressing pathway even though there is no sequence or structural similarity to any of the already known MC4R ligands. The potency of LCN2 should be comparable to the α -MSH analogue Melanotan II. Binding and activation could also be shown in cell culture experiments in which LCN2 dose-dependently induced cAMP activity in MC4R-expressing HEK293T cells [140]. Here, we wanted to reproduce this results to gain further knowledge about the interaction between LCN2 and MC4R.

3.3 Material and Methods

Cloning, expression and purification of LCN2

The human *LCN2* (hLCN2) gene was amplified from pUC57-hLCN2 (Sigma-Aldrich) using a primer pair designed for pGEX-6P-2 and pET-SUMO vector, respectively. The mouse *Lcn2* (mLCN2) gene was ordered as a DNA fragment (Thermo Fisher) and amplified using a primer pair designed for incorporation into pET-SUMO vector. The signal peptide coding sequence was removed from LCN2 constructs. The primers used for the respective constructs are shown in Table 3.1.

Table 3.1: List of LCN2 constructs and PCR primers. Primers are listed in 5'-to-3' orientation.

| Construct | Vector | Used primers, Forward (F) and Reverse (R) |
|------------|-----------|---|
| GST-hLCN2 | pGEX-6-P2 | F: GGGGCCCTGGGATCC, R: GTCGACCCGGAATTTTAACCATC |
| SUMO-hLCN2 | pET-SUMO | F: GAACAGATTGGTGGTCAGGATAGCACCAGCGATC, R: AGCAGCCGGATCTCATTAGCCATCAATGCACTGATCAATC |
| SUMO-mLCN2 | pET-SUMO | F: GAACAGATTGGTGGTCAGGATAGCACCAGCGATC, R: AGCAGCCGGATCTCATTAGCCATCAATGCACTGATCAATC |

For bacterial expression, *E. coli* BL21 (DE3) cells were used and cultivated in 2YT medium at 160 rpm. Protein production was induced at OD 0.5-0.8 with 1 mM IPTG and ran for 3 h at 37 °C.

GST-hLCN2 was purified as follows: Harvested cells were resuspended in 4-fold wet pellet weight of lysis buffer (50 mM Tris-HCl, pH 7.4, 150 mM NaCl containing a protease inhibitor tablet (cOmplete Mini, Roche)) and lysed by sonication with a VS70/T tip connected to a Bandelin Sonopuls sonicator (30% amplitude, 2 s ON, 2 s OFF, 5 minutes) on ice. Cell debris was pelleted at 16 000 *g* for 20 min at 4 °C. Subsequently, the supernatant was loaded on a pre-equilibrated GS Trap column (GE Healthcare) to deplete GST-tagged fusion protein from preparation. After extensive washes, GST-hLCN2 was eluted from the column by adding 10 mM reduced glutathione. Eluted samples were dialysed against PreScission cleavage buffer (50 mM Tris-HCl, pH 7.4, 150 mM NaCl, 1 mM Dithiothreitol), before PreScission Protease was added in 1:100 molar ratio for 4 h at 4 °C. GST-fusion protein was removed from the sample by re-chromatography on a GS Trap column, hLCN2 was pooled and concentrated using Vivaspin 20 (MWCO: 10 kDa, Sartorius) followed by size exclusion chromatography on HiLoad 16/600 Superdex 75pg (GE Healthcare). All the collected peak samples were pooled and concentrated in SEC buffer (20 mM sodium phosphate, pH 7.4, 50 mM NaCl).

SUMO-hLCN2 as well as SUMO-mLCN2 were purified similar as GST-hLCN2 with minor changes: Sodium phosphate buffer, pH 8 with 300 mM NaCl and 10 mM imidazole was used for IMAC. Cleared lysate was loaded on a HisTrap Excel column (GE Healthcare) to bind His-tagged fusion protein. After extensive washes, SUMO-hLCN2 was eluted from the column by increasing imidazole concentration to 250 mM. Eluted samples were dialysed against Sumo cleavage buffer (50 mM sodium phosphate, pH 8, 100 mM NaCl, 10 mM imidazole, 1 mM Dithiothreitol for 2 h at 4 °C, before SUMO protease was added in 1:10 molar ratio for 2 h at 30 °C. Protein samples were then subjected to reverse Ni-NTA chromatography, and concentrated using Vivaspin 20 (MWCO: 10 kDa, Sartorius) followed by size exclusion chromatography on HiLoad 16/600 Superdex 75pg (GE Healthcare). All the collected peak samples were pooled and concentrated in SEC buffer (50 mM sodium phosphate, pH 8, 100 mM NaCl).

HEK cell culture and MC4R expression

HEK293T cells were grown in DMEM supplemented with 10% FBS and 100 U ml⁻¹ penicillin and 100 µg ml⁻¹ streptomycin at 37 °C in a 5% CO₂ atmosphere. For transfection, cells were plated in a 10 cm dish at a density of 500 000 cells so as to be 90% confluent next day. 9 ml medium (DMEM supplemented with 10% FBS and 100 U ml⁻¹ penicillin and 100 µg ml⁻¹ streptomycin) were used per 10 cm dish. Next day, cells are transfected using lipofectamine 3000. 15 µl Lipofectamine 3000 reagent were mixed with 500 µl OPTIMEM reduced serum medium. Separately, 5 µg of MC4R expression construct and 20 µl P3000 reagent were mixed with 500 µl OPTIMEM reduced serum medium. Subsequently, both mixtures were combined, incubated for 10 min and then added straight to the plated cells in their 9 ml culture medium. 12 h later, transfection medium was removed and replaced with fresh DMEM supplemented with 10% FBS and 100 U ml⁻¹ penicillin and 100 µg ml⁻¹ streptomycin. Cells were incubated for further 36 h and then used for downstream experiments by dissociating them using an enzyme-free cell-dissociation buffer (Gibco, Life Technologies).

cAMP assay

cAMP assay was performed as described in Chapter 2.

NMR spectroscopy

All NMR experiments were performed on Bruker Avance III HD⁺ spectrometers operating either at 600 or 750 MHz, using standard 3 mm tubes and a ¹³C, ¹H, ¹⁵N triple-resonance probe head. Samples were measured in 50 mM sodium phosphate pH 7.4, 100 mM NaCl, supplemented with 10% D₂O and 0.02% NaN₃. Data was collected at 37 °C except stated otherwise and processed with TOPSPIN 3.5 (Bruker BioSpin) and NMRPipe. 4,4-dimethyl-4-silapentanesulfonic acid (DSS) was used as a chemical shift standard (100 µM in sample).

3.4 Results and Discussion

Human LCN2 does not activate human MC4R

The cDNA encoding hLCN2 without N-terminal signal peptide was cloned into pGEX-6P-2 expression vector to form pGEX-6P-2-hLCN2 construct with a PreScission protease cleavage site (Fig. 3.1a). The signal peptide is not included in the construct since it gets cleaved once the protein enters the secretory pathway. The expression of the construct was performed in BL21(DE3) *E. coli* strain and showed overexpression after induction with 1 mM IPTG (data not shown).

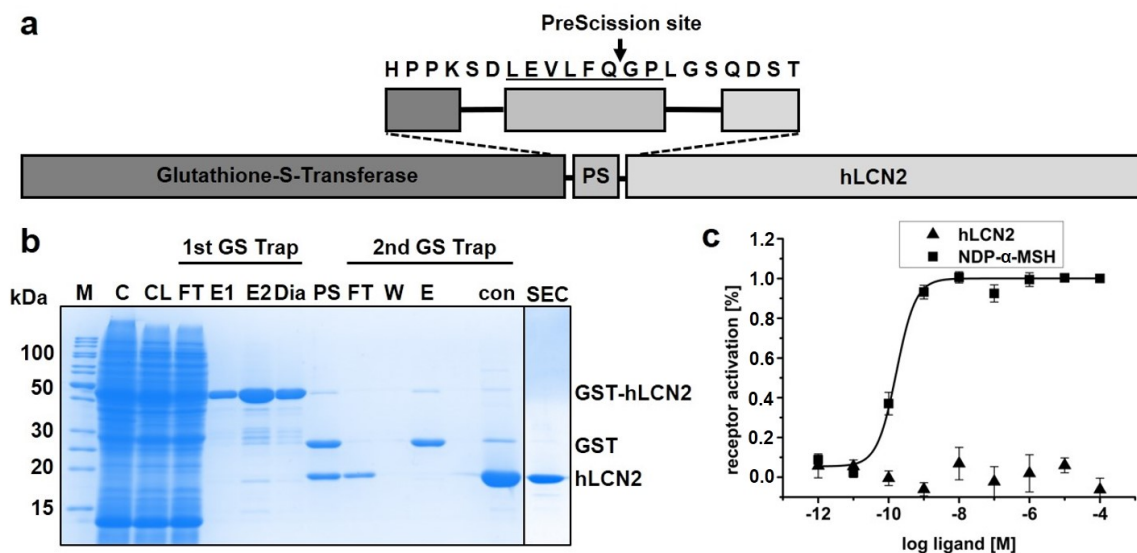


Figure 3.1: GST-hLCN2 construct, purification and functional characterization. a) hLCN2 construct contains an N-terminal glutathione-S-transferase (GST) tag and a PreScission protease cleavage site b) Coomassie-stained SDS-PAGE of GST-hLCN2 purification and cleavage. M, Marker; C, whole cell extract; CL, cleared lysate; FT, flow through; E1, E2, elution fractions 1 and 2; Dia, dialysis of elution fractions; PS, PreScission cleavage; W, wash fraction of second ac; E, elution fraction of second ac; con, concentrated hLCN2; SEC, hLCN2 gel filtration fraction. c) Functional activity of hLCN2 at recombinant hMC4R. HEK293F cells were stably transfected with hMC4R expression vector and stimulated for 30 min with increasing concentrations of ligands as indicated. Receptor activity is normalised to 1 μ M Forskolin-stimulated response. Experiment was repeated three times.

The fusion protein GST-hLCN2 was purified via affinity chromatography as shown in Figure 3.1b. The elution fractions showed only low content of impurities. GST-hLCN2 was predicted to be 47.4 kDa based on its sequence, which corresponds to its apparent molecular weight in SDS-PAGE (Fig. 3.1b). The cleaving efficiency using PreScission protease is above 90% and hLCN2 could be separated from GST-tag by reverse affinity chromatography. Remaining impurities could be removed by size exclusion chromatography resulting in pure hLCN2 protein that could be used for structural and functional studies.

3 Characterization of lipocalin 2 and its interaction with MC4R

In order to study the effect of hLCN2 on hMC4R, HEK293F cells recombinantly expressing hMC4R were incubated with recombinantly expressed hLCN2 and GPCR activation was monitored via detection of cAMP production in cells. The data show that hLCN2 does not activate the receptor in a manner which results in significant changes in the level of cAMP production (Fig. 3.1c). Contrary, stimulation with NDP- α -MSH leads to dose-dependent cAMP activity in hMC4R-expressing HEK293F cells with an EC₅₀ (half-maximal response) of 0.18 ± 0.04 nM. Note that NDP- α -MSH was used as positive control using the exact same assay conditions (cells, reagents, read-out).

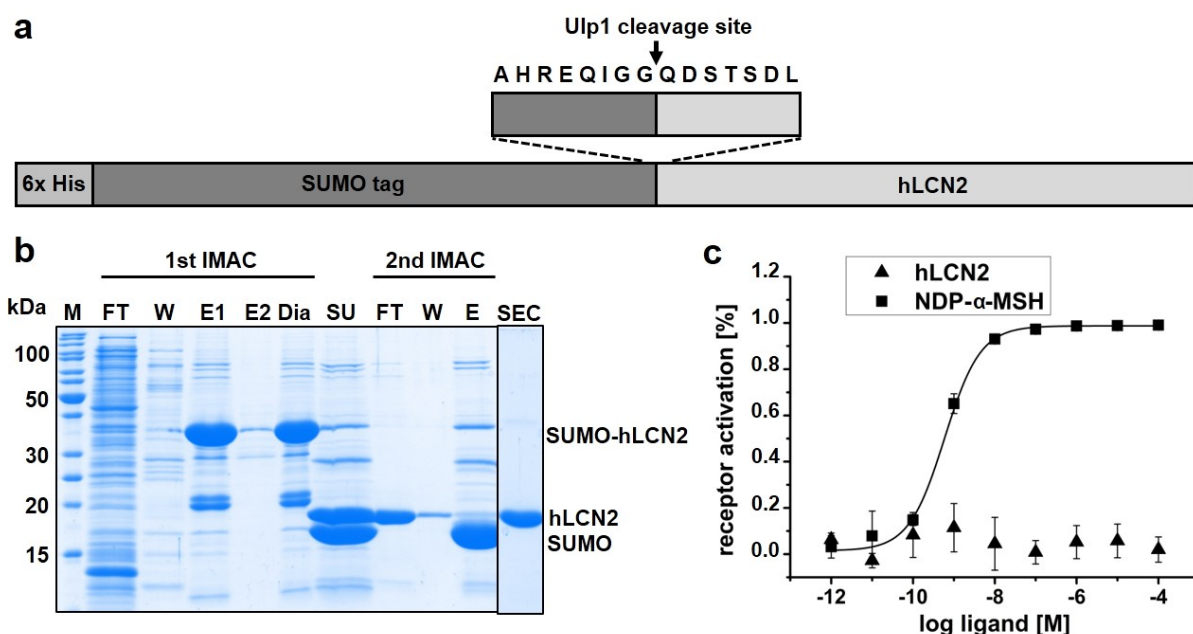


Figure 3.2: SUMO-hLCN2 construct, purification and functional characterization. a) hLCN2 construct contains an N-terminal Hexahistidin as well as a SUMO tag with a cleavage site for SUMO Protease (ULP1). b) Coomassie-stained SDS-PAGE of SUMO-hLCN2 purification and cleavage. M, Marker; FT, flow through; W, wash fraction; E1, E2, elution fractions 1 and 2; Dia, dialysis of elution fractions; SU, ULP1 cleavage; SEC, hLCN2 gel filtration fraction. c) Functional activity of hLCN2 at recombinant hMC4R. HEK293F cells were stably transfected with hMC4R expression vector and stimulated for 30 min with increasing concentrations of ligands as indicated. Receptor activity is normalised to 1 μ M Forskolin-stimulated response. Experiment was performed in triplicates.

These results are in strong contradiction to Mosialou *et al.* and it is not clear at this point, if the five amino acids at the N-terminus (GPLGS, Fig. 3.1a) deriving from cleavage site and multiple cloning site may have an impact on this result. To exclude that these 'artificial' residues hinder proper activation of hMC4R by hLCN2, we used a new construct in which hLCN2 is fused to small ubiquitin-related modifier (SUMO) sequence. In contrast to GST-fusion tag SUMO conjugation has the advantage of a clean cut with the UBL-specific protease 1 (Ulp1) without leaving fusion-derived amino acids on the cleaved protein (Fig. 3.2a) [164]. SUMO-hLCN2 was purified by Ni-NTA chromatography and gel filtration Fig. 3.2b. The result of the activity assay upon

incubation with previously produced hLCN2 can be seen in Figure 3.2c. It clearly indicates that (clean) hLCN2 has again no effect on cAMP production in hMC4R expressing cells.

Murine LCN2 does not activate murine MC4R

Mosialou *et al.* exclusively investigated MC4R-dependent cAMP production of murine LCN2 (mLCN2) [140]. Human and mLCN2 share a high degree of identity at the cDNA level and 62% identical amino acid homology (Fig. 3.3) [165]. The degree of similarity (79%) in amino acid sequence implies existence of conserved regions ensuring ligand specificity (Fig. 3.3) [158]. However, the human variant of LCN2 associates through a specific disulfide linkage, with matrix metalloproteinase-9 (MMP-9) [166]. The formation of this 135 kDa heterodimer stabilizes MMP-9 and thus increases its proteolytic activity [167]. Murine LCN2 lacks the corresponding cystein residue and is not known to interact with MMP-9 [157]. In regard to immune response it could also be shown that significant aspects of murine LCN2 cannot be applied to human LCN2 [168, 169]. Although major similarities exist between both variants there are important differences between human and murine LCN2 in their function.

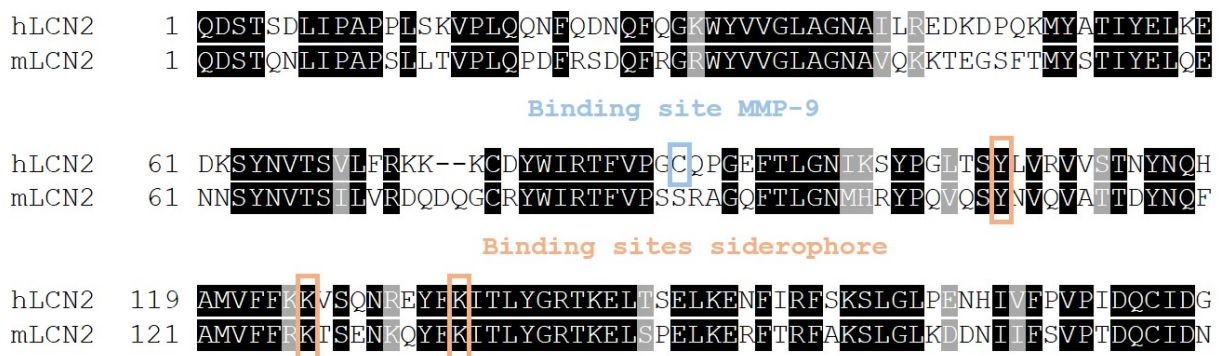


Figure 3.3: Protein sequence alignment of human and murine LCN2. The amino acid sequences of human and murine LCN2 are compared using Boxshade version 3.21. Black boxes indicate identical residues whereas conserved residues are shaded in grey. The binding motifs to siderophore and metalloproteinase-9 (MMP-9) are boxed with orange and blue squares respectively. LCN2 sequences included hLCN2: NP_005555; mLCN2: NP_032517. Note that LCN2 sequences in this work do exclude the signal peptide.

We decided to test murine LCN2 for murine MC4R (mMC4R) activation and cloned the cDNA of mLCN2 into pET-SUMO vector and produced the protein in the same way as the human variant. Equally, the cDNA of mMC4R was cloned into the same expression construct as the human variant. Human and murine MC4R amino acid sequence share 94% identity (Fig. 6.7), significant differences can be predominantly detected in the extracellular domain (positions 1-43).

In a first step, the ability of mLCN2 and α -MSH to activate hMC4R in HEK293F cell line was measured (Fig. 3.4a). For this purpose, we used both, the hMC4R expression construct as well as the recombinantly expressed mLCN2 that was used by Mosialou in their studies

3 Characterization of lipocalin 2 and its interaction with MC4R

[140]. Similarly, we tested activation on murine MC4R Fig. 3.4b. In both cases, α -MSH dose-dependently induced cAMP activity with an EC_{50} of 3.17 ± 0.3 nM (hMC4R) and 1.66 ± 0.1 nM (mMC4R). In contrast, mLCN2 did not show any agonist activity, neither at human nor at murine MC4R.

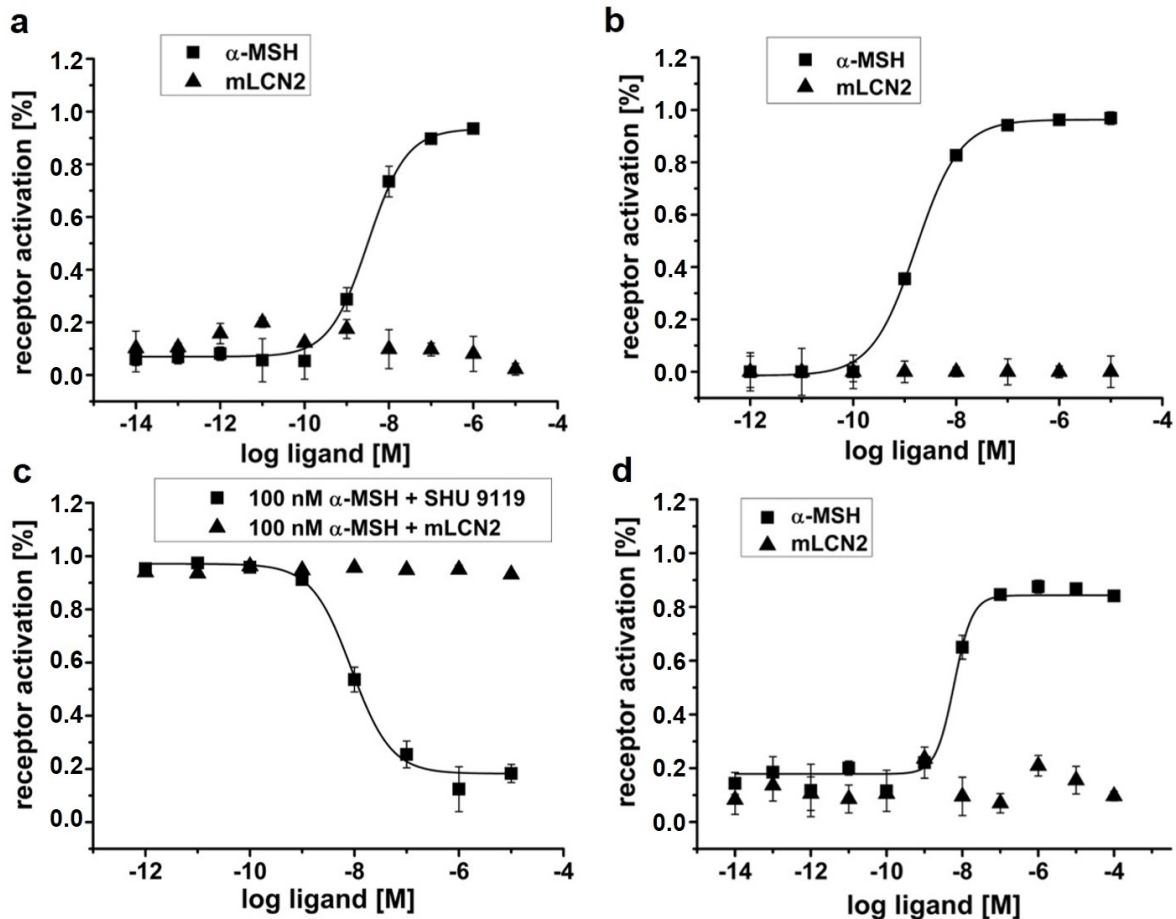


Figure 3.4: Functional characterization of murine LCN2 in HEK293-MC4R cells. Agonist (a, b, d) and antagonist (c) activity of mLCN2 at MC4R. HEK293F (a, b, c) and HEK293T (d) cells were transfected with hMC4R (a, d) and mMC4R (b, c) expression vector and stimulated for 30 min with increasing concentrations of ligands as indicated. a) HEK293F cells were transiently transfected with pCMV6-XL4 MC4R expression vector. Plasmid and mLCN2 were provided by Mosialou *et al.* [140]. Receptor activity is normalised to $1 \mu\text{M}$ Forskolin-stimulated response. Experiments were performed in triplicates.

To evaluate a possible antagonist activity of mLCN2, we measured the ability of the protein to inhibit the cAMP accumulation produced by 100 nM α -MSH in mMC4R expressing HEK293F cells. As positive control, cells were mixed with α -MSH (100 nM final concentration) and mLCN2 at increasing concentrations. As an initial proof of experimental principle, we incubated 100 nM α -MSH with increasing concentrations of the MC4R antagonist SHU 9119. The results are illustrated in Figure 3.4c. SHU 9119 is able to inhibit the activation that is induced by α -MSH

in a concentration-dependent manner, whereas mLCN2 does not affect the activation via α -MSH. This result shows that mLCN2 neither has an antagonistic effect on mMC4R nor any competitive effect on α -MSH binding to mMC4R.

Ultimately, we reproduced our results using the adherent HEK293T cell line, as they were used by Mosialou *et al.* [140]. A change of cell type also did not lead to MC4R activation by LCN2 (Fig. 3.4d).

LCN2 characterization

In order to prove the biochemical and structural integrity of LCN2, we produced isotope labelled protein and could obtain structural information of LCN2 using solution NMR. The ^1H - ^{15}N -HSQC NMR spectra of human and murine LCN2 are shown in Figure 3.5a,b.

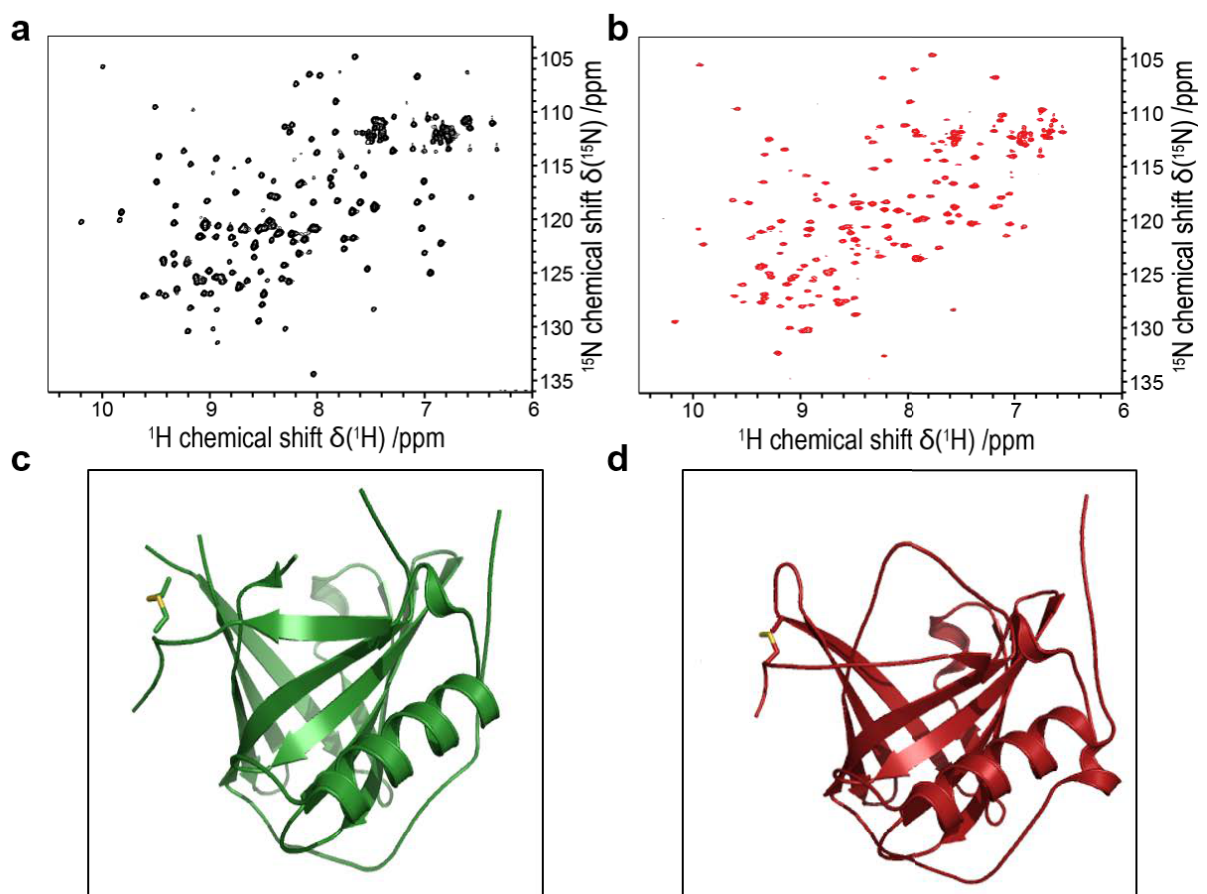


Figure 3.5: Structural comparison of human and murine LCN2. Comparison of [$^1\text{H};^{15}\text{N}$]-HSQC NMR spectra (a,b) and crystal structures (c,d) of murine murine (a,c) and human (b,d) LCN2. NMR measurements were taken on Bruker 700 MHz spectrometer, all samples were supplemented with 10% D_2O and DSS as reference. Crystal structures of mLCN2 (PDB: 3s26) and hLCN2 (PDB: 1l6m) are shown in cartoon representation, whereas disulfide bonds are depicted as yellow sticks. Images were generated with Pymol.

The observed dispersion of chemical shifts for both homologues indicates that both proteins are well folded. However, the chemical shift pattern of both proteins shows expected differences, given that the two sequences only share 62% identity (Fig. 3.3). Despite this discrepancy, the human and murine homologues show a very high degree of similarity in their three-dimensional structure as been illustrated by crystal structures of both proteins (Fig. 3.5c,d) which is also reflected by the overall comparable dispersion in the HSQC spectra (Fig. 3.5a,b). The high structural identity paired with the low level of sequence homology underlies the conserved function of the binding domain between different species.

Since LCN2 primarily binds bacterial siderophores, we wanted to figure out, whether possible ligand binding (i.e. enterobactin) to LCN2 has an effect on its activation of MC4R. With the help of electrospray ionization mass spectrometry a molecular mass of 20872 Dalton was analyzed. When calculated by the addition of average isotopic masses of the amino acids (protParam), LCN2 has a mass of 20874 Dalton. To get rid of any co-purified ligand, hLCN2 sample was unfolded by 6 M guanidinium hydrochloride, loaded on a desalting column to separate protein from any possible ligand and then refolded by dialysis [170]. The correct refolding of the protein was confirmed by 1D ^1H NMR spectra (Fig. 6.8). Refolded hLCN2 was tested for activation of hMC4R in HEK293F cells, but still no activation could be observed (data not shown). Taken together, there is no indication of misfolding after expression and purification of LCN2. Also, we could verify that there is no copurified ligand in LCN2 sample that could prevent proper MC4R activation.

3.5 Conclusion

It was possible to express and purify human and murine homologue of LCN2 with high purity. In parallel, MC4R from both organisms could be expressed in cell culture using HEK293 cell line. In order to monitor GPCR signaling, activation of MC4R with different ligands was tested and proven. This setup was then used to reproduce the results from Mosialou *et al.* [140]. However, neither using human constructs (Fig. 3.2) nor with the murine variants (Fig. 3.4), activation of MC4R by LCN2 could be confirmed. It was reported that in particular murine LCN2 is able to activate human MC4R in HEK293T cells. We tested this constellation (Fig. 3.2a) but did not observe any activation even when we used LCN2 sample and MC4R expression construct directly provided from the authors.

By contrast, the authors could show MC4R activation using our LCN2 protein (Fig. 3.2 and our pHLIRES-MC4R construct (Fig. 6.9). The onliest difference is the way of detecting activation.

In this study, an assay was used being based on the use of an antibody that specifically recognizes both intracellular cAMP and an exogenous labeled cAMP conjugate that acts as a competitor, followed by detection via FRET reaction (Fig. 1.2) [32]. Mosialou *et al.* used a reporter gene assay which monitors the downstream effects of cAMP. Here, a reporter gene was used that contains a cAMP response element (CRE) which in turn regulates the transcrip-

tion of luciferase, whose luminescence is used for readout [27]. Both assays have been used extensively to monitor characteristics of G_{α_s} -coupled GPCRs. It can be assumed that the reason for the completely different interpretations on MC4R activation by LCN2 lies in the fact that both assays work fundamentally different. FRET-based sensors are tools for direct measurement of cAMP implying a readout immediately after binding between cAMP and the sensor molecules. In contrast, reporter gene assays are indirect biosensors because there are several intermediary steps between actual cAMP concentration and the readout. One has to take into account the possible interference that may occur during downstream signaling, in particular, the potential for a response that is generated by more than one signaling pathway. Baker *et al.* discovered this phenomenon when characterizing the effect of different beta-blockers on β_2 -adrenoreceptor [171]. They showed that some beta-blockers are actually agonists of the receptor. The effects on cAMP level were small, while they were significant at the level of CRE-mediated gene transcription. The route between cAMP and CRE-mediated reporter genes via PKA was by-passed via the p42/44-MAP kinase pathway. This relates to the fact that ligands can simultaneously act as an inverse agonist through a G_{α_s} -coupled mechanism while stimulating an alternative G-protein-independent mechanism [171].

It is conceivable that MC4R may signal via a different pathway not detectable with the FRET-based assay used here. MC4R mainly signals through the activation of G_{α_s} , leading to a cAMP-dependent reaction [172]. However, there is more and more evidence that MC4R is using also different signaling pathways, such as the extracellular regulated kinase (ERK) pathway [173] or through binding to different G-proteins such as Gq [174]. It is reported that the latter might be involved in the anorexigenic effect of MC4R [175].

Based on our results, we can negate that LCN2 dose-dependently induces cAMP activity in MC4R-expressing HEK293 cells. We could also demonstrate that LCN2 does not influence activation by known MC4R ligands like α -MSH indicating, that both molecules do not compete for the same binding site. A recent publication by Heyder *et al.* addressed this issue and generated MC4R homology models as well as complexes with interaction partners [114]. Due to the lack of molecular data the authors were only able to visualize the spatial dimensions of both proteins. However they assume a completely different MC4R interaction mode compared to other peptide ligands [114]. There is neither a sequential nor a structural similarity between LCN2 and MC4R ligands like α -MSH and AGRP. Mosialou *et al.* speculated a RGRW motif in the LCN2 sequence to mimic the binding motif of α -MSH to MC4R [140]. In α -MSH the central recognition motif HFRW is involved in mediating ligand induced effects [114].

In a recently published study, the influence of LCN2 on Celastrol-mediated reduction of food intake and body weight [176]. Celastrol is a leptin-sensitizing agent and reported to be the most effective anti-obesity agent to date [177]. Even though LCN2 protein levels were strongly upregulated by celastrol, genetic deficiency of LCN2 altered neither the development of diet-induced obesity, nor the ability of celastrol to promote weight loss. Hence, the authors doubt the role of LCN2 as major influence on anorexigenic and anti-obesity signaling [176].

3 Characterization of lipocalin 2 and its interaction with MC4R

To date, neither the binding of LCN2 to MC4R nor its agonistic properties could be reproduced and still remain to be unclear. Our data strongly indicate that LCN2 does not directly activate the MC4R, both in the human and murine system.

4 SMALPs as a tool for lipid-peptide interaction

4.1 Abstract

Styrene-maleic acid (SMA) copolymer is a promising new tool in membrane research for solubilizing membranes. SMA acts as amphiphatic belt stabilizing lipids in the form of nanodiscs. Here, we investigate the potential of SMA lipid particles (SMALPs) to characterize lipid-peptide interaction. In a first step, we tested the solubilization of model membranes with different lipid composition by SMA resulting in homogenous particles with a diameter of 6 to 10 nm. Further, we demonstrate that microfluidic diffusional sizing allows characterization of lipid-peptide interaction using SMALPs highlighting new applications for SMA lipid particles.

4.2 Introduction

The amphiphilic copolymer Styrene-maleic acid (SMA) has emerged as an alternative to conventional detergents for solubilization of biomembranes [178]. SMA is able to form, similar to membrane scaffold protein (MSP), a novel class of nanodiscs, referred as SMALPs (SMA lipid particles) by forming a belt around lipid bilayers. Styrene unit acts as a hydrophobic moiety, maleic acid as the hydrophilic part [46]. In chapter 2, we demonstrated the capability of SMA to permeate cell membranes in order to form SMA lipid particles (SMALPs) that contain membrane proteins which can be used for further applications. Besides that, SMA has been shown to form SMALPs with synthetic lipids [179]. Depending on preparation, SMALPs have a size between 5 and 30 nm [34]. The most crucial advantage of the SMA method is the absence of detergent in the protocol, however they suffer from limitations. The biggest drawback of SMA is its pH limitation as it tends to aggregate at pH below 6.5 [50]. Moreover, SMA copolymer chelates divalent cations leading to precipitation which makes a usage under this conditions challenging. Unlike MSP-derived nanodiscs, lipids are stabilized by the copolymer and do not contain proteins. As a result, SMALPs should not interfere with protein specific detection properties, which makes SMALPs an attractive tool for investigation of protein interaction studies with lipids. One of these detection principles is the post separation labelling used by Fluidity One instrument (Fluidic Analytics). The fluorescent labelling relies on amine reactive dye and therefore is specific for proteins, preventing the use of MSP-derived nanodiscs.

4.3 Material and Methods

Preparation of vesicles and SMALPs

Vesicle formation and SMALP preparation was performed as described before [180]. DMPG and DMPC vesicles were formed by dispersion of dried lipids (Avanti) in the buffer (20 mM sodium phosphate, pH 7.4, 100 mM NaCl) to a final concentration of 25 mM. Lipid slurry was vortexed vigorously to mix completely and vesicles were formed spontaneously after ten freeze/sonication cycles (3 min each step). SMA polymer (Xiran 30010) was dissolved in the same buffer to a final concentration of 5% (w/v). SMALPs were formed by mixing SMA polymer and lipids in a 1:1 weight ratio. Samples were then mixed well by vortexing and equilibrated through two freeze/sonication cycles. Samples were equilibrated at room temperature overnight. Finally, SMALPs were purified by size exclusion chromatography on a HiLoad 16/600 Superdex 200 pg and a Superdex 200 10/300 GL column, respectively which were equilibrated with 20 mM sodium phosphate, pH 7.4 and 50 mM NaCl. SMALPs were concentrated using a Vivaspin concentrator with a 10 kDa MWCO.

Dynamic light scattering (DLS)

DLS was performed on a submicron particle sizer, Nicomp 380 (Particle Sizing Systems Nicomp, Santa Barbara, CA). Data were analyzed with the Nicomp algorithm using the volume-weighted Nicomp distribution analysis.

Microfluidic measurements

A Fluidity One instrument (Fluidic Analytics Ltd., Cambridge, U.K.) was used for microfluidic diffusional sizing measurements [181] with post separation labeling [182] using injection moulded disposable plastic chips.

4.4 Results and Discussion

Following previously described protocols [180], we assembled stable nanoscale lipid particles using anionic 1,2-dimyristoyl-sn-glycero-3-phospho-(1'-rac-glycerol) (DMPG) and neutral 1,2-dimyristoyl-sn-glycero-3-phosphocholine (DMPC) lipids as well as the styrene-maleic acid (SMA) copolymer as scaffold.

Figure 4.1a illustrates the assembly of SMA lipid particles (SMALPs) after addition of the copolymer to previously produced lipid vesicles. This process is supposed to follow a three-step model [34]: Initially SMA binds to the surface of the membrane, followed by the insertion into the hydrophobic core of the membrane which is driven by the hydrophobic styrene units. Finally, the membrane is solubilized and stable lipid particles are formed. The resulting SMALPs were characterized using size-exclusion chromatography (Fig. 4.1). SMALPs could be produced us-

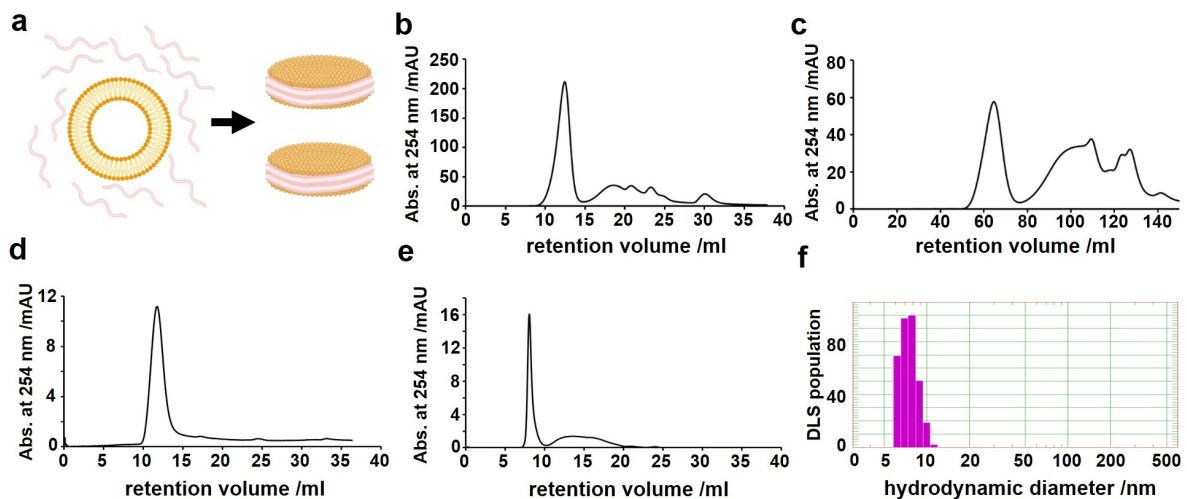


Figure 4.1: Preparation and characterization of SMALPs a) Schematic representation of assembled SMALPs after addition of SMA copolymer to vesicles. b-e) SEC analysis of different SMALP preparations. b) SMALPs formed with DMPC lipid (analytical scale). c) Preparative SEC of DMPG-SMALPs. d) Analytical SEC of DMPG-SMALPs after flash freezing with liquid nitrogen and storage at -20°C . e) Analytical SEC of DMPG-SMALPs after incubation with 5 mM CaCl_2 . f) Histogram of DMPG-SMALP particle sizes as determined via dynamic light scattering (DLS).

ing both DMPG and DMPC lipids. The particles elute at similar volumes compared to nanodiscs and non-assembled SMA copolymer could be separated (Fig. 4.1b,c).

We further characterized the hydrodynamic radius of the resulting particles using dynamic light scattering (DLS). The overall size distribution is in line with the expected SMALP properties with diameters from 6 to 10 nm (Fig. 4.1f).

In order to investigate the influence of storage capabilities conditions on DMPG-SMALPs, we performed SEC experiments after flash freezing with liquid nitrogen and storage at -20°C . The similarity of the resulting SEC profile (Fig. 4.1d) suggests that SMALPs can be frozen for storage, largely facilitating their handling and usage for various approaches.

Notably, SMA is known to chelate divalent cations [50]. We incubated DMPG-SMALPs with 5 mM CaCl_2 in order to test the stability. The resulting SEC profile (Fig. 4.1e) shows that the SMALPs indeed collapsed and elute within the void volume.

In a next step, we wanted to study the interaction of SMALPs with the MC4R ligand adrenocorticotrophic hormone (ACTH) using microfluidic diffusional sizing (MDS) which is particularly well suited for particles in the size range of SMALPs.

The principle of this type of measurement is that the diffusion of proteins and protein complexes in a laminar flow regime within a microfluidic channel is quantified (Fig. 4.2a). The amount of protein that diffuses across the channel perpendicular to the flow direction is quantified by measuring the concentrations at the two symmetric channel outlets. Large particles, such as SMALPs, require a comparatively slow flow rate, in order to provide enough time for a significant amount of diffusion to occur. Protein quantification is based on a latent fluorophore [182] which reacts with the primary amines of protein molecules after they have left the main channel, and which renders the proteins fluorescent.

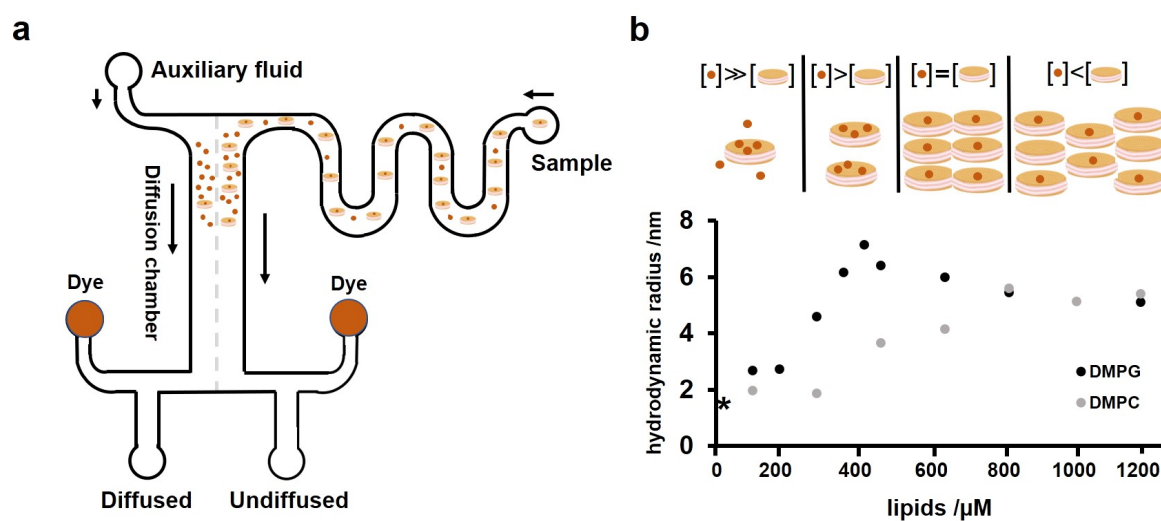


Figure 4.2: Binding of ACTH to SMALPs. a) Schematic representing the flow of a sample through a microfluidic chip during MDS analysis. b) Hydrodynamic radius of ACTH ($10\ \mu\text{M}$) upon titration with increasing amounts of SMALPs composed of DMPC (grey) and DMPG (black) using a microfluidic setup. Reference value of ACTH with lipids is indicated by an asterisk.

A crucial feature of SMALPs in context of interaction studies with MDS is that neither the DMPC and DMPG lipids nor the SMA copolymer are labelled by the fluorophore, thus only diffusion of ACTH is followed. Here, SMALPs prevail against MSP-derived nanodiscs which are labelled by the dye as well as liposomes which lack solubility and stability. Previously, NMR and fluorescence data indicated a charge dependent interaction of ACTH with lipids (unpublished data). To investigate the interaction, we titrated ACTH with increasing amounts of DMPG- and DMPC-SMALPs followed by determination of the hydrodynamic radius of the sample. Due to a lack of experimental data about the copolymer to lipid ratios in SMALPs, we quantified SMALPs with the initial amount of lipids used for SMALP assembly.

ACTH in the absence of lipids exhibited a radius of 1.7 nm. When incubating $10\ \mu\text{M}$ ACTH with increasing amounts of DMPG-SMALPs, a progressive increase from 2.67 nm to 7.13 nm could be observed when lipid concentration was increased to $400\ \mu\text{M}$ (Fig. 4.2b). At this condition, SMALPs bind ACTH up to their binding capacity resulting in SMALPs with a high number of ACTH molecules per disc. At lipid concentrations below $200\ \mu\text{M}$ unbound ACTH dominates the sample population and the determined size is almost identical to ACTH alone. Above DMPG concentrations of $400\ \mu\text{M}$, ACTH binds SMALPs in a 1:1 ratio and the radius slightly decreases to 5.09 nm ($1.2\ \text{mM}$) which corresponds to the size of SMALPs and one ACTH monomer. This also applies for conditions when SMALP concentration is larger than ACTH concentration.

Upon incubation with DMPC-SMALPs, radius increased to 5.84 nm (at $800\ \mu\text{M}$). In general, this result points to a lower affinity of ACTH to DMPC. However, since e.g. NMR measurements did not show interaction, it is likely that ACTH interacts with the copolymer. ACTH has a net positive charge associated with the basic amino acid residues at position 15 to 18 in the sequence [183] and can form electrostatic interactions with the maleic acid subunit which is partially deprotonated at pH 7.4 [50].

4.5 Conclusion

The formation of SMA lipid particles (SMALPs) from DMPC and DMPG lipids and SMA copolymer was successfully demonstrated. A weight ratio (lipid to copolymer) of 1:1 could completely dissolve lipid vesicles to form homogenous SMALPs with a diameter of 6 to 10 nm. Moreover, we could demonstrate the feature to store frozen SMALP stock solutions, simplifying handling and minimizing artifacts by batch-to-batch variations.

We show that microfluidic diffusional sizing (MDS) in connection with SMALPs is an effective method to investigate binding of proteins to different lipid types. As a proof of principle, we analyzed the binding of the MC4R ligand ACTH which was shown to bind to negatively charged lipids. Even though we could likely observe non-specific binding of ACTH to DMPC-SMALPs, presumably due to electrostatic interactions with SMA, we could detect stronger interaction when using DMPG-SMALPs demonstrating that the method is capable to detect lipid specificity of peptide-lipid interaction. The availability of a simple and reliable lipid screening assay is urgently needed in many areas of research.

For further optimization, optimized polymers with lower charge characteristics should be used to exclude non-specific binding of analyte to the polymer. Overall, SMALPs are a new membrane mimetic system that show great potential for investigation of biophysical studies of membrane associated proteins.

5 Interaction of α -Synuclein with α -Synuclein-derived lipoparticles

This chapter reflects content of the following publication.

5.1 Publication information

Title: α -Synuclein-derived lipoparticles in the study of α -Synuclein amyloid fibril formation

Authors: Marcel Falke, Julian Victor, Michael M. Wördehoff, Alessia Peduzzo, Tao Zhang, Gunnar F. Schröder, Alexander K. Buell, Wolfgang Hoyer, Manuel Etzkorn

Published in: **Chemistry and Physics of Lipids**, Vol. 220, pp. 57-65, 2019

DOI: 10.1016/j.chemphyslip.2019.02.009

5.2 Abstract

Aggregation of the protein α -Synuclein (α Syn) is of great interest due to its involvement in the pathology of Parkinson's disease. However, under *in vitro* conditions α Syn is very soluble and kinetically stable for extended period of time periods. As a result, most α Syn aggregation assays rely on conditions that artificially induce or enhance aggregation, often by introducing rather non-native conditions. It has been shown that α Syn interacts with membranes and conditions have been identified in which membranes can promote as well as inhibit α Syn has the intrinsic capability to assemble lipid-protein particles, in a similar way as apolipoproteins can form lipid-bilayer nanodiscs. Here we show that these α Syn-lipid particles (α Syn-LiPs) can also effectively induce, accelerate or inhibit α Syn aggregation, depending on the applied conditions. α Syn-LiPs therefore provide a general platform and additional tool, complementary to other setups, to study various aspects of α Syn amyloid fibril formation.

5.3 Introduction

The aggregation of the protein α -Synuclein (α Syn) into amyloid fibrills is associated with the pathology of Parkinson's disease. [68–73] Notably, purified α Syn on its own is kinetically stable in its intrinsically disordered, monomeric form, even at high concentrations and/or temperatures. Therefore, to study the process of α Syn amyloid fibril formation, experimental conditions are typically chosen under which aggregation is promoted. One frequently applied α Syn aggregation assay setup uses for example a glass bead inside the sample solution in combination with agitation of the sample [184, 185] resulting in strongly enhanced aggregation. Factors which

may promote α Syn aggregation in this 'glass-bead assay' (GB-assay) include (i) frequent scission of fibrils, constantly increasing the number of fibril ends available for elongation [186], and (ii) increased detachment of α Syn aggregates from the air-water-interface, where fibril nuclei preferentially form [187, 188]. GB-assays have been used/optimized by numerous groups and in many cases lead to improved reproducibility in the aggregation behavior, rendering them useful for the characterization of factors that for example interfere with α Syn aggregation [184, 189–192]. On the other hand, the intrinsic properties of the GB-assay can mask key processes of amyloid fibril formation. For example, the highly-induced fragmentation rate renders it difficult to detect other secondary processes, such as secondary nucleation on the fibril surface [193, 194]. Furthermore, the primary nucleation at the air-water interface impairs the quantification of the effects of other surfaces, such as liposomes [195] or nanoparticles [196] on the nucleation rate.

While its native function is not yet fully understood, α Syn is known to interact with membranes and a physiological role of α Syn in membrane-associated processes has been proposed [74, 75, 197, 198]. It has also been shown that the presence of lipids can modulate α Syn aggregation behavior [81, 82]. Using small unilamellar vesicles (SUVs) formed with anionic lipids, conditions have been identified that can enhance α Syn aggregation, providing a useful alternative to GB-assays [195]. We have recently shown that similar results can be obtained using lipid-bilayer nanodiscs formed with anionic lipids and the membrane scaffold protein MSP1D1 [83]. While both membrane mimetics can modulate α Syn aggregation in a similar manner, it appears that the presence of nanodiscs leads to the formation of fibrils with a morphology very similar to the ones formed in the absence of lipids [83], i.e. mature fibrils with diameters in the range of 8–10 nm. SUV-induced aggregation, on the other hand, leads to morphologically distinct short fibrils [195], which have been shown to convert into mature fibrils after heating to above 50 °C [199]. The application of nanodiscs and SUVs may therefore provide complementary information useful to disentangle the different processes involved in lipid-induced α Syn aggregation.

Interestingly, it has also been shown that α Syn, due to its amphipathic character, can stabilize lipid bilayers analogous to the membrane scaffold protein (MSP) [84, 85] and that stable α Syn-lipid particles (α Syn-LiPs) can be assembled *in vitro* using a similar approach as for nanodisc preparations [86, 87]. While the occurrence and possible physiological role of α Syn-LiPs is unclear, they may display useful features that could be exploited for *in vitro* studies.

Here we investigate the behavior of these α Syn-LiPs in α Syn aggregation assays. In line with results obtained on nanodiscs, we show that depending on the ratio of 'free' α Syn to α Syn-LiPs, the presence of the lipid particles can either inhibit or accelerate α Syn aggregation. In comparison to SUVs, α Syn-LiPs appear to be more stable, simplifying their handling. Additionally, the presence of α Syn-LiPs, in contrast to SUVs [199], does not noticeably alter fibril morphology and does not lead to kinetically trapped fibrils. In comparison to MSP1D1-derived nanodiscs, usage of α Syn-LiPs reduces the aggregation setup to a two-component system, simplifying sample preparation and eliminating potential effects of the membrane scaffold protein. Our re-

sults suggest that α Syn-LiPs may therefore be a useful complementary tool to study different aspects of lipid-induced α Syn aggregation.

5.4 Materials and Methods

α Syn and N-terminally acetylated α Syn expression and purification

α Syn in the pT7-7 vector was expressed in *E. coli* BL21 DE3. For acetylated α Syn, the N-terminal acetylation enzyme pNatB from *Schizosaccharomyces pombe* was coexpressed in a second vector, pNatB [200]. Expression was conducted in 50 mM phosphate buffered 2YT-medium (pH 7.2) with 0.4% glycerol and 2 mM $MgCl_2$, protein production was induced at OD 1–1.2 with 1 mM IPTG and ran for 4 h at 37 °C.

Purification of acetylated and non-acetylated α -syn was carried out as previously described [185], some changes to the protocol have been made. A cell pellet of 1 l culture was dissolved in 20 ml of 50 mM Tris-HCl pH 8, 150 mM NaCl, 5 mM EDTA containing a protease inhibitor tablet (cOmplete Mini, Roche) and cells were lysed by sonication with a MS72 tip connected to a Bandelin Sonopuls sonicator (30% Amplitude, 1.5 s ON, 3.5 s OFF, 5 min) on ice. Cell debris was pelleted at 15 000 g for 20 min at 4 °C. The supernatant was boiled at 95 °C for 15 min to precipitate unwanted proteins which were pelleted at 15 000 g for 20 min and 4 °C. After that, the supernatant was sterile-filtered and α Syn was precipitated by gradually adding 4 M ammonium sulfate solution until a concentration of 1.75 M was reached. α Syn was pelleted at 15 000 g for 20 min at 4 °C, the pellet was then dissolved in 20 ml of 50 mM Tris-HCl pH 8 and dialysed against 1.8 l of 50 mM Tris-HCl pH 8 overnight at 4 °C. Subsequently, α Syn was loaded onto a 5 ml HiTrap Q HP anion exchange column (GE Healthcare). Impurities were eluted by washing the column with 8 M Urea, 5 mM Dithiothreitol in 50 mM Tris-HCl pH 8, 100 mM NaCl for 30 min. α Syn eluted at around 250 mM to 300 mM NaCl in a 20-column volume gradient from 100 mM to 500 mM NaCl in 50 mM Tris-HCl pH 8. α Syn was then again precipitated with ammonium sulfate as described above, dissolved in an appropriate volume of 25 mM potassium phosphate buffer pH 7.4 and dialysed extensively against 1.8 l of the same buffer overnight at 4 °C. α Syn concentration was determined by measuring UV absorption at 275 nm and using an extinction coefficient of $5600 \text{ M}^{-1} \text{ cm}^{-1}$.

α Syn-Lip assembly

α Syn-LiPs were assembled according to established protocols [86]. In short, POPG or POPC lipids (Avanti) were suspended in lipid resuspension buffer (20 mM Tris-HCl pH 7.5, 100 mM NaCl, 60 mM Na-cholate, 5 mM EDTA) to a final concentration of 26 mM. Monomeric α Syn and lipids were mixed at a molar ratio of 1:40. 20% w/v of previously washed Biobeads SM-2 (Bio-rad) were added and the mixture was incubated at room temperature overnight. The Biobeads were removed by centrifugation and once again 20% w/v were added for an additional 4 h. Finally, α Syn-LiPs were purified by SEC on a HiLoad 16/600 Superdex 200 pg column or an-

alyzed using a 10/300 Superdex 200 column (GE Healthcare) equilibrated with 20 mM sodium phosphate pH 7.4. NaCl concentrations of 50 mM (low salt), 150 mM (medium salt) or 300 mM (high salt) were used at a flow rate of 1 ml min⁻¹ on an ÄKTA Pure FPLC (GE Healthcare). α Syn-LiPs were concentrated to the desired molarity using a Vivaspin concentrator with a 10 kDa MWCO. Where provided α Syn-LiP concentrations are calculated based on the α Syn absorbance measurements and the assumption of 8 α Syn molecules per α Syn-LiP.

MSP1D1-nanodisc preparation

Expression and purification of MSP1D1 as well as nanodisc assembly was carried out as reported before [83]. 100% POPG lipids and MSP1D1 after proteolytic cleavage of the Histidine tag were used for all MSP1D1 nanodiscs used in this study.

Thioflavin T (ThT) fluorescence aggregation assays

Influence of α Syn-LiPs on lipid-independent α Syn fibril formation (GB-assay)

In order to study the influence of α Syn-LiPs on α Syn fibril formation experimental conditions were chosen such that α Syn fibril formation occurs spontaneously by interface-driven nucleation and amplifies through fibril fragmentation. 25 μ M of acetylated α Syn were mixed with α Syn-LiPs at molar ratios of 8:1 (3.125 μ M α Syn-LiPs), 16:1, 64:1, and 128:1 in 20 mM potassium phosphate buffer pH 7.4 with 50 mM KCl, 0.05% NaN₃ and 10 μ M Thioflavin T (ThT). Duplicates of 80 μ l each were pipetted into half area 96-well plates with nonbinding surface (Corning No. 3881, black, clear bottom) containing a glass bead (2.85–3.45mm diameter, Carl Roth) for mixing and incubated at 37 °C for 5 days. Thioflavin T fluorescence was excited at 445 nm and measured at 485 nm every 20 min with 15 s of orbital shaking at 180 rpm prior to the measurement in a plate reader (Tecan Spark 10 M). Note that in order to provide a most accurate comparison between MSP1D1 ND and α Syn-LiPs, both were prepared in parallel under identical conditions, including assembly and SEC purification at NaCl concentrations of 150 mM (medium salt).

Nucleation-sensitive assays

We have previously reported that the presence of nanodiscs can accelerate nucleation of α Syn amyloid fibrils under conditions that minimize the intrinsic nucleation rate [83]. A similar setup, i.e. quiescent conditions and protein-repellent plate surfaces, was used to determine possible effects of α Syn-LiPs on the nucleation rate of α Syn. 25 μ M (final concentration) of acetylated α Syn was mixed with α Syn-LiPs at molar ratios of 4:1, 8:1, 16:1, 32:1, 64:1, 128:1, 256:1, 512:1, and 1024:1. Assays were performed in 20 mM sodium phosphate buffer pH 7.4 with 50 mM NaCl, 0.05% NaN₃ and 10 μ M Thioflavin T (ThT). Multiples of 30 μ l were pipetted into 384-well plates with nonbinding surfaces (Greiner 71900, black, non-binding). The samples were incubated at 37 °C in a plate reader (Tecan Spark 10M or Tecan infinite M1000PRO) for

up to 17 days during which aggregation was monitored by exciting ThT fluorescence at 445 nm and measuring emission at 485 nm every 20 min.

Microfluidic measurements

A Fluidity One instrument (Fluidic Analytics Ltd., Cambridge, U.K.) was used for microfluidic diffusional sizing measurements [181] with post separation labeling [182] using injection moulded disposable plastic chips. Triplicate measurements for each condition were performed and average hydrodynamic radii with standard deviation error margins are plotted. α Syn-LiPs concentrations were in the range of 1 μ M.

Dynamic light scattering (DLS)

DLS was performed on a submicron particle sizer, Nicomp 380 (Particle Sizing Systems Nicomp, Santa Barbara, CA). Data were analyzed with the Nicomp algorithm using the volume-weighted Nicomp distribution analysis. Additional data analysis is shown in Fig. 6.12. POPG α Syn-LiPs prepared under low salt conditions, directly after SEC elution were measured. Note that analysis shown in Fig. 5.1e identifies also a species of particle sizes >500 nm with a (volume) contribution of 0.03% that is not visible in the graph.

Fourier transform infrared spectroscopy (FTIR)

Infrared spectroscopy using the Direct Detect[®] system (EMD Millipore) was used to quantitatively determine the concentration of protein and lipids in the LiPs. The instrument uses a calibration via a BSA standard (Sigma) to quantify the protein abundance at multiple wavenumbers, including 1650 cm^{-1} . POPG lipid signal was calibrated manually using several dilutions of POPG in Na-cholesterol buffer. Signal from the C-H symmetric stretching vibrational populations between 2870 and 2840 cm^{-1} was used to quantify lipid signals (see Fig. 6.10 for data and more information).

Electron microscopy (EM)

Samples at different time points were used for EM studies. Freshly prepared α Syn-LiPs (concentrated to $150\text{ }\mu\text{M}$ α Syn) were flash frozen in liquid nitrogen after SEC elution (used for Fig. 5.3). In addition, samples after the ThT quiescent aggregation assays (Fig. 5.4) were collected from the respective assay wells (used for Fig. 5.5). All samples were kept at the used phosphate buffer, reducing possible preparation artifacts but leading to larger background staining artifacts. Negative stained samples were prepared on plasma-cleaned formvar-carbon-coated copper grids with a 2% uranyl acetate stain solution. Electron microscopy images were taken on a CM20 microscope operated at 200 kV.

Circular dichroism (CD)

The secondary structure of α Syn-LiP assemblies was determined using a J-815 spectropolarimeter (JASCO, Tokyo, Japan). Samples of α Syn-LiP assemblies were prepared in buffer containing 4 mM sodium phosphate, pH 7.4, 10 mM NaCl with the working concentration of LiPs at 4 μ M. For CD measurements, samples at 200 μ l were loaded into a 1 mm path length quartz cuvette and spectra were recorded from 195 to 260 nm, using a scanning speed of 50 nm min⁻¹ and a bandwidth of 2 nm, at 20 °C. The final spectrum of each sample was averaged based on 10 accumulations. The signal of the buffer was subtracted manually.

Native polyacrylamide gel electrophoresis (PAGE)

For gel casting 16%, 8%, and 4% acrylamide/bisacrylamide solutions (37.5:1, Carl Roth) were prepared in 250 mM Tris-HCl pH 7.4. Tetramethylethylenediamin (TEMED) and ammonium persulfate were added to a final concentration of 0.05% each. Afterwards, gels were immediately cast by layering the solutions over each other between two glass plates for polymerization with 16% acrylamide/bisacrylamide at the bottom (1.5 cm), 8% in the middle (4 cm), and 4% on top (1.5 cm). Samples were prepared by adding non-denaturing loading buffer (final concentrations 75 mM Tris-HCl pH 7.4, 10% glycerol, 0.02% bromophenol blue (w/v)). NativeMark™ Unstained Protein Marker (ThermoFisher Scientific) was loaded as a reference. The samples were separated by applying 25 mA per gel. Afterwards, gels were fixed in 10% ethanol, 3% phosphoric acid (v/v) for 15 min at room temperature and stained with colloidal Coomassie for at least one hour at room temperature (prepared from 0.02% Coomassie Brilliant Blue G-250 (w/v), 5% aluminium sulfate octadecahydrate (w/v), 3% phosphoric acid (v/v), and 10% ethanol (v/v)). Images were acquired using the ChemiDoc MP™ Imaging System (Bio-Rad).

Atomic force microscopy (AFM)

Samples were taken at the end of aggregation experiments, before or after centrifugation at 16 000 *g* for 30 min. The pelleted fibrils were resuspended in the same volume of PBS (10 mM Phosphate Buffer pH 7.4, 137 mM NaCl, 3 mM KCl, 0.02% NaN₃). Samples were diluted in PBS to a final concentration of 10 μ M and applied onto freshly cleaved mica for 5 min. Excess salt was removed by gently rinsing sample with water and dried with a slow flow of N₂. AFM images were taken in air, using a Nanowizard III atomic force microscope (JPK). Imaging was performed using tapping mode with a silicon cantilever with silicon tip (OMCL-AC160TS, Olympus) with a tip radius of 7 ± 2 nm and a force constant of 26 N m⁻¹.

5.5 Results and Discussion

Preparation and initial characterization of α Syn-LiPs

Following previously described methods [86], we assembled stable nanoscale lipid particles using anionic 1-palmitoyl-2-oleoyl-sn-glycero-3-phospho-(1'-rac-glycerol) lipids (POPG) and α Syn as scaffold protein. α Syn has been shown to be N-terminally acetylated in cellular environments and its acetylation is thought to act as an important mode of regulation of protein-membrane association [201,202]. Therefore, in addition to non-acetylated α Syn, which was used in the initial studies of *in vitro* lipid particle formation [86,87], we also tested lipid particle formation using acetylated α Syn. The resulting α Syn lipoparticles (α Syn-LiPs) were characterized using size-exclusion chromatography (Fig. 5.1). The α Syn-LiP preparations with the two different α Syn variants show very similar SEC profiles (Fig. 5.1a) confirming that acetylated α Syn can also form α Syn-LiPs. Since this variant is physiological more relevant, in particular in the context of lipid interactions, only acetylated α Syn was used for the following experiments. In general, both SEC profiles are in line with previous results in which α Syn-LiPs elute close to the void volume of the used Superdex 200 columns [86,87].

In order to investigate the influence of storage capabilities conditions on α Syn-LiPs, we performed SEC experiments after storage at 4 °C for one day, one week, as well as after flash freezing with liquid nitrogen and storage at -20 °C. The similarity of the resulting SEC profiles (Fig. 5.1b) suggests that α Syn-LiPs can be stored for several days at 4 °C or can be frozen for storage, largely facilitating their handling and usage for various assays.

Notably, α Syn is known to interact with negatively charged membrane surfaces [203–207]. This interaction is not driven by the net negative global charge, but rather by the partial positive charge in the N-terminal part of the protein. Therefore, when assembling α Syn-LiPs using anionic lipids it is unlikely that α Syn will only stabilize the hydrophobic edges of the lipid bilayer in the same manner as the membrane scaffold protein in the nanodisc system, but may also bind to the membrane surface (and/or partially insert at various positions in the bilayer). In order to decrease the electrostatic contributions of a potential α Syn membrane surface interaction, we increased the ionic strength of the buffer by changing the NaCl concentration from 50 mM (low salt) to 300 mM (high salt). SEC analysis of α Syn-LiPs, initially prepared using low-salt buffer and then incubated in high-salt buffer, shows that high-salt concentration results in dissociation of α Syn monomers from α Syn-LiPs (Fig. 5.1c, red). When reinjecting highsalt washed α Syn-LiPs, no further α Syn monomers are detached, suggesting that the remaining particles are stabilized predominantly by hydrophobic interactions (data not shown). When α Syn-LiPs are directly prepared in high-salt conditions using the previously reported α Syn-to-lipid molar ratio of 1:40 during α Syn-LiPs assembly, a high fraction of monomeric α Syn is again visible in the SEC profile (Fig. 5.1c, orange). Interestingly washing with 300 mM NaCl or full preparation in 300 mM NaCl leads to a comparable amount of α Syn monomers present in the sample. This suggests that, when using anionic lipids, the used protein-to-lipid ratio may not be optimal to effectively form disc-shaped particles in which the amphipathic properties of α Syn-helices are exploited

5 Interaction of α -Synuclein with α -Synuclein-derived lipoparticles

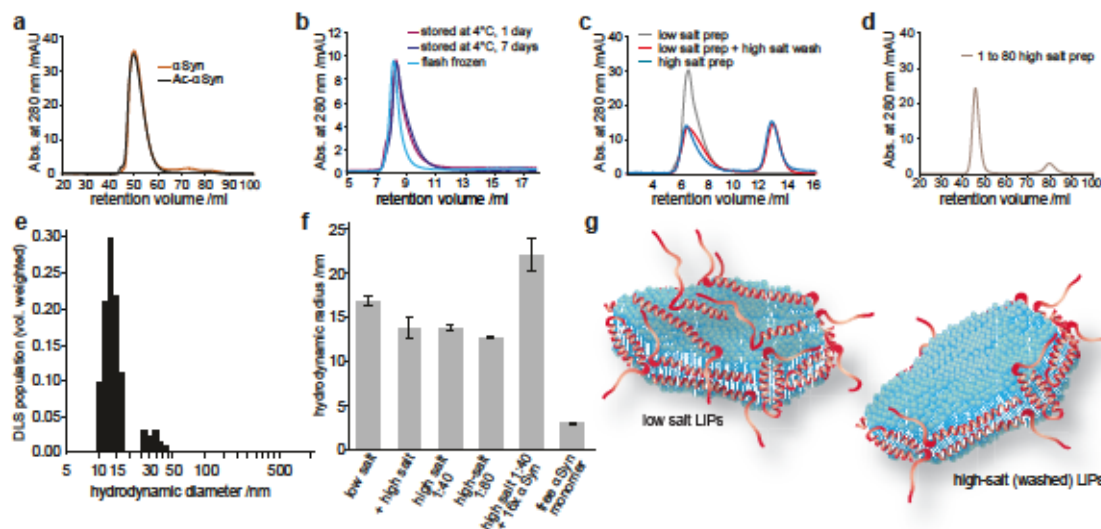


Figure 5.1: Preparation and characterization of α Syn-LiPs a-d) SEC analysis of different α Syn-LiP preparations. a) α Syn-LiPs formed with acetylated (black) and nonacetylated (orange) α Syn (preparative scale). b) Analytical SEC of acetylated α Syn-LiPs after storage for one day at 4 °C (purple) or one week at 4 °C (dark blue) or after flash freezing with liquid nitrogen and storage at -20 °C (light blue). c) α Syn-LiP preparation in low-salt conditions (grey). Same sample but after incubating and running in high-salt buffer (red) as well as α Syn-LiPs directly assembled in high-salt buffer (blue). d) α Syn-LiPs assembled in high-salt conditions with 2-fold more lipids per α Syn (i.e. molar ratio 1:80 - α Syn:POPG). e) Histogram of α Syn-LiP particle sizes as determined via dynamic light scattering (DLS). f) Measured hydrodynamic radii of indicated samples using a microfluidic setup (see text for more details). g) Possible model of α Syn-LiPs assembled with anionic lipids and either low-salt (left) or high-salt (right) conditions. Note that α Syn orientation at membrane edges is unknown.

to stabilize the hydrophobic membrane edges. While at a molar ratio of 1:40 (α Syn:lipid) nearly all α Syn is incorporated into α Syn-LiPs at low-salt conditions (Fig. 5.1c, black), only about half of the total α Syn is incorporated when electrostatic interactions are weakened at the same protein:lipid ratio (Fig. 5.1c, orange, red). We therefore also tested high salt α Syn-LiP formation at ratios with 2-fold increased excess of lipids, i.e. a protein:lipid molar ratio of 1:80. The resulting SEC profile (Fig. 5.1d, green) shows a considerably decreased fraction of monomeric α Syn as compared to high salt prepared α Syn-LiPs at protein:lipid molar ratios of 1:40 (Fig. 5.1c, orange). This data is in line with the picture that under conditions which lower membrane surface attachment (e.g. high salt or possibly also usage of neutral lipids), α Syn-LiPs are formed with roughly 2-fold less α Syn molecules per LiP.

To experimentally determine the protein-to-lipid ratio, we carried out quantitative Fourier Transform Infrared (FTIR) spectroscopy (see methods and Fig. 6.10 for more details). The data show a protein-to-lipid ratio of 1:35 for α syn-LiPs prepared at low-salt conditions. This value is very well in line with the previously estimated ratio of 1:40 [86]. When using α Syn-LiPs prepared under high-salt conditions, the ratio changes considerably to 1:105 consistent with the picture that the low-salt α Syn-LiPs carry a substantial amount of α Syn attached to the lipid surface via electrostatic interactions. According to the FTIR data about 2/3 of the protein may be in such a conformation in the low-salt α Syn-LiPs.

We further characterized the hydrodynamic radius of the resulting particles using Dynamic Light Scattering (DLS). While the resulting overall size distribution is in line with the expected

α Syn-LiPs properties, i.e. rather heterogenous particles with diameters from 10 to 44 nm (Fig. 5.1e), the sample heterogeneity renders accurate particle sizing via DLS, in particular when applying polydisperse data analysis, rather unreliable (see Fig. 6.12 for more details). This complicates detection of presumably small variations of particle sizes due to changing conditions as e.g. induced by attachment of monomers to preformed α Syn-LiPs. However, the DLS data are consistent with the particles sizes also seen in negative stained electron microscopy (EM) of the same samples (vide infra).

To more reliably detect smaller changes on the particle sizes, we used microfluidic diffusional sizing as an emerging alternative to DLS [181], which is particularly well suited for particles in the size range of α Syn-LiPs. The principle of this type of measurement is that the diffusion of proteins and protein complexes in a laminar flow regime within a microfluidic channel is quantified. At the entrance of the channel, one half is filled with water and the other half with protein solution. Laminar flow ensures that no turbulent mixing occurs and the two fluid streams stably flow in parallel. The amount of protein that diffuses across the channel perpendicular to the flow direction is quantified by measuring the concentrations at the two symmetric channel outlets. Large particles, such as α Syn-LiPs, require a comparatively slow flow rate, in order to provide enough time for a significant amount of diffusion to occur. Protein quantification is based on a latent fluorophore [182] which reacts with the protein molecules after they have left the main channel, and which renders the proteins fluorescent.

Regularly-prepared (low salt+flash frozen) α Syn-LiPs display a hydrodynamic radius of 16.9 ± 0.6 nm (Fig. 5.1f). When measuring high-salt-washed α Syn-LiPs after SEC separation of monomeric α Syn, a hydrodynamic radius of 13.8 ± 0.4 nm is obtained, which most likely reflects the actual size of α Syn-LiPs without membrane surface-attached α Syn. Consistently, a comparable hydrodynamic radius of 12.7 ± 0.2 nm is detected for α Syn-LiPs assembled with a protein:lipid molar ratio of 1:80 in high-salt conditions. Note that the used SEC column (Superdex 200) displays a rather limited separation efficiency in this size regime, explaining why no size difference was detected in the respective SEC profiles.

We additionally tested whether monomeric α Syn, which shows a hydrodynamic radius of 2.9 ± 0.1 nm, attaches to high-salt-washed α Syn-LiPs (in low-salt conditions). Indeed, the addition of 16-fold molar excess of monomeric α Syn (16 α Syn monomers added per LiP) significantly increased the hydrodynamic radius of the particles to 22.1 ± 1.8 nm. Note that the microfluidic measurement yields the average hydrodynamic radius of all particles in the sample. The presence of larger amounts of free monomeric α Syn molecules would therefore lead to an apparent decrease in measured hydrodynamic radius of the sample. The measured value of 22.1 nm consequently suggests that a large fraction of the added α Syn monomers attaches to the α Syn-LiPs. Since the size of the '16-fold loaded' α Syn-LiPs is considerably larger than the size of the α Syn-LiPs formed at low ionic strength, the microfluidic diffusional sizing data also suggest that low salt α Syn-LiPs still have unoccupied binding sites for α Syn on the membrane surface.

In general, α Syn-LiPs which have not been in contact with a high ionic-strength solution are well-suited for further usage in different assays (vide infra), however one should keep in mind

that these (low salt) α Syn-LiPs are formed with a higher number of α Syn per particle compared to those formed in, or washed with, higher ionic-strength buffer. While it is not fully clear where these additional α Syn molecules are located, binding to the lipid bilayer surface, i.e. interaction with the negatively-charged lipid head groups, would be one simple explanation consistent with the data obtained in this study. It should be highlighted that this also suggests that the estimation of the α Syn-LiP concentration based on measurements of the α Syn absorbance will be altered due to the different amounts of α Syn per particle at different ionic strengths. It is important to take this aspect into consideration, in particular for quantitative measurements of aggregation kinetics.

α Syn-LiPs in aggregation assays

Using a similar setup as reported for MSP1D1-derived nanodiscs (NDs) [83], we explored the influence of α Syn-LiPs on α Syn amyloid-fibril formation. Initially we used a conventional GB-assay that reports on the effect of α Syn-LiPs on the lipid- independent α Syn aggregation pathway. To directly compare the results of α Syn-LiPs to the previously characterized effects of NDs [83] we prepared NDs and α Syn-LiPs in parallel and performed a GB-assay simultaneously for both systems on the same 96-well plate (Fig. 5.2). Depending on the ratio of added α Syn monomers to either α Syn-LiPs or to NDs, both lipid systems can either inhibit aggregation or accelerate aggregation (Fig. 5.2a,b). Interestingly while a ratio of 16 added α Syn monomers per ND leads to an aggregation-accelerating behaviors (Fig. 5.2a, 16:1), the same ratio is in the inhibiting regime in the case of α Syn-LiPs (Fig. 5.2b, 16:1). This is well in line with the increased size of the α Syn-LiPs as compared to MSP1D1 NDs as well as the α Syn lipid-binding modes identified in our previous study [83].

In general, anionic lipids in liposomes or in nanodiscs are capable of inducing primary nucleation of α Syn [83,195]. To investigate whether anionic lipids in α Syn-LiPs also show nucleation-inducing properties, we investigated α Syn-LiPs with 100% POPG lipids via negative stain electron microscopy (EM). Surprisingly, the α Syn-LiPs already show directly after their SEC elution, in addition to the expected disc-like particles (Fig. 5.3a), the occurrence of thin fibrillar structures (Fig. 5.3b). While the amount of fibrils is difficult to quantify via EM, the polydisperse DLS data analysis (Fig. 5.1e) reports a fraction of (only) 0.03% very large particles (> 500 nm, 0.03% volume weighted, 16% intensity weighted, also see Fig. 6.12). Since the SEC elution peak itself appears directly after the void volume of the used column, the respective samples were flash frozen in liquid nitrogen directly after SEC elution, and EM data was directly recorded after a short thawing step, it is likely that the fibrillar structures already formed during α Syn-LiP assembly, which is a rather slow process, e.g. due to the prolonged incubation with Biobeads for detergent removal. To investigate whether the fibrillar structures are induced by the anionic lipids or are just an artifact of the α Syn-LiP assembly process itself, we also prepared α Syn-LiPs containing 100% 1-palmitoyl-2-oleoylglycero-3-phosphocholine (POPC) lipids. The POPC α Syn-LiPs were prepared in parallel to POPG α Syn-LiPs. EM data recorded after SEC elution

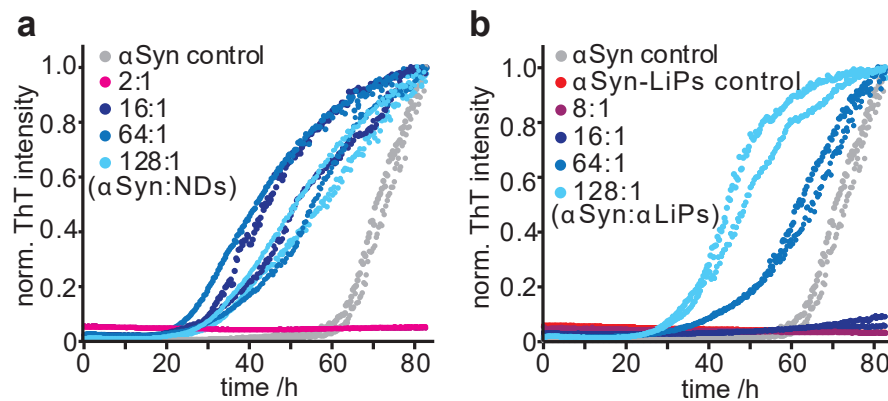


Figure 5.2: α Syn-LiPs in direct comparison to classical MSP-derived nanodiscs as a tool in aggregation assays. Comparison between MSP1D1 NDs a) and α Syn-LiPs b) in a GB-aggregation assay. α Syn aggregation kinetics, as measured by increase in ThT fluorescence, in the absence of NDs/LiPs (grey) and in the presence of indicated ratios of monomeric α Syn per NDs a) or per α Syn-LiP b) are shown. Note that monomeric α Syn concentration is kept constant and α Syn-LiP particle concentration was estimated assuming an average of 8 α Syn proteins per LiP as reported before [86]. Duplicate measurements are shown with same color. Both the ND and the α Syn-LiP system are able to inhibit as well as to accelerate α Syn aggregation as compared to α Syn in the absence of lipid particles (grey). However, the ratios of added α Syn monomers per lipid particle that lead to inhibiting or accelerating behavior differ between α Syn-LiPs and NDs.

(Fig. 6.11) do not show any fibrillar structures for POPC α Syn-LiPs in two different samples and over 20 different scan regions (Fig. 5.3c provides one example).

We also characterized the respective POPG and POPC α Syn-LiPs via circular dichroism (CD) spectroscopy (Fig. 5.3d). The resulting CD spectra of the two samples are very similar and in line with the expected secondary structure, i.e. an amphipathic α -helix for first approx. 100 residues and random coil conformations for the remaining C-terminal residues, as seen in NMR spectra of comparable α Syn-LiPs [86]. Note that the remaining small deviation between the two CD spectra would also be in line with a very small population of β -sheet rich fibrils in the POPG α Syn-LiPs sample.

Overall, our data suggest that POPG α Syn LiPs after SEC elution already contain a small fraction of fibrillar structures, which were induced by the presence of anionic lipids. Having a closer look at the fibrillar structures in the EM images shows that to some extent the fibrils colocalize with α Syn-LiPs (Fig. 5.3e,f). In general, it cannot be fully excluded at this point that α Syn-LiPs and fibrils cluster during the drying process on the EM grid. However, such a clustering should in principle result in α Syn-LiPs appearing at random positions on the fibrils. While such connections are also observed, a rather large fraction of fibrils appear to 'grow out' of the LiPs. Such defined start/end points may indeed suggest that the EM images captured early stages of lipid induced α Syn aggregation.

Interestingly, it has been shown that α Syn can also reshape lipid vesicles into lipid nanotubes consisting of either a monolayer of lipids (micellar tubes) or of a lipid bilayer in a cylindrical arrangement [84]. The observed fibrillar structures also share some similarities with these micellar lipid tubes. While it is difficult to distinguish small protein fibrils from lipid tubes in the negative stained EM images, amyloid-fibril-specific ThT fluorescence increase can be used to

5 Interaction of α -Synuclein with α -Synuclein-derived lipoparticles

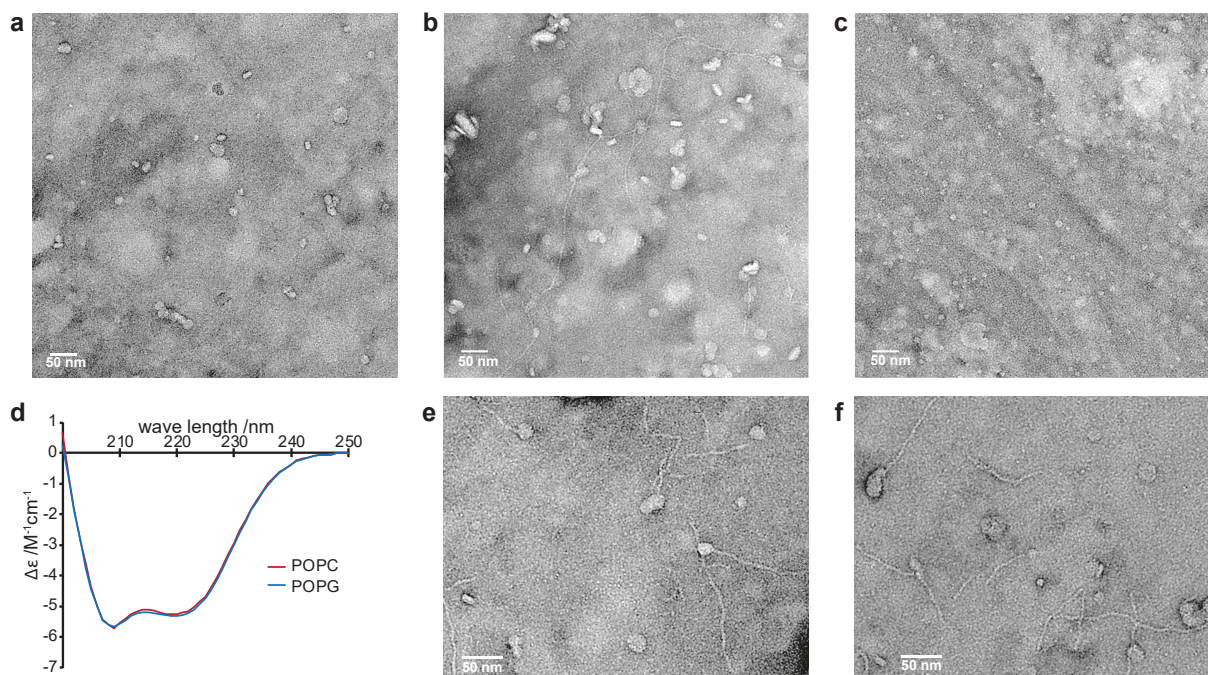


Figure 5.3: α Syn-LiPs properties after SEC elution. a) EM image of POPG α Syn-LiPs. b) Different region of the same sample as in a) showing occurrence of thin fibrillar structures. c) EM image of POPC α Syn-LiPs, no fibrillar structure was detected in this or any other region of the sample as well as in repetition experiments. d) CD spectra of the POPC (red) and POPG (blue) α Syn-LiPs (same condition as used for the respective EM images). e, f) Zoom into selected regions in POPG α Syn-LiPs showing possible connections between α Syn-LiPs and fibrils.

distinguish between the two species, once sufficient fibrils are formed. In order to test whether nucleation-inducing properties of POPG α Syn-LiPs can be monitored via ThT aggregation assays, we performed additional ThT assays under conditions that do not promote the formation of detectable quantities of amyloid fibrils in the absence of LiPs. Such a setup is provided by using quiescent assay conditions (no glass beads, no shaking) [195]. The absence of a glass bead facilitates usage of smaller sample volumes. We therefore carried out the assay using a volume of 30 μ L per well in a 384-well plate format. In general, we observed that this assay has limitations in reproducibility and shows variations in the ThT profiles of wells with the same conditions in particular in respect to total ThT fluorescence intensity. In general, reproducibility in α Syn aggregation assays is a well-known challenge [185]. It is therefore not unexpected that the rather slow kinetics observed in the α Syn-LiP nucleation assay also propagates detectable differences in wells replicating the same conditions. However, the assay format also facilitates usage of a higher number of replications for each condition. We therefore carried out 5 replications for each condition and the resulting ThT profiles show a clear trend, despite their intrinsic variation. Our data show that (i) α Syn does not aggregate in the absence of α Syn-LiPs (Fig. 5.4a), (ii) α Syn-LiPs on their own do not form ThT-detectable amyloid fibrils (Fig. 5.4b), (iii) α Syn-LiPs can induce amyloid fibril formation at specific ratios of α Syn to α Syn-LiPs (Fig. 5.4c), and (iv) α Syn-LiPs formed with neutral POPC lipids do not induce aggregation at any of the tested α Syn to α Syn-LiPs ratios (Fig. 5.4d).

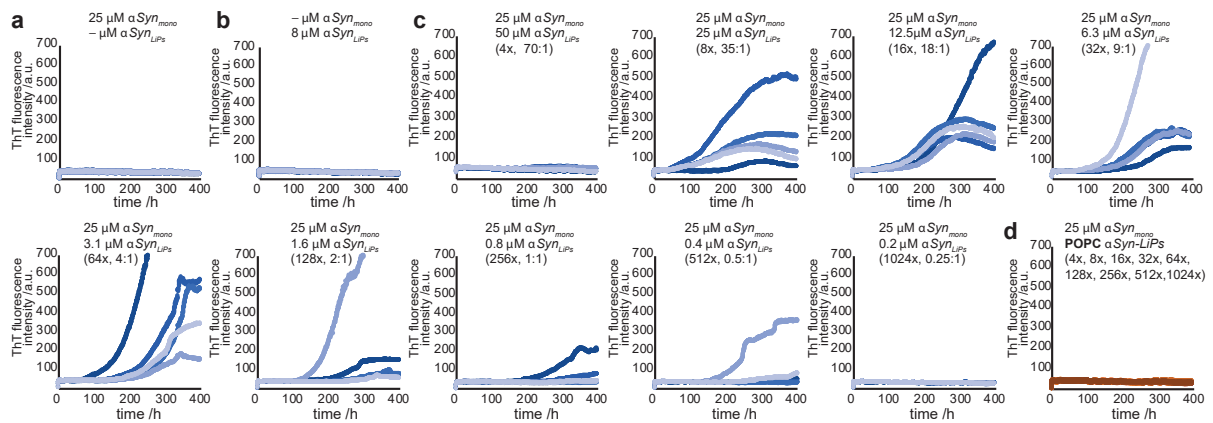


Figure 5.4: α Syn-LiPs can induce primary nucleation. a–d) ThT aggregation assays under quiescent conditions. Under these conditions neither aggregation of α Syn in the absence of α Syn-LiPs a) nor of α Syn-LiPs on their own b) is observed. Each plot contains data of five replications of the indicated condition. c) Variation of α Syn-LiP level in the presence of constant monomeric α Syn starting concentrations. In addition to concentration of monomeric α Syn, also the concentration of α Syn in LiPs is provided for each plot. Numbers in parentheses refer to estimated excess of monomeric α Syn over α Syn-LiP particles (assuming an average composition of 8 α Syn per LiP [86]). In addition, the respective molar ratios of lipids to added monomeric α Syn are given. d) All conditions as shown in c) but using POPC α Syn-LiPs (all 45 curves are shown in one plot).

Note that α Syn-LiPs showing fibrillar structures were used as starting material for the aggregation assays (Fig. 5.4b,c). In case the fibrillar structures represent protein fibrils and not lipid tubes, it would be likely that the fibrils can act as seeds in the aggregation assay. The shape of the resulting kinetic profile however still shows a long lag phase, indicative of primary nucleation events, in all conditions resulting in ThT-detectable fibrils. The time frame of the corresponding lag phase is also considerably larger than the sample preparation time before the assays, suggesting that a potential seeding effect originating from the pre-existing fibrillar structures is rather small. Considering that all negative controls consistently do not show any ThT increase, it can be stated that α Syn-LiPs containing anionic lipids induce primary nucleation.

Interestingly, ThT assays carried out using SUV preparations with comparable lipid composition show induction of primary nucleation at comparable lipid: α Syn (monomer) ratios [195]. However, SUVs did not induce detectable aggregation at the used NaCl concentration of 50 mM, even at higher α Syn concentration [195]. This observation suggests that α Syn-LiPs show similar properties as SUV and may be even more potent in inducing primary nucleation than SUVs. However, a more thorough mechanistic analysis beyond the scope of this work will be required to quantify the kinetic rate constants as well as the molecular determinants of α Syn-LiPs-modulated α Syn aggregation. While the contributions of potential nucleation events prior to the start of the assay may or may not complicate data analysis, our data demonstrate that α Syn-LiPs provide an interesting tool in the investigation of lipid-induced α Syn aggregation.

To obtain insights into the sample properties at the end points of the aggregation assays, we recorded AFM and EM images of selected samples. Our data show that extended fibrils with a morphology comparable to α Syn fibrils obtained in regular GB-assays have been formed in the presence of α Syn-LiPs (Fig. 5.4a–d). Note that the samples were obtained in conditions in

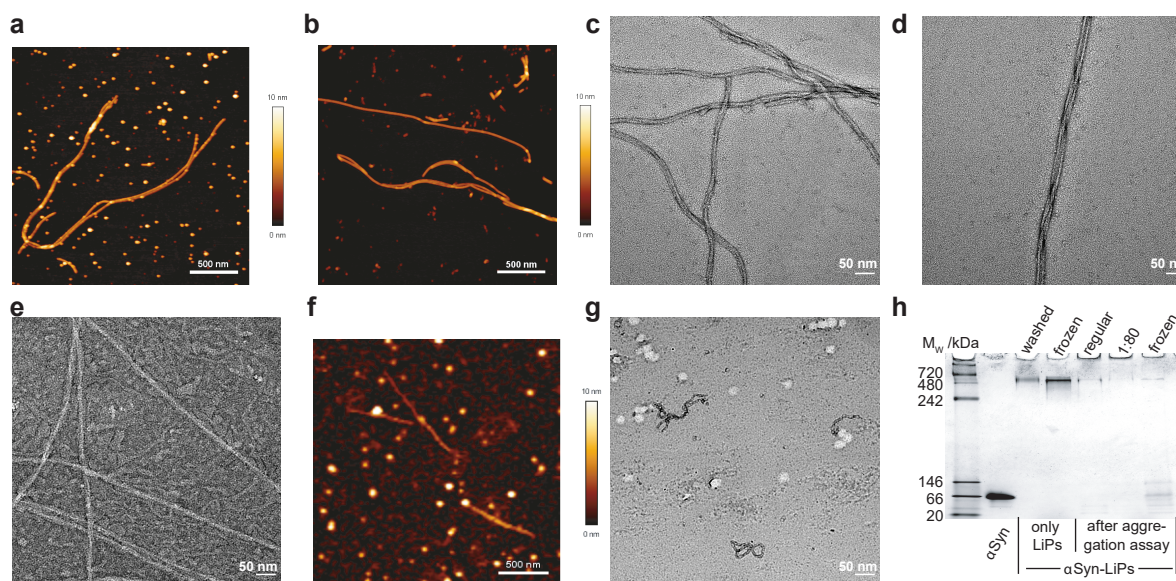


Figure 5.5: Sample properties at the end of the aggregation assays. AFM images of α Syn fibrils grown in the presence of POPG α Syn-LiPs, before centrifugation a) and after removal of the supernatant b). c+d) EM image of α Syn fibrils grown in the presence of POPG α Syn-LiPs before centrifugation (condition 64x in Fig. 5.4c). e) EM image of α Syn fibrillar structures grown in the presence of POPG α Syn-LiPs that did not lead to sizable ThT signal increase (condition 4x in Fig. 5.4c). f+g) AFM and EM image of POPG α Syn-LiPs control samples at the end of the aggregation assays (without addition of excess of monomeric α Syn, Fig. 5.4b). d) Native PAGE of monomeric α Syn as well as α Syn-LiPs in indicated conditions (washed refers to high-salt washed; frozen = non-washed, flash-frozen and stored at -20°C ; regular = non-washed, non-frozen; 1:80 = preparation with high salt and adapted molar ratio of α Syn to lipids of 1:80). Note that amount of monomers added in aggregation assays is identical to amount loaded in the free α Syn control (first lane).

which the α Syn-LiPs induced fibril formation (Fig. 5.4c, 128x for AFM, 64x for EM). α Syn fibrils grown in the presence of SUVs show a clearly distinct morphology when the plateau of ThT fluorescence is reached, since their growth is strongly affected due to the SUV lipids [195]. These SUV-induced fibrils appear to be kinetically trapped, as it was recently found that an increase in temperature is able to induce their conversion into mature fibrils [199]. Interestingly, when directly imaging the sample containing α Syn fibrils that were induced by α Syn-LiPs after the aggregation assay, a number of particles consistent in size and overall appearance with α Syn-LiPs are found (Fig. 5.5a). After centrifugation and removal of the supernatant the occurrence of these particles in the AFM image is largely reduced (Fig. 5.5b). While other contributions, such as drying-induced assemblies of monomeric α Syn cannot be fully excluded, this observation is in line with the presence of soluble α Syn-LiPs after the aggregation assay. EM images also show disc-like particles attached to mature fibrils (Fig. 5.5c). This could either be residual fibril α Syn-LiPs complexes as observed at the beginning of the aggregation assays (Fig. 5.3e,f) or again drying-induced clustering of mature fibrils and soluble α Syn-LiPs or amorphous aggregates. In any case, most fibrils are free of disc-like particles and show characteristic features (branching and twists) of mature α Syn amyloid fibrils (Fig. 5.5c,d).

Surprisingly, EM images of α Syn monomers incubated with the highest amount of POPG α Syn-LiPs (Fig. 5.4c) also show clear fibrillar structures (Fig. 5.5e), despite showing no in-

crease in ThT signal (Fig. 5.4c). As compared to the EM data of the other conditions, this sample displays larger heterogeneity (areas with and areas without fibrillar structures, not shown). In addition, the EM image suggests that the fibrillar structures are surrounded by a rather large number of heterogenous particles, possibly LiPs (Fig. 5.5e). It is at this point not clear whether the total amount of fibrils in this sample is too low to induce a detectable ThT signal increase, or whether the fibrillar structures are lipid (bilayer) tubes, or whether a different fibril morphology and/or lipid coating weakens ThT interactions.

The AFM and EM images of the α Syn-LiPs control sample at the end of the aggregation assays (i.e. α Syn-LiPs without addition of α Syn monomers) still show particles most likely reflecting intact α Syn-LiPs (Fig. 5.5f,g) and low amounts of short fibrillar structures as already present at the beginning of the assay (Fig. 5.3).

To detect remaining monomeric α Syn as well as intact α Syn-LiPs, we additionally carried out a native PAGE analysis of selected samples after the aggregation assays. The resulting gel shows clear bands for the monomeric α Syn reference as well as for freshly prepared α Syn-LiPs (Fig. 5.5h). The latter appears between the molecular weight markers for 480–720 kDa. A comparable band is also observed for frozen α Syn-LiPs. Notably, also weak bands at this position are observed after the aggregation assay, supporting the view that a fraction of α Syn-LiPs are still intact at the end points of the aggregation assay. A rough estimation based on the band intensity and the loaded α Syn-LiPs amount, however suggests that the fraction of intact α Syn-LiPs is rather low (< 10%). Interestingly, the amount of monomeric α Syn loaded onto the gel for the reference sample (first lane) reflects the amount added at the beginning of the respective aggregation assay. Since no or only very weak bands are observed for monomeric α Syn after the aggregation assay, our data show that most monomeric α Syn molecules have either been incorporated into α Syn-LiPs and/or have formed larger aggregates. The rather weak bands for α Syn-LiPs are in favor for the latter, suggesting that α Syn aggregation was very effective in the presence of α Syn-LiPs.

5.6 Conclusion

Overall, we have shown that α Syn-LiPs can be used to induce, accelerate or inhibit α Syn amyloid fibril formation. While our results are well consistent with a planar lipid bilayer stabilized by surrounding α Syn molecules with an approx. 4-to-8-fold increased surface area as compared to MSP1D1 nanodiscs, it should be pointed out that we cannot exclude different molecular arrangements of α Syn and lipids. In addition, we have shown that usage of anionic lipids in combination with low ionic strength of the sample buffer leads to α Syn-LiPs formed with a higher number of α Syn molecules per LiP. Since about half of the α Syn proteins can be detached from these α Syn-LiPs by increasing the ionic strength of the buffer while the other half remains attached to LiPs, we attribute this observation to the contribution of an electrostatically driven binding of α Syn to the negatively charged membrane surface.

5 Interaction of α -Synuclein with α -Synuclein-derived lipoparticles

The presence of α Syn-LiPs in the used aggregation assays evidently induces distinguishable modulations of the aggregation behavior. Our EM data show connections between short fibrillar structures and α Syn-LiPs that could reflect on early lipid induced nucleation events. However, more thorough investigations will be needed to understand the formation and role of these fibril-LiP complexes and whether they play a role in the amyloid fibril formation process. While very consistently only the presence of α Syn-LiPs with anionic lipids led to ThT detectable α Syn fibrils in quiescence aggregation assays, we also observed limitations in well-to-well reproducibility. In general, reproducibility is a common problem in α Syn aggregation assays and it is at this point not clear whether α Syn-LiPs are prone to induce variations in the aggregation assays or whether assay conditions can be further optimized to increase reproducibility. Nevertheless, our data clearly demonstrate that α Syn-LiPs display useful features including (i) a very strong capability to induce primary nucleation, (ii) the possibility to store frozen α Syn-LiP stock solutions, simplifying handling and minimizing artifacts by batch-to-batch variations, and (iii) a not detectable influence on the morphology of fibrils that have formed and grown in the presence α Syn-LiPs. We therefore anticipate that α Syn-LiPs offer an attractive tool, complimentary to other setups, to study various processes of α Syn amyloid fibril formation.

6 Interaction of ARNO-Sec7 with juxtamembrane segment of EGFR

This chapter reflects content of the following publication.

6.1 Publication Information

Title: Molecular Architecture of a Network of Potential Intracellular EGFR modulators: ARNO, CaM, Phospholipids, and the Juxtamembrane Segment

Authors: Aldino Viegas, Dongsheng M. Yin, Jan Borggräfe, Thibault Viennet, Marcel Falke, Anton Schmitz, Michael Famulok, Manuel Etzkorn

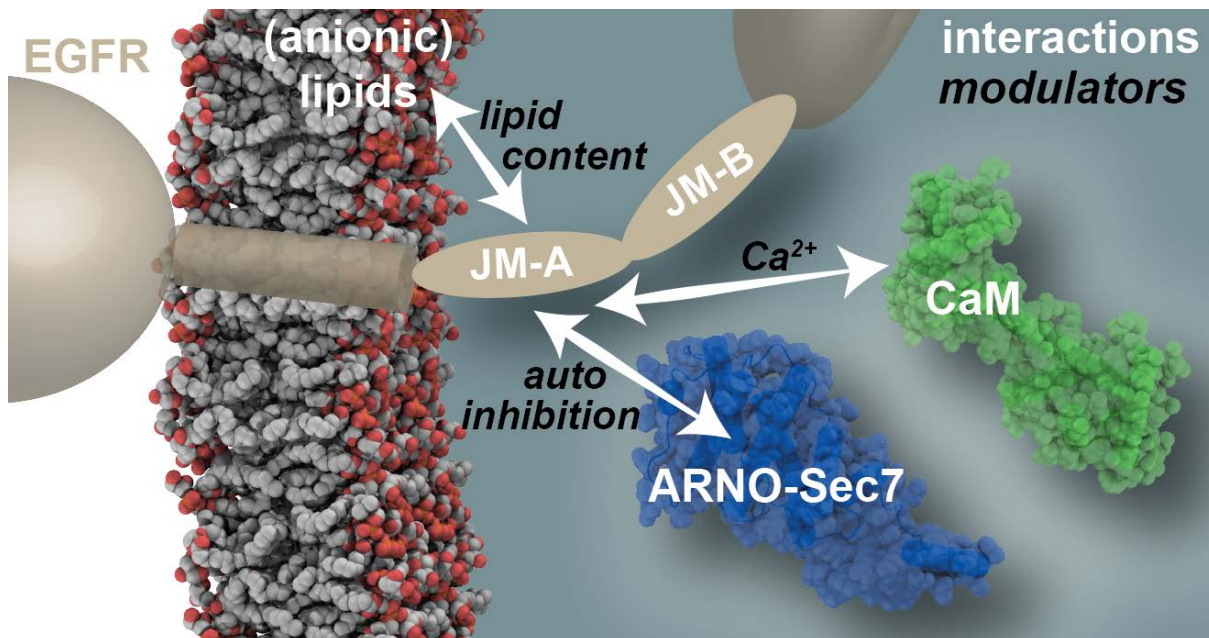
Published in: **Structure**, Vol. 28, pp. 54-62, 2020

DOI: 10.1016/j.str.2019.11.001

6.2 Abstract

Epidermal growth factor receptors (EGFRs) are central cellular signaling interfaces whose misregulation is related to several severe diseases. Although ligand binding to the extracellular domain is the most obvious regulatory element, also intracellular factors can act as modulators of EGFR activity. The juxtamembrane (JM) segment seems to be the receptor's key interaction interface of these cytoplasmic factors. However, only a limited number of cytoplasmic EGFR modulators are known and a comprehensive understanding of their mode of action is lacking. Here, we report ARNO, a member of the cytohesin family, as another JM-binding protein and structurally characterize the ARNO-EGFR interaction interface. We reveal that its binding mode displays common features and distinct differences with JM's interaction with calmodulin and anionic phospholipids. Furthermore, we show that each interaction can be modulated by additional factors, generating a distinctly regulated network of possible EGFR modulators acting on the intracellular domain of the receptor.

Graphical Abstract



6.3 Introduction

The epidermal growth factor receptor (EGFR) is a major regulator of proliferation in epithelial cells. Since its misregulated activation can lead to hyperproliferation and the development of cancer, an intricate regulatory network to control EGFR activity has evolved comprising systemic and cell-autonomous elements [208]. Key to the regulation of EGFR activity is the receptor's intrinsic autoinhibition, on which the regulatory network is built. The importance of this autoinhibition is evident from several mutations which disrupt the autoinhibition and are linked to specific types of cancer [209]. In general, the autoinhibited state can be released by formation of an asymmetric EGFR dimer in which one kinase domain activates the other one [160]. This asymmetric dimer is stabilized by the juxtamembrane (JM) segments of both intracellular domains of the involved monomers. The C-terminal part of the JM segment of the activated kinase functions as a 'latch' or 'cradle' for the activator kinase [91,210]. In addition, the N-terminal parts of both JM segments are thought to form an antiparallel coiled-coil enhancing the affinity of the monomers for each other [210]. The formation of the antiparallel coiled-coil requires the C-termini of the transmembrane helices to be separated from each other which on its turn is coupled to the ligand-bound conformation of the extracellular domain and thus confers regulation by EGF. In the inactive state, the basic JM segment binds to acidic phospholipids of the inner leaflet of the plasma membrane, and this interaction contributes to the autoinhibition of the receptor [211].

In addition to its function in relaying the conformational changes induced by EGF-binding from the extracellular domains to the kinase domains, the JM segment is a site of modulation of EGFR activity by intracellular factors. Previous studies identified a number of hot spots associated e.g. with kinase interaction (T654 and T669) [89, 90], activation of the receptor (V665 and L680) [91] or a possible conformational constraining of the receptor (R645 – R657) [92]. When e.g. threonine-654 in the JM segment is phosphorylated by protein kinase C the activity of the EGFR is attenuated [89, 212–214] probably due to inhibition of EGFR dimerization [215]. Phosphorylation of another threonine (T669) in the JM segment by extracellular signal-regulated kinase (ERK) reduces EGFR downregulation [216]. Recently the tumor necrosis factor receptor associated factor 4 (TRAF4) has been reported to interact with the C-terminal part of EGFR-JM to promote receptor dimerization [217]. The cytosolic protein calmodulin (CaM) binds to the N-terminal part of the JM segment in a calcium-dependent manner [93, 94] enhancing EGFR activation [95, 96].

In this work we report on the ability of ARNO (ADP ribosylation factor nucleotide binding-site opener), a member of the cytohesin family of guanine nucleotide exchange factors, to bind EGFR's JM domain. While ARNO has been proposed to function as activator of the EGFR [218–220], the underlying mechanism has not been determined. Here, we provide a comprehensive *in vitro* analysis of the determinants that define the ARNO-JM interaction and characterize the interaction at the molecular level in the absence and presence of a membrane environment. We identify the JM-binding site in the Sec7 domain of ARNO and show that JM's interaction with ARNO-Sec7 displays large similarities to its interaction with CaM, pointing to the speculation that ARNO and CaM may modulate EGFR in a similar manner. Our data also reveal that ARNO-Sec7, CaM as well as lipid bilayers containing anionic phospholipids compete for overlapping binding sites on the JM segment. Moreover, we show that additional factors including auto inhibition for ARNO, Ca^{2+} availability for CaM and lipid composition for JM's membrane association, are capable to further regulate this competitive network of EGFR-JM interaction partners. While we here focus on the structural and biophysical characterization of this network under defined *in vitro* conditions, our findings are consistent with previous findings in living cells and in tumor tissue [218–220] and should stimulate future studies of this important aspects in EGFR signaling.

6.4 Results and Discussion

The JM segment of the EGFR interacts with the Sec7 domain of ARNO

To investigate whether ARNO interacts with the EGFR we carried out microscale thermophoresis (MST) measurements of selected isolated domains. Since ARNO is a cytosolic protein, only EGFR constructs comprising the intracellular domain were considered (Fig. 6.1a). Our MST data show that the EGFR intracellular domain (ICD) indeed interacts with the Sec7 domain of ARNO (Sec7) (Fig. 6.1b, black). The other major domain of ARNO, the pleckstrin homology domain (PH), did not show binding under the applied conditions (data not shown).

6 Interaction of ARNO-Sec7 with juxtamembrane segment of EGFR

Interestingly the purified juxtamembrane segment (JM) alone displays a comparable binding behavior to ARNO-Sec7 as EGFR-ICD (Fig. 6.1b, blue). While EGFR-ICD and EGFR-JM bind ARNO-Sec7 with similar affinity (K_D of about $50 \mu\text{M}$), an EGFR-ICD construct lacking the first 27 amino acids of the JM segment (EGFR-ICD ΔJM_{1-27}) does not show interaction (Fig. 6.1c, grey), which is also true for a scrambled version of JM (JM_{sc}) containing the same amino-acids, but randomly redistributed (Fig. 6.1c, pink, see Methods for full sequence). Our data demonstrate that ARNO-Sec7 interacts with the EGFR *in vitro* and strongly suggest that this interaction is on the EGFR side mainly driven by the JM segment.

Due to JM's key role in EGFR regulation [91, 92, 210, 215, 221, 222] and its high potential for EGFR signaling modulation [93], we carried out a comprehensive NMR study to characterize the molecular architecture of the interaction of ARNO-Sec7 and EGFR-JM.

Following the full resonance assignments of both domains (see supplementary Tables 6.1 and 6.2 and Fig. 6.13 for details on data acquisition, resonance assignment and structural features) we performed NMR-based titration studies with Sec7 and JM to identify the interacting regions based on the chemical shift perturbations (CSP) induced by their binding partner. Figure 6.1d-g summarize the data from the point of view of the (^{15}N -isotope-labeled) JM segment. The presence of increasing amounts of (unlabeled) Sec7 induces characteristic concentration-dependent chemical shift perturbations for certain residues (Fig. 6.1d). Plotting these chemical shift perturbations along the JM sequence clearly identifies the N-terminal half of JM, i.e. the JM-A segment [210], as the one involved in the interaction with Sec7. Furthermore, the NMR chemical shifts continuously

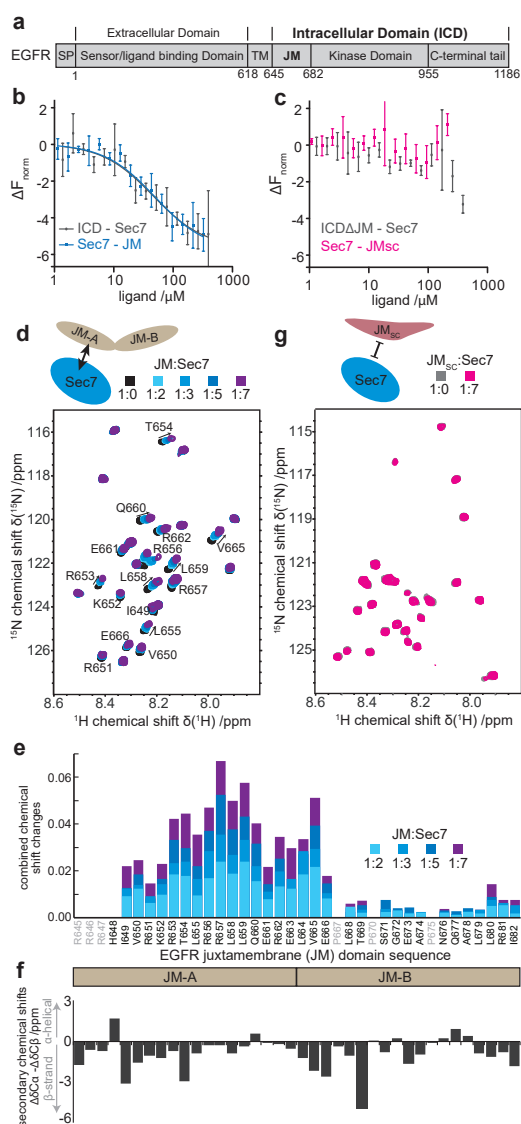


Figure 6.1: JM-Sec7 interaction as seen from the EGFR-JM side. a) Schematic representation of EGFR's domain architecture (SP: signal peptide; TM: transmembrane domain; JM: juxtamembrane). b+c) MST data for indicated EGFR and ARNO constructs. Here and in the subsequent figures the EGFR construct is always mentioned first and the fluorophore-labeled molecule is labeled with asterisk ($n=3$, mean \pm SD). d) [^1H ; ^{15}N]-HSQC NMR spectra of ^{15}N -labeled EGFR-JM in the presence of increasing amounts of unlabeled ARNO-Sec7. e) Chemical shift perturbations along the EGFR-JM sequence induced by the presence of indicated amounts of ARNO-Sec7. Grey labels indicate residues that were not observed. f) Secondary chemical shifts (see Supplementary Information for definition) as indicator for secondary structure of EGFR-JM when free in solution. g) [^1H ; ^{15}N]-HSQC NMR spectra of a ^{15}N -labeled scrambled version of EGFR-JM (JM_{sc}) in the absence (grey) or presence of 7-fold excess (magenta) of ARNO-Sec7.

change with increasing concentration of Sec7, revealing a rather transient interaction (NMR fast-exchange regime) with residue specific binding affinities (K_D) in the high μM range (see Supporting information Figure 6.13e for more details).

In general, NMR chemical shifts, in particular of carbon C_α and C_β nuclei, are robust indicators of secondary structure [223]. Analysis of the respective chemical shifts of the isolated JM segment points to the absence of a clear secondary structure when free in solution (Fig. 6.1f). This observation is in good agreement with previous results [224, 225], in which JM was shown to behave mainly as random coil in the absence of membrane mimetics.

Addition of Sec7 did not lead to detectable ^{13}C chemical shift perturbations (data not shown), which suggests that the interaction with Sec7 does not induce a stable secondary structure in JM. However, the rather uniform shift of the affected peaks in the $^1\text{H}, ^{15}\text{N}$ -HSQC spectrum (Fig. 6.1d) towards lower ^1H and ^{15}N frequencies would be in line with an increase in transient α -helical propensity upon Sec7 binding [223]. The JM segment of EGFR contains a high number of charged residues (see Fig. 6.13c). In particular the JM-A segment comprises an unusually high number of positively charged residues (i.e. 10 out of 20 residues). To test whether the interaction with Sec7, which contains both negatively and positively charged regions (Fig. 6.14), is driven by nonspecific electrostatic interactions we used again the scrambled JM construct (JM_{SC}) containing the same total amino acid composition but randomly redistributed. In line with the MST measurements (Fig. 6.1c, pink), the NMR measurement (using ^{15}N -labeled JM_{SC} , Fig. 6.1g) shows that the scrambled JM does not interact with Sec7, in clear contrast to wild-type JM under identical conditions (e.g. Fig. 6.1d, purple). Our data therefore demonstrate that the absolute charge of JM is not key to the interaction and imply that the primary sequence of JM promotes a specific recognition by Sec7.

Due to its good NMR properties [226] ARNO-Sec7 offers the appealing opportunity to investigate the interaction also from the cytohesin point of view. Consequently, we recorded a series of NMR experiments using ^{15}N -isotope labeled ARNO-Sec7 and non-labeled EGFR-JM (Fig. 6.2). In line with the data obtained from the JM point of view (Fig. 6.1), the presence of increasing amounts of EGFR-JM induced chemical shift perturbation for specific Sec7 residues (Fig. 6.2b,c) reproducing the transient interaction of the two domains (NMR fast exchange regime) and pinpointing a specific JM-binding site of Sec7. Following the resonance assignment of the 21 kDa Sec7 construct (Fig. 6.13, BMRB deposition code: 27761) distinct regions of the Sec7 domain can be identified that interact with the isolated JM segment (Fig. 6.2d). The affected residues mainly cluster around helices E (5), F (6), G (7), H (8) and I (9) and the loop connecting helices I (9) and J (10) (helix nomenclature as in [227] and, in brackets, according to [226]). Highlighting the most affected residues in the Sec7 structure reveals a well-defined JM-binding interface (Fig. 6.2e).

While the affected region partially overlaps with the negatively charged surface of Sec7 (see Fig. 6.14), it also involves a high number of hydrophobic residues (17 out of 39), suggesting that ARNO-Sec7 interacts with EGFR-JM, in part, through an extended hydrophobic surface. In particular, a surface-exposed hydrophobic patch of residues in Sec7's helix H appears to be in the center of this interaction. Reducing the hydrophobicity of this patch by alanine substi-

6 Interaction of ARNO-Sec7 with juxtamembrane segment of EGFR

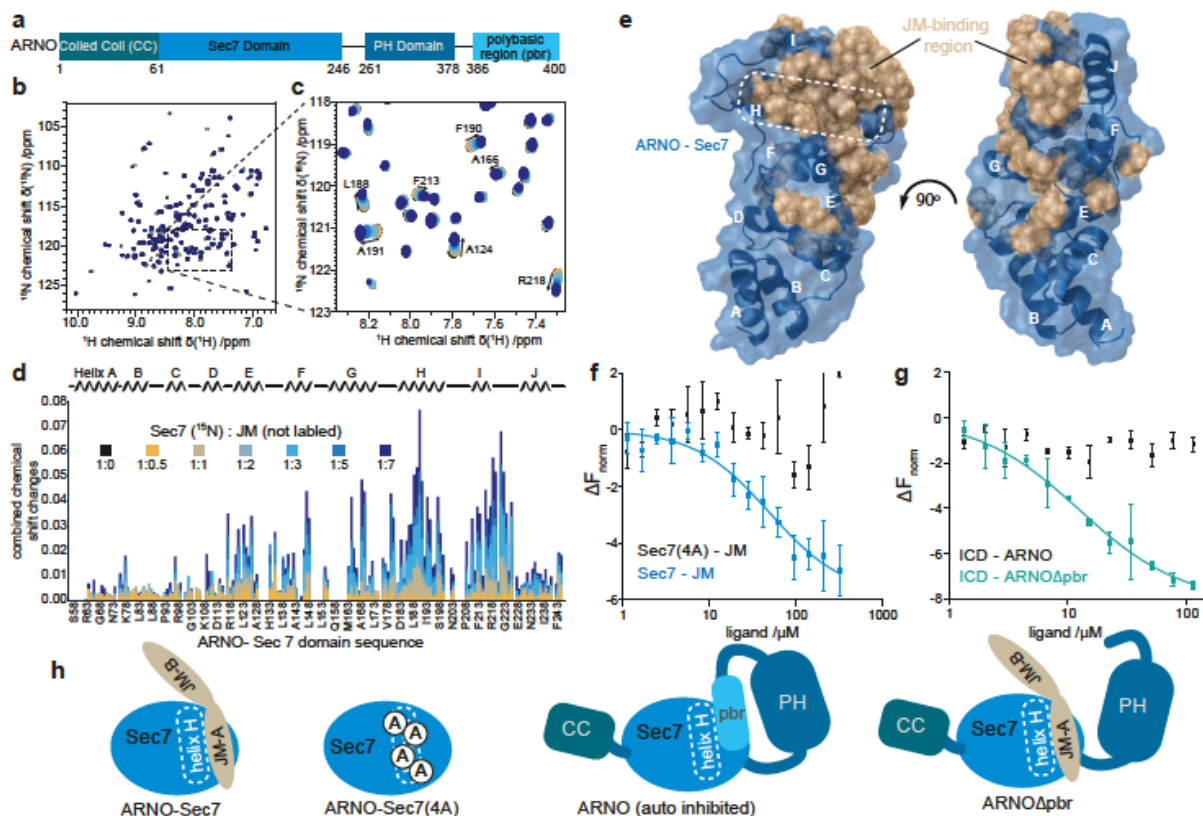


Figure 6.2: JM-Sec7 interaction as seen from the ARNO-Sec7 side. a) Schematic representation of ARNO's domain architecture. b+c) $^1\text{H};^{15}\text{N}$ -HSQC NMR spectra of ^{15}N -labeled ARNO-Sec7 in the presence of increasing amounts of unlabeled EGFR-JM (color code as in d). d) Chemical shift perturbations along the ARNO-Sec7 sequence induced by the presence of indicated molar ratios of EGFR-JM. e) Mapping of most affected residues on the 3D structure of ARNO-Sec7 (pdb code: 4JMI [228]) indicating the EGFR-JM binding side of ARNO-Sec7. f+g) MST data showing disruption of JM's interaction with ARNO-Sec7 due to mutations (f) or autoinhibition (g). f) Alanine substitutions of surface-exposed hydrophobic residues of helix H of Sec7, i.e. Sec7(4A), lead to disruption of the interaction with JM. The JM-Sec7 data (blue) is identical to data shown in Fig. 6.1b and serves as reference. g) While the presence of the autoinhibitory polybasic region (pbr) in full-length ARNO inhibits interaction with EGFR-ICD (black), deletion of the polybasic region (ARNO Δ pbr) restores the interaction (n=3, mean \pm SD). h) schematic summary of MST and NMR results.

tutions of Y186, F190, I193 and M194, i.e. ARNO-Sec7(4A), indeed inhibits binding to JM as determined by MST (Fig. 6.2f).

Of note, the observed binding site is also located in a region populated by residues crucial for the interaction of Sec7 with ARF1 [226, 227, 229]. ARF1 binding is prevented in the autoinhibited state in all cytohesin members when helix H forms intramolecular contacts with the linker and the polybasic region (pbr). Accordingly, ARNO lacking the polybasic region (ARNO Δ pbr) loses this autoinhibition [230]. To test whether this autoinhibitory mechanism also plays a role for an interaction of ARNO with the EGFR, we carried out MST measurements using EGFR-ICD and either full-length ARNO or ARNO Δ pbr (Fig. 6.2g,h). Indeed, full length (autoinhibited) ARNO did not bind EGFR-ICD (Fig. 6.2g, black) whereas for ARNO Δ pbr the interaction was restored (Fig. 6.2g, green). This data supports the importance of Sec7's helix H in the interac-

tion and suggests that ARNO's autoinhibitory mechanism may also regulate its interaction with the EGFR.

EGFR-JM's interaction with membranes shares common features and distinct differences to ARNO-Sec7

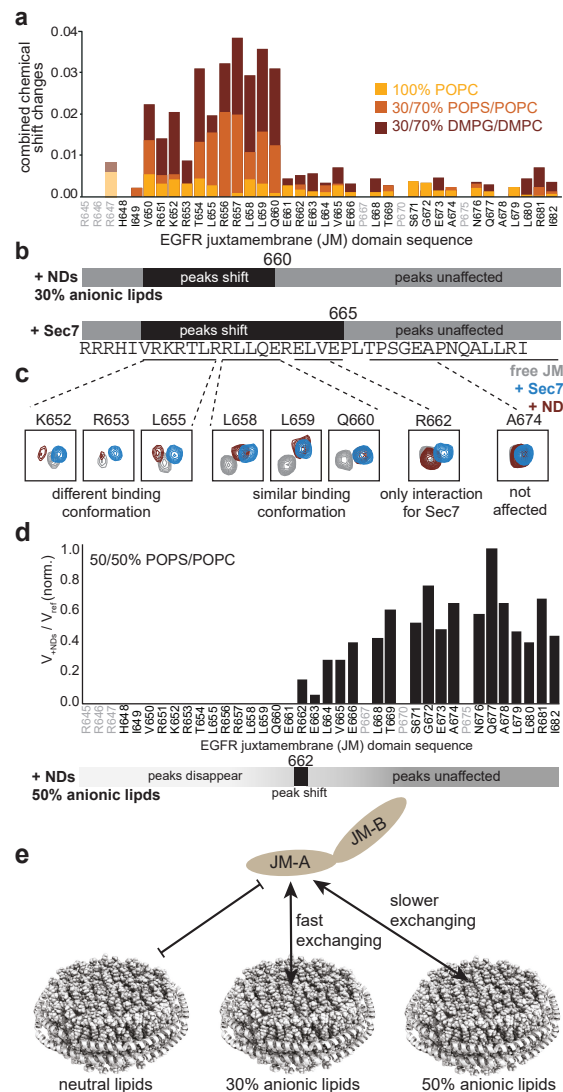
We have shown that ARNO-Sec7 binds the JM segment of the EGFR. As it is known that the JM segment also interacts with CaM and anionic phospholipids of the inner leaflet of the plasma membrane [93, 211, 231–234] we subsequently investigated similarities and/or differences in the binding mode of these interactors. To obtain the desired high-resolution information into the effect of the membrane surface, the interactions of JM with phospholipids in the form of phospholipid-bilayer nanodiscs (NDs) were characterized by NMR spectroscopy.

Our data show that the presence of NDs containing only the neutral POPC phospholipid does not induce noticeable chemical shift perturbations in EGFR-JM (Fig. 6.3a, yellow), indicating that this domain on its own does neither interact with neutral phospholipids nor with the membrane scaffold proteins (MSP) used to assemble the NDs. While the latter corroborates usage of MSP-derived nanodiscs as suitable membrane mimetic for the system, the absence of interactions with POPC lipids differs to previous findings in which a strong interaction of JM to DPC micelles was observed [224]. Since DPC detergent molecules and POPC lipids both comprise the same phosphocholine head group, our results suggest that the overall assembly of the membrane mimetic (detergent-free lipid bilayers vs. detergent monomer-micelle equilibrium) has a strong influence on the interaction with JM. At this point it can only be speculated that the nanodiscs better reflect the physiologically-relevant membrane interaction of JM. However, in any case, the observed difference between detergent micelles and nanodiscs highlights the importance of the choice of a suitable membrane mimetic for structural studies of membrane interactions.

The strengths of the nanodisc system include its homogeneity, stability, the absence of detergents and near native bilayer arrangement as well as a the possibility to accurately change their lipid composition without modifying other parameters and use NMR-spectroscopy to determine lipid specific interaction with single amino acid resolution [83, 235]. In the following we made use of these features to investigate the interaction of JM with NDs containing 30% anionic phospholipids via NMR spectroscopy. Two different phospholipid mixtures were used, i.e. 30% anionic DMPG lipids with 70% neutral DMPC lipids as well as anionic POPS lipids (30%) with neutral POPC lipids (70%). In both cases clear changes in the NMR spectrum induced by the presence of the respective nanodiscs can be observed (Fig. 6.3a, Fig. 6.15 and Fig. 6.16). Similar to the interaction with ARNO-Sec7, the residues affected the most by the presence of the anionic membrane surface are confined to the JM-A region. However, a closer look also reveals that the phospholipid interacting region is a few residues shorter than the Sec7-binding region.

A comparison of EGFR-JM's interaction with anionic lipids or ARNO-Sec7 highlights four different sections in JM (Fig. 6.3b,c). While residues V650-Q660 show considerable chemical-

Figure 6.3: JM-membrane interaction depends on anionic lipid content and follows a similar pattern as Sec7 binding with distinct differences. a) Chemical shift perturbations along the EGFR-JM sequence induced by the presence of nanodiscs with the indicated lipid composition. b) Schematic comparison of EGFR-JM binding behavior to lipid bilayers containing 30% anionic lipids (upper chart) or ARNO-Sec7 (lower chart, according to data shown in Fig. 6.1e). c) NMR signals of selected residues representative of JM regions with different behavior induced by the presence of Sec7 (blue peaks, also see Fig. 6.1) or NDs with 30% anionic lipids (red peaks). Blue area highlights residues showing interaction exclusively with Sec7 and not the used NDs. d) Effects of addition of NDs with 50% anionic lipid content. Unlike to the peak shifts visible for ND interaction with 30% anionic lipid content (a) or Sec7 binding (Fig. 6.1), addition of NDs containing 50% POPS and 50% POPC (brown) or 50% DMPG and 50% DMPC (dark brown) predominantly leads to disappearance of peaks for residues in JM-A (see Fig. 6.15 and Fig. 6.16 for comparison of spectra, peak shifts and volumes for all used lipid mixtures). The observed peak disappearance is indicative of prolonged contact times of this region with the lipids (i.e. NMR medium or slow exchange regime for 50% anionic lipids and NMR fast exchange regime for 30% anionic lipids or Sec7). e) Schematic summary of EGFR-JM's interaction with different NDs. In a) and d), grey labels indicate residues that were not observed.



shift perturbations induced by both interaction partners, the first half of these residues (V650-L655, Fig. 6.3c, section #1) show clearly different chemical shifts upon binding to lipids or Sec7, whereas the second half (R656-Q660, Fig. 6.3c, section #2) experience an almost identical variation in chemical shift. The third section (R662-V665, Fig. 6.3c, section #3) is only affected by Sec7 and not by the lipids. The fourth section (L667-I682, Fig. 6.3c, section #4) is not affected by the presence of either interaction partner. Consequently, EGFR-JM's interaction with anionic phospholipids shares some common features with the interaction with ARNO-Sec7, but also displays distinct differences.

A comparative summary of EGFR-JM's interaction with anionic lipids or with ARNO-Sec7 highlights four different sections in JM (Fig. 6.3b,c). While residues V650-Q660 show considerable chemical-shift perturbations induced by both interaction partners, the first half of these residues (V650-L655, section 1, Fig. 6.3c) show clearly different chemical shifts upon binding to lipids or Sec7, whereas the second half (R656-Q660, section 2, Fig. 6.3c) experience an almost identical variation in chemical shift.

While the presence of NDs with 30% content of anionic phospholipids leads to chemical shift perturbations indicative of fast exchange processes, increasing the membrane charge density to 50% anionic phospholipids alters the interaction kinetics and leads to considerable peak broadening indicative of intermediate exchange processes (see supplementary Fig. 6.16 for experimental data). Considering the size of the ND system a tight binding (in the slow exchange regime) could also explain this observation. In any case, it can be assumed that the JM-membrane interaction becomes stronger with increased negative charge density of the membrane. When plotting the peak intensity instead of the chemical shift changes it can be seen that also under these conditions the JM-A region is the driving force of the interaction (Fig. 6.3d).

Overall our data shows that despite JM-A being mainly involved in the interaction with lipids and Sec7, the interaction with Sec7 occurs over an extended binding mode that involves a number of additional JM residues, as compared to JM's interaction with the membrane surface. In addition, an increase of the anionic lipid content from 30% to 50% slows down the otherwise fast bound-to-free exchange processes, revealing the possibility of modulating JM's membrane interaction kinetics by variations in lipid composition.

The interplay of lipids, CaM and Sec7 as intracellular modulators of EGFR-JM

To directly compare the observed interaction of EGFR-JM with ARNO-Sec7 to the known cytoplasmic EGFR modulator CaM, we carried out additional MST and NMR-based experiments. Unsurprisingly, our MST data shows that binding of CaM to EGFR-ICD is calcium- and JM-dependent (Fig. 6.4a). When recording NMR spectra of EGFR-JM in the presence of unlabeled CaM, a set of peaks disappear from the spectrum (in line with an interaction in the NMR intermediate exchange regime).

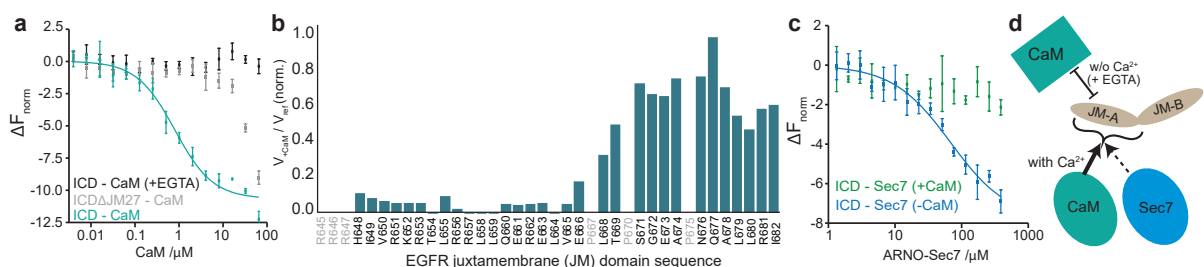


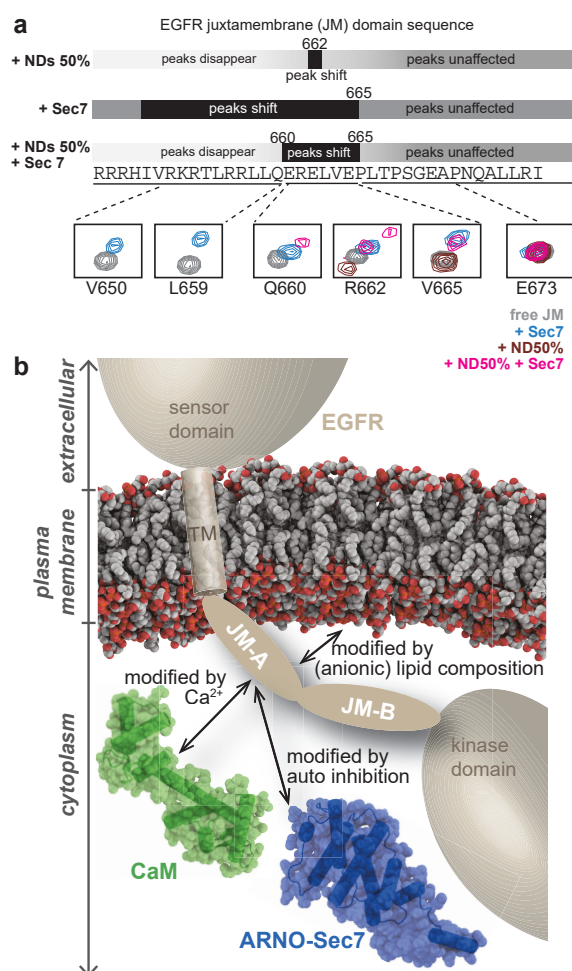
Figure 6.4: Calmodulin (CaM) and ARNO-Sec7 share same binding site and compete for EGFR-JM binding *in vitro*. a) MST data of the interaction of CaM and EGFR-ICD. Removal of accessible calcium via EGTA (black) as well as deletion of the first 27 residues of the JM segment (grey) largely reduces the binding of calcium-activated CaM to EGFR-ICD (green; $n=3$, mean \pm SD). b) Changes in EGFR-JM residue specific peak volumes upon addition of CaM. Peak disappearance reports on interaction between the effected JM residues and CaM (NMR intermediate exchange regime) Grey labels indicate residues that were not observed. c) MST data of the interaction between ARNO-Sec7 and EGFR-ICD in the absence (blue) or presence of $30\ \mu\text{M}$ CaM (green; $n=3$, mean \pm SD). d) Schematic comparison of the observed CaM and Sec7 binding behavior of EGFR-JM.

6 Interaction of ARNO-Sec7 with juxtamembrane segment of EGFR

As expected [93,236], plotting the decrease in intensity along the JM sequence again reveals that predominantly JM-A interacts with CaM (Fig. 6.4b). Looking at the affected JM residues it can be seen that the CaM binding region of JM is again a few residues longer than its membrane binding region. Interestingly the CaM and the Sec7 binding regions of JM are essentially identical. However, in line with a higher binding affinity seen in the MST data (K_D of about 1 μM), the NMR data also suggest that CaM interacts less transiently with JM as compared to Sec7 or membranes with 30% negative charge content.

Figure 6.5: The interplay between possible modulators acting on EGFR-JM as central interface in the intracellular interaction network of the EGFR.

a) Comparison of NMR results for EGFR-JM in the presence of NDs with 50% anionic lipids (POPS, top), or in the presence of ARNO-Sec7 (middle), or in the presence of both interaction partners (lower schematic). Overlay of residue specific NMR signals in the absence (grey) or presence of indicated interaction partner(s). Selected residues, representative of the three differently affected regions, are shown. b) Schematic summary of EGFR-JM interaction partners, shown in this study to interact with the JM-A segment *in vitro*, and their individual modulators.



Having found that CaM and ARNO-Sec7 bind to an essentially identical binding site on EGFR-JM we investigated a possible competition of CaM and ARNO-Sec7 for binding to the EGFR using MST. In line with the higher binding affinity of CaM, when EGFR-ICD (200 nM) was preincubated with a saturating concentration of CaM (30 μM), the binding of ARNO-Sec7 was completely prevented (Fig. 6.4c), confirming a competitive binding of CaM and ARNO-Sec7 *in vitro*.

Our data shows that CaM and ARNO-Sec7 interact with the same JM region. This fact hinders a reliable NMR investigation of the competition between these two proteins. In contrast, the binding regions of JM to phospholipid nanodiscs or Sec7 sufficiently differ to allow distinction between the binary JM-nanodisc and JM-Sec7 complexes. In particular, residues (E661-V665) in the center of the JM segment can be used as reporters since they are not affected by binding to phospholipids but are part of the Sec7-interacting region (Figs. 6.3 and 6.16). Indeed, when adding unlabeled ARNO-Sec7 to the JM peptide preincubated with NDs containing high amounts of anionic lipids (50/50% POPC/POPS) distinct chemical shift perturbations are visible for the 'Sec7-specific-reporter residues' E661-V665 as compared to free JM or to JM in the presence of just NDs (Fig. 6.5a and Fig. 6.17). The observed peak shift is consistent with the perturbations expected due to formation of a JM-Sec7 complex. Interestingly, JM residues directly at the edge of the membrane binding interface (Q660 and R662) show stronger or different chemical shift perturbation when both binding partners are present (as compared to the individual pairwise interactions, Fig. 6.5a). This behavior is indicative of cooperative effects and/or different structural alterations. While our data does not allow to distinguish between a ternary JM-membrane-Sec7 complex or an exchanging 3-state equilibrium (free JM, membrane-bound JM, Sec7-bound JM), the NMR data show that ARNO-Sec7 can interact with the JM peptide even in the presence of NDs containing a high amount of anionic lipids and thus support the notion that ARNO can interact with the EGFR at the plasma membrane.

6.5 Conclusion

Using solution NMR spectroscopy and microscale thermophoresis (MST), supported by site-directed mutagenesis techniques, we show that ARNO-Sec7 and EGFR-JM interact *in vitro*. The residues of both Sec7 and JM involved in binding were identified (Figs. 6.1 and 6.2). From the JM side, NMR data showed that Sec7 specifically recognizes the first half of the segment (i.e. JM-A, Fig. 6.1e), which has been shown to be of importance for EGFR activation [92, 210, 215, 221, 222]. JM-A is also the region recognized by calmodulin (Fig. 6.4), a major regulatory protein of the EGFR [93, 95, 234, 236]. Furthermore, JM-A tethers JM to the plasma membrane (Fig. 6.3), stabilizing the inactive conformation of the EGFR [237, 238].

The isolated JM peptide in solution seems to exist mainly as random coil (Fig. 6.1f), with some propensity to form a transient α -helix at the JM-A region [210, 225, 237, 239]. Our data reveals that, upon binding to Sec7, the amide resonances of JM-A shift upfield (Fig. 6.16c), which is indicative of a higher helical propensity in the Sec7-bound conformation. The JM segment also interacts with negatively charged phospholipids of the inner leaflet of the membrane [211, 238]. By using phospholipid nanodiscs (NDs) we demonstrate that JM-A is also the region responsible for binding to membranes containing anionic lipids. While the membrane-binding and Sec7-binding regions of JM largely overlap, a closer analysis of the NMR data shows that some residues experience different chemical shift perturbations upon binding to either partner

and that the binding interface to Sec7 is elongated as compared to the lipid binding interface (Fig. 6.3b and Fig. 6.16).

From the Sec7 side, our data shows that the accessibility of the JM binding site is restricted when ARNO is in the autoinhibited state which is common to all cytohesin members [230] (Fig. 6.2). Release from the autoinhibition requires the binding of an already activated, membrane-attached ARF molecule or of phosphoinositides (PIPs) to the PH domain and maximum activation requires both steps resulting in exposure of the Sec7 domain [240, 241]. As PIPs cluster around the EGFR [96, 231, 232, 242, 243], binding of ARNO to these PIPs would bring it near to the EGFR and simultaneously activate it for JM binding (Fig. 6.17 for schematic visualization). The PIPs-driven co-localization and/or insufficient Ca^{2+} availability could also counteract the higher affinity observed for Ca^{2+} -activated CaM as possible competitor of the ARNO-EGFR interaction. The interplay between ARNO's expression level and state of activation, the plasma membrane's lipid composition and its arrangement, as well as the available Ca^{2+} - and CaM levels could therefore provide a further layer of modulation of EGFR signaling (Fig. 6.5b). Whether binding of ARNO to the JM segment of the EGFR occurs in the living cell and whether this binding would indeed modulate EGFR signaling is however currently unknown. There is indirect evidence for ARNO modulating EGFR activity [218–220] but the mechanism has not been elucidated. Due to our findings that *in vitro* ARNO interacts with the JM segment in a similar way as CaM does, it is tempting to speculate that ARNO and CaM could modulate EGFR activity also by a similar mechanism. Although the mechanism by which CaM modulates EGFR activity has not yet been exactly determined, it appears to involve the weakening of JM's interaction with phospholipids of the membrane [211, 244]. Our data obtained in the presence of phospholipid nanodiscs are consistent with this view and with a model in which CaM and ARNO could contribute to the activation of the EGFR by releasing one of several autoinhibition mechanisms of the EGFR, namely the immobilization of the JM segment on the surface of the membrane.

6.6 Material and Methods

Protein constructs and expression

Human EGFR-ICD (amino acids 645-1186, numbering according to UniProt P00533 without the 24 amino acids of the signal peptide) was equipped with a 6xHis tag and a TEV cleavage site and cloned into pFastBac-1 (Invitrogen) such that after TEV cleavage the protein contained two additional amino acids (Gly, Ala) at the *N*-terminus. EGFR-ICD Δ JM₁₋₂₇ (amino acids 672-1186) was constructed by inserting a TEV cleavage site between amino acids 671 and 672 of EGFR-ICD and cloned into pACEBac-1 (ATG:biosynthetics) such that after TEV cleavage the protein had no additional amino acids. Recombinant baculoviruses were generated using the MultiBacTurbo Expression System (ATG:biosynthetics) and proteins expressed for 3 days in SF9 cells (Invitrogen). EGFR-JM (amino acids 645-682) was fused to maltose binding protein followed by a TEV site such that after TEV cleavage the unmodified JM peptide was obtained.

It was cloned into pET-28a (Novagen) and expressed for 3 h at 37 °C in *E. coli* BL21(DE3) (Stratagene). EGFR-JMSC was obtained by scrambling amino acids 645-682 resulting in the sequence: RELKHIQVRL RTERQLEPLE IRAVNRSRLT PRLAGLPR. Otherwise it was treated the same way. Human ARNO (UniProt Q99418), ARNO Δ pbr (amino acids 1-386), ARNO-Sec7 (amino acids 61-246), ARNO-Sec7(4A) (Y186, F190, I193 and M194 changed to Ala) and human CaM (UniProt P0DP23, amino acids 2-149) were equipped with a 6xHis tag and a TEV cleavage site, cloned into pET-28a and expressed at 20 °C overnight in *E. coli* BL21(DE3). Except for CaM, the constructs contain additional Gly and Ser at the *N-terminus* after TEV cleavage

Protein purification and labelling

All cell pellets were homogenized via French press in lysis buffer (50 mM Tris/HCl, pH 7.8, 300 mM NaCl, 10% glycerol, 25 mM imidazole), except for calmodulin in different lysis buffer (50 mM HEPES/KOH, pH 7.8, 300 mM NaCl, 10% glycerol, 25 mM imidazole). EGFR-ICD, EGFR-ICD Δ JM₁₋₂₇, all ARNO constructs and calmodulin were purified via Ni-NTA affinity chromatography (Macherey-Nagel). Eluted samples were buffer exchanged to remove imidazole, before TEV cleavage overnight at 4 °C. Protein samples were then subjected to reverse Ni-NTA chromatography (Macherey-Nagel), and concentrated using Vivaspin Turbo (Sartorius) followed by size exclusion chromatography either on HiLoad 16/600 Superdex 200pg (GE Healthcare) for EGFR-ICD and EGFR-ICD Δ JM₁₋₂₇, or on HiLoad 16/600 Superdex 75pg (GE Healthcare) for ARNO-Sec7, ARNO-Sec7(4A) and calmodulin. In addition, during TEV cleavage of EGFR-ICD, 0.5 μ M His-tagged YopH and 0.5 mM MgCl₂ was added for dephosphorylation of the kinase. During calmodulin purification, cleared lysate was heated for 5 min at 80 °C, then cooled down on ice for 10 min, followed by centrifugation to remove denatured proteins. Furthermore, 1 mM of CaCl₂ was supplemented to the sample immediately before size exclusion chromatography. MBPT-EGFR-JM and MBPT-EGFR-JMSC were purified via amylose affinity chromatography (New England Biolabs), followed by TEV cleavage at room temperature for 48 h. Afterwards, digested sample was applied to size exclusion chromatography on HiLoad 16/600 Superdex 30pg (GE Healthcare). All the gel filtration runs were monitored at 280 nm, except for EGFR-JM, EGFR-JM_{SC} and calmodulin at 214 nm. All the collected peak samples were concentrated in buffer H (20 mM HEPES/KOH, pH 7.8, 150 mM NaCl), using Vivaspin Turbo (Sartorius).

For the fluorescence labeling of ARNO-Sec7 and ARNO-Sec7(4A), 10 μ M proteins were mixed with 100 μ M Alexa Fluor 647 NHS Ester (Thermo Fisher) in labeling buffer T (20 mM HEPES/KOH, pH 7.8, 150 mM NaCl, 100 mM NaHCO₃). The labeling reactions were carried out on ice in the dark for 1 h. For the labeling of EGFR-ICD and EGFR-ICD Δ JM₁₋₂₇, 10 μ M proteins were mixed with 30 μ M RED-NHS 2nd generation (NanoTemper) in labeling buffer N (20 mM HEPES/KOH, pH 7.8, 150 mM NaCl). The mixture was incubated on ice in darkness for 30 min. All labeling reactions were terminated by addition of 100 mM Tris/HCl, pH 8. Afterwards, samples were applied to pre-equilibrated illustra Nap-5 columns (GE Healthcare) to

remove free dye, followed by elution with buffer H. Protein concentrations and degrees of labeling were quantified on NanoDrop 2000c Spectrophotometer (Thermo Fisher), before aliquoting and flash freezing.

MST measurements

For each MST assay, unlabeled protein was used to prepare 15-step serial dilution with final volume of 5 μ l in assay buffer (20 mM HEPES/KOH, pH 7.8, 150 mM NaCl, 0.005% Triton X-100, 10 μ M BSA). Next, 5 μ l of 200 nM fluorescence-labeled protein was added to each dilution. For measurements including CaM (except for that with EGTA), 2 mM CaCl₂ was added to the assay buffer. The calmodulin titration was carried out in 1:2 serial dilution, while the others were performed in 1:3 dilution. For the calmodulin competition assay, 30 μ M calmodulin was premixed with 200 nM labeled protein, before being added to 15 serial dilutions. Mixed samples were loaded into Monolith NT.115 Premium Capillaries (NanoTemper) and MST measurements were performed on Monolith NT.115 system (NanoTemper). For assays using labeled ARNO-Sec7 and ARNO-Sec7(4A), samples were pre-incubated at room temperature for 10 min and measured with 60% LED power, 50% MST power. For assays using labeled EGFR-ICD and EGFR-ICD Δ JM₁₋₂₇, samples were pre-incubated at room temperature for 5 min and measured with 20% LED power, 40% MST power. Each sample preparation and measurement was carried out in triplicate. Data analysis was performed using the K_D fitting function of MO.Affinity Analysis v2.3 (NanoTemper) and graphs were prepared using Prism 5.0f (GraphPad). For the calculation of F_{norm} , hot cursor was set at 5 seconds for assays involving labeled ARNO-Sec7 and ARNO-Sec7(4A), while for assays involving labeled EGFR-ICD and EGFR-ICD Δ JM₁₋₂₇, hot cursor was set at 2.5 seconds. Consistently in each interaction plot the fluorescence-labeled compound is shown at first position in the data labels.

Nanodiscs production

Membrane scaffold protein expression and purification

As reported before [43], *E. coli* BL21 (DE3) were transformed with MSP1D1 plasmid DNA in vector pET28a. Cells were grown in LB medium, induced by 1 mM IPTG at an optical density of 0.7, incubated 5-6 hours at 37 °C and pelleted down. Cells were resuspended in buffer B (50 mM Tris/HCl, pH 8.0, 500 mM NaCl) supplemented with 6 M GdnHCl and EDTA-free Complete protease inhibitors (Macherey-Nagel) lysed by sonication (Bandelin Sonopuls MS72 probe), centrifuged at 17 000 g for 1 h (Beckman J2-21 rotor JA-20.1) and incubated 1 h with previously equilibrated 2.5 ml Ni-NTA agarose resin/3 L culture (Macherey-Nagel). Column was washed with 4 CV buffer B, 4 CV buffer B supplemented with 1% Triton X-100, 4 CV buffer B + 60 mM Na-cholate, 4 CV buffer B, 4 CV buffer B + 20 mM imidazole. Four fractions of 1 CV were eluted with 250 mM imidazole. The whole process was kept at 4 °C in a cold room. The elution fractions were pooled and dialyzed against 100-fold dialysis buffer (200 mM Tris/HCl, pH 7.5, 100 mM NaCl). N-terminal His-tag was cleaved using TEV protease incubated overnight at

4 °C. Δ His-MSP was separated from MSP by IMAC and concentrated to the desired molarity using a Vivaspin centrifugal device of 10 kDa MWCO.

Nanodiscs assembly

Nanodiscs were assembled according to established protocols [245,246]. In short, lipids' chloroform stocks were dried under nitrogen flow to obtain a lipid film and stored under vacuum overnight. Δ His-MSP1D1 and the appropriate amount of lipids (Avanti Polar Lipids) solubilized in 60 mM Na-cholate were mixed together in lipid buffer (20 mM Tris/HCl, pH 7.5, 100 mM NaCl, 5 mM EDTA). Four different batches were prepared: one using 100% 1-palmitoyl-2-oleoyl-sn-glycero-3-phosphocholine (POPC) as a non-charged control; one using 30% 1-palmitoyl-2-oleoyl-sn-glycero-3-phospho-L-serine (POPS) and 70% POPC containing 30% net negative charge and similar properties as native membranes; one using 50% POPS and 50% POPC with a higher density of negative charges; one using 50% 1,2-dimyristoyl-sn-glycero-3-phospho-(1'-rac-glycerol) (DMPG) and 50% 1,2-dimyristoyl-sn-glycero-3-phosphocholine (DMPC) containing 50% negative charge and different head group and hydrocarbon chain properties (see main text for more information). The scaffold-to-lipids molar ratio was calculated from geometrical considerations. 20% w/v of previously washed Biobeads SM-2 (Biorad) were added and the mixture incubated at room temperature overnight. The Biobeads were removed by centrifugation and once again 20% w/v were added for an additional 4-5 h. Finally, they were purified by SEC on a HiLoad 16/600 Superdex 200 pg column (GE Healthcare) equilibrated with SEC buffer (20 mM sodium phosphate, pH 7.4, 50 mM NaCl) using a Äkta pure device at a flow rate of 1 ml min⁻¹. The quality of NDs preparation was checked by the SEC chromatogram as well as by DLS (PSS Nicomp). NDs were concentrated to the desired molarity using a Vivaspin centrifugal device of 10 kDa MWCO.

NMR Spectroscopy

All NMR experiments were performed on Bruker Avance III HD⁺ spectrometers operating either at 600 or 700 MHz, both equipped with 5 mm inverse detection triple-resonance z-gradient cryogenic probes. Data was collected at 32 or 15 °C and processed with TOPSPIN 3.2 (Bruker BioSpin). 4,4-dimethyl-4-silapentanesulfonic acid (DSS) was used as a chemical shift standard, and ¹³C and ¹⁵N data were referenced using frequency ratios as previously described [247].

Sec7 and JM resonance assignment

For the resonance assignment of Sec7 and JM, triple (U[²H,¹³C,¹⁵N]) and double-labelled (¹³C,¹⁵N) samples were prepared, respectively. The U[²H,¹³C,¹⁵N] and double-labelled (¹³C,¹⁵N]-Sec7 sample was prepared at a concentration of 360 μ M in 20 mM sodium phosphate buffer pH 7.4 containing 300 mM NaCl, 10% (v/v) D₂O, 0.01% sodium azide and 100 μ M DSS. The ¹³C,¹⁵N-JM sample was prepared at a concentration of 270 μ M in 20 mM sodium phosphate buffer pH 5.5 containing 100 mM NaCl, 10% (v/v) D₂O, 0.01% sodium azide and 100 μ M

6 Interaction of ARNO-Sec7 with juxtamembrane segment of EGFR

DSS. The lower pH in this sample was used in order to avoid residue-amide exchange with the solvent. TROSY versions (Tr) of ^{15}N -edited HSQC and three-dimensional HNCO, HN(CA)CO, HN(CO)CACB (or CBCA(CO)NH, for JM) and HNCACB experiments were performed to obtain the chemical shift assignments of the backbone atoms of Sec7, while the standard versions were used for JM. Furthermore, for the assignment of the sidechain resonances of JM we also acquired a ^{13}C -edited HSQC and a 3D hCCH-TOCSY. The assignment of the ^1H , ^{13}C , and ^{15}N signals in the spectra was performed using CARA 1.9.24a [248]. Data was acquired at 32 and 15 °C for U[^2H , ^{13}C , ^{15}N]-Sec7 and ^{13}C , ^{15}N -JM, respectively. Table 6.1 and Table 6.2 summarize the acquisition parameters for Sec7 and JM, respectively.

Table 6.1: Acquisition parameters of the spectra used for Sec7 resonance assignment.

| | Number of points | | | Spectral width (ppm) | | | Central frequency (ppm) | | | NS |
|--|------------------|------|-----|----------------------|----|----|-------------------------|-------|-----|----|
| | F3 | F2 | F1 | F3 | F2 | F1 | F3 | F2 | F1 | |
| 2D | | | | | | | | | | |
| ^1H , ^{15}N -TrHSQC | - | 2048 | 128 | - | 14 | 36 | - | 4.704 | 116 | 64 |
| 3D | | | | | | | | | | |
| TrHNCO | 2048 | 40 | 128 | 14 | 36 | 22 | 4.704 | 116 | 176 | 8 |
| TrHN(CA)CO | 2048 | 40 | 128 | 14 | 36 | 22 | 4.704 | 116 | 176 | 24 |
| TrHN(CO)CACB | 2048 | 40 | 128 | 14 | 36 | 75 | 4.704 | 116 | 39 | 24 |
| TrHNCACB | 2048 | 40 | 128 | 14 | 36 | 75 | 4.704 | 116 | 39 | 32 |

Table 6.2: Acquisition parameters of the spectra used for JM resonance assignment.

| | Number of points | | | Spectral width (ppm) | | | Central frequency (ppm) | | | NS |
|--------------------------------------|------------------|------|-----|----------------------|----|----|-------------------------|-------|-------|----|
| | F3 | F2 | F1 | F3 | F2 | F1 | F3 | F2 | F1 | |
| 2D | | | | | | | | | | |
| ^1H , ^{15}N -HSQC | - | 2048 | 256 | - | 13 | 30 | - | 4.697 | 119.5 | 32 |
| ^1H , ^{13}C -HSQC | - | 1024 | 512 | - | 13 | 75 | - | 4.696 | 42 | 32 |
| 3D | | | | | | | | | | |
| HNCO | 2048 | 40 | 128 | 13 | 30 | 22 | 4.697 | 119.5 | 176 | 8 |
| HN(CA)CO | 2048 | 40 | 128 | 13 | 30 | 22 | 4.697 | 119.5 | 176 | 16 |
| CBCB(CO)NH | 2048 | 40 | 128 | 13 | 30 | 80 | 4.697 | 119.5 | 42 | 32 |
| HNCACB | 2048 | 40 | 128 | 13 | 30 | 80 | 4.697 | 119.5 | 42 | 32 |
| hCCH-TOCSY | 2048 | 40 | 128 | 13 | 75 | 75 | 4.697 | 42 | 42 | 16 |

Sec7 titration with JM

The residues of Sec7 responsible for binding were identified by titrating a sample of ^{15}N -labeled Sec7 with increasing amounts of non-labelled JM and acquiring a ^1H - ^{15}N -HSQC spectrum at each titration point. The concentration of protein was maintained at $60\ \mu\text{M}$ and the concentration of JM varied from 0 to $420\ \mu\text{M}$ (using seven individual samples at 0.0, 0.5, 1.0, 2.0, 3.0, 5.0 and 7.0 molar equivalents). The ^1H - ^{15}N -HSQC spectra were acquired with 2048×128 points and 256 scans. Spectral widths were 14 ppm for ^1H and 36 ppm for ^{15}N . The central frequency for proton was set on the solvent signal (4.704 ppm) and for nitrogen was set on the center of the amide region (116 ppm). The data was acquired in 20 mM sodium phosphate buffer containing 100 mM NaCl, 10% (v/v) D_2O , 0.01% sodium azide and $100\ \mu\text{M}$ DSS, pH 7.4. All data was acquired at $32\ ^\circ\text{C}$.

JM titration with Sec7, NDs and CaM

The residues of JM responsible for binding were identified in a similar way as described above, using ^{15}N -labeled JM and non-labelled Sec7. The concentration of JM was maintained at $40\ \mu\text{M}$ and the concentration of Sec7 varied from 0 to $280\ \mu\text{M}$ (using five individual samples at 0.0, 2.0, 3.0, 5.0 and 7.0 molar equivalents). The ^1H - ^{15}N -HSQC spectra were acquired with 2048×128 points and 8 scans. Spectral widths were 13 ppm for ^1H and 30 ppm for ^{15}N . The central frequency for proton was set on the solvent signal (4.695 ppm) and for nitrogen was set on the center of the amide region (119.5 ppm). The data was acquired in 20 mM sodium phosphate buffer containing 100 mM NaCl, 10% (v/v) D_2O , 0.01% sodium azide and $100\ \mu\text{M}$ DSS, pH 5.5. All data was acquired at 15 and $32\ ^\circ\text{C}$.

To study the interaction of JM with the different NDs we measured ^{15}N -edited HSQC spectra of the free ^{15}N -JM ($40\ \mu\text{M}$) and in the presence of $20\ \mu\text{M}$ of NDs, containing the different lipids (note that this will result on average in one JM per membrane leaflet). The ^1H - ^{15}N -HSQC spectra were acquired with 2048×128 points and 8 scans. Spectral widths were 15 ppm for ^1H and 30 ppm for ^{15}N . The central frequency for proton was set on the solvent signal (4.703 ppm) and for nitrogen was set on the center of the amide region (119.5 ppm). The data was acquired in 20 mM sodium phosphate buffer containing 100 mM NaCl, 10% (v/v) D_2O , 0.01% sodium azide and $100\ \mu\text{M}$ DSS, pH 5.5. All data was acquired at $32\ ^\circ\text{C}$.

The interaction between JM and calmodulin (CaM) was measured using ^{15}N -edited HSQC experiments with $100\ \mu\text{M}$ ^{15}N -labeled JM in absence and presence of $400\ \mu\text{M}$ CaM in 20 mM sodium phosphate buffer, pH 5.5, with 150 mM NaCl, 10% (v/v) D_2O , 0.01% sodium azide and $100\ \mu\text{M}$ DSS. The spectra were acquired with 2048×128 points and the central frequency for protons were set on the solvent signal (4.690 ppm) and for nitrogens on 119.5 ppm. The spectral widths for ^1H and ^{15}N were set to 13 ppm and 30 ppm, respectively. Both spectra were acquired with 16 scans at $15\ ^\circ\text{C}$. Data for JM's three N-terminal Arginines was not unambiguous and, where shown, could reflect either only on Arg647 or also on Arg646 and/or Arg645. Signal for His648 was considerably weaker as for all other assigned residues and not always clearly distinguishable from spectral noise. In unclear cases, the residue was removed from analysis.

JM_{sc} titration with Sec7

To investigate the effect of the overall charge of JM in binding we prepared a scrambled version of JM, JM_{sc}, containing a redistributed but overall identical amino acid composition with the sequence:RELKHIQVRLRTERQLEPLEIRAVNRSRLTPRLAGLPR (positively and negatively charged residues are colored in blue and red, respectively).

We measured a ¹⁵N-edited HSQC spectrum of the free JM_{sc} (40 μM) and in the presence of 7.0 equivalents of Sec7 (280 μM). The ¹H-¹⁵N-HSQC spectra were acquired with 2048 × 128 points and 8 scans. Spectral widths were 13 ppm for ¹H and 30 ppm for ¹⁵N. The central frequency for proton was set on the solvent signal (4.701 ppm) and for nitrogen was set on the center of the amide region (119.5 ppm). The data was acquired in 20 mM sodium phosphate buffer containing 100 mM NaCl, 10% (v/v) D₂O, 0.01% sodium azide and 100 μM DSS, pH 5.5. All data was acquired at 32 °C.

Combined Chemical Shift, $\Delta\delta_{\text{comb}}$

For the evaluation of the behavior of individual amino acids upon addition of increasing amounts of ligand we calculated the combined amide proton and nitrogen chemical shift differences using Eq. (6.1) [249]:

$$\Delta\delta_{\text{comb}} = \sqrt{(\Delta\delta_H)^2 + (0.1 \times \Delta\delta_N)^2} \quad (6.1)$$

where $\Delta\delta_H$ and $\Delta\delta_N$ are the chemical shifts of proton and nitrogen, respectively. In order to decide whether a given residue belongs to the class of interacting or non-interacting residues, we have calculated a corrected standard deviation to zero (σ_0^{corr}) [249].

Sec7 and JM Resonance Assignment

Despite existence of an NMR structure of Sec7 [226], the experimental assignments are not available. As such, a *de novo* assignment was carried out. The backbone assignment of the amide resonances of Sec7 and JM has been performed using a standard triple resonance approach [250]. For Sec7, the amide resonances of amino acids S1, E2, T3, R4, Q5, R6, Y44, G48, K51, T52, F73, D74, L75, H76, R88, S93, F94, R95, L96, A100, Q101, K102, I103, D104, R105, M106, T125, N144, R148, D149 and L150 could not be assigned (possibly due to exchange with the solvent). The Chemical Shift Index (CSI) [251] was used to identify protein secondary structure and compare it with the deposited structures [226, 228] (Fig. 6.13). The secondary structure of Sec7 was predicted for each assigned amino acid residue using Eq. (6.2)

$$CSI = \Delta\delta C_\alpha - \Delta\delta C_\beta \quad (6.2)$$

where CSI is the Chemical shift index and $\Delta\delta C_\alpha$ and $\Delta\delta C_\beta$ are the variations of the measured C_α and C_β chemical shifts with respect to random coil values. Three or more consecutive negative values indicate β -strand while three or more positive values indicate a α -helical structure.

Data and Software Availability

NMR chemical shift assignment of Sec7 are deposited in the BMRB data bank under the number: 27761.

Conclusion and key achievements

A large number of cellular processes is regulated by a complex interplay between several hormones, membrane-embedded proteins and lipids. Finding a suitable membrane mimetic system for membrane protein stabilization as well as for interaction studies with peptides remains still challenging and this work explored approaches to overcome these limitations.

One main aspect was the characterization of the interaction network of melanocortin-4 Receptor (MC4R) and its ligands. Ensuring expression of active receptor in sufficient amounts, we established functional expression of MC4R in different eukaryotic expression systems, such as HEK293, Sf9 and Tnao38 cell lines (Chapter 2). The newly developed Tnao38 cell line not only gave the best expression rate, we could also establish that this cell line can be used for downstream activity assays. However, HEK293 cells with more moderate MC4R expression turned out to be more suitable for activation studies of MC4R. With the help of a fluorescence-based cAMP activity assay we were able to study the potency of different ligands to activate MC4R.

Further, we explored the recently described [140] interaction of the bone-derived hormone lipocalin 2 (LCN2) with MC4R (Chapter 3). Both, human and murine homologues of LCN2 could be expressed and purified with high purity and in sufficient amounts from *E. coli*. However, neither human nor murine LCN2 showed dose-dependent activation of MC4R which clearly contradicts the previously reported interaction.

To complement our *in situ* insights into MC4R pharmacology, we explored the potential of the styrene-maleic acid (SMA) technology for the purification of MC4 receptor from Tnao38 cell membranes (Chapter 2). Once the conditions for solubilization were optimized, we could successfully use SMA for purification of MC4R from Tnao38 membranes. However, MC4R-SMA lipid particles (SMALPs) displayed a large degree of heterogeneity as proved by electron microscopy and gel filtration. Further optimization processes have to be performed to form more monodispers particles which then can be used for further downstream experiments.

In order to develop a new screening assay for investigation of lipid/ protein interaction we used SMALPs in combination with microfluidic diffusional sizing (Chapter 4). We could show that the MC4R agonist adrenocorticotrophic hormone (ACTH) binds to SMALPs in a lipid-dependant manner demonstrating that the method is capable to detect lipid specificity of peptide-lipid interaction.

We have shown in Chapter 5 that α Syn-LiPs can be used to induce, accelerate or inhibit α Syn amyloid fibril formation. In addition, we have shown that usage of anionic lipids in combination with low ionic strength of the sample buffer leads to α Syn-LiPs formed with a higher number of α Syn molecules per LiP. Since about half of the α Syn proteins can be detached from these α Syn-LiPs by increasing the ionic strength of the buffer while the other half remains attached to LiPs, we attribute this observation to the contribution of an electrostatically driven binding of α Syn to the negatively charged membrane surface. The presence of α Syn-LiPs in the used aggregation assays evidently induces distinguishable modulations of the aggregation behavior. Our EM data show connections between short fibrillar structures and α Syn-LiPs that could reflect on early lipid induced nucleation events. Our data clearly demonstrate that α Syn-LiPs

display useful features including (i) a very strong capability to induce primary nucleation, (ii) the possibility to store frozen α Syn-LiP stock solutions, simplifying handling and minimizing artifacts by batch-to-batch variations, and (iii) a not detectable influence on the morphology of fibrils that have formed and grown in the presence α Syn-LiPs. However, more thorough investigations will be needed to understand the formation and role of these fibril-LiP complexes and whether they play a role in the amyloid fibril formation process.

In chapter 6, we identified ADP ribosylation factor nucleotide binding-site opener (ARNO), a member of the cytohesin family, as JM-binding protein. Using solution NMR spectroscopy and microscale thermophoresis, supported by site-directed mutagenesis techniques, we could structurally characterize the ARNO-EGFR interaction interface. We reveal that its binding mode displays common features and distinct differences with JM's interaction with calmodulin and anionic phospholipids. Furthermore, we were able to show that each interaction can be modulated by additional factors. In doing so, we could generate a distinctly regulated network of possible EGFR modulators acting on the intracellular domain of the receptor.

Overall, our results may help to better understand the role of lipids on several cellular events and introduce new means to better characterize these essential processes.

List of publications

The following publications reflect the content of this dissertation, either already accepted or in preparation:

Chapter 5:

Falke M, Victor J, Wördehoff MM, Peduzzo A, Zhang T, Schröder GF, Buell AK, Hoyer W, Etzkorn M. α -Synuclein-derived lipoparticles in the study of α -Synuclein amyloid fibril formation. *Chem Phys Lipids* 220, 57-65 (2019) DOI: 10.1016/j.chemphyslip.2019.02.009

Contribution: Prepared samples. Carried out all kinetics, DLS, FITR and microfluidic measurements. Contributed to process and interpret all data. Participated in writing and reviewing the manuscript.

Chapter 6:

Viegas A, Yin DM, Borggräfe J, Viennet T, **Falke M**, Schmitz A, Famulok M, Etzkorn M. Molecular Architecture of a Network of Potential Intracellular EGFR modulators: ARNO, CaM, Phospholipids, and the Juxtamembrane Segment. *Structure* 28 (1), 54-62 2020 DOI: 10.1016/j.str.2019.11.001

Contribution: Prepared nanodisc samples. Contributed to review the manuscript.

Chapter 2:

Schriek S, **Falke M**, Viegas A, Viennet T, Dahlhaus M, Etzkorn M. Melanocortin signaling: modulation through membrane and calcium interactions. *In preparation*

Contribution: Participated in cell culture experiments and biochemical assays.

Chapter 2:

Falke M, Ortmann C, Tripailo A, Dahlhaus M, Etzkorn M. Insights into Hormone-GPCR Interactions: Enhancing eukaryotic MC4R expression for structural studies. *In preparation*

Contribution: Compiled literature. Designed and performed the experiments. Contributed to process and interpret all data.

Chapter 3:

Falke M, Ortmann C, Tripailo A, Schloesser R, Borggräfe J, Etzkorn M. Lipocalin 2 does not activate MC4R *in situ*. *In preparation*

Contribution: Compiled literature. Designed and performed the experiments. Contributed to process and interpret all data.

Chapter 4:

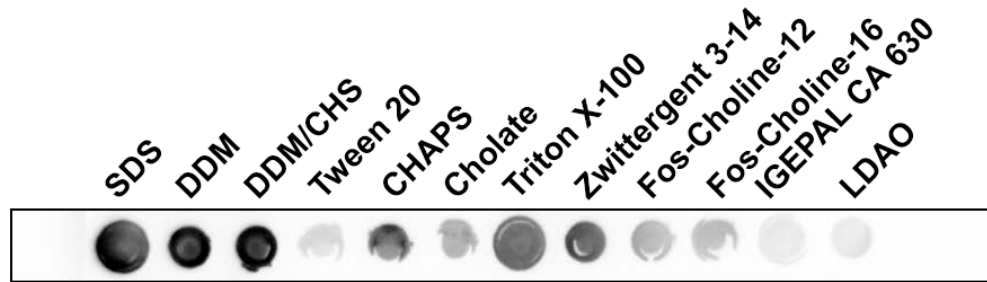
Falke M, Victor J, Etzkorn M. SMALPs as a tool for lipid-peptide interaction. *In preparation*

Contribution: Compiled literature. Designed and performed the experiments. Participated in processing and interpretation of data.

Supplementary data

MC4R (Chapter 2)

a



b

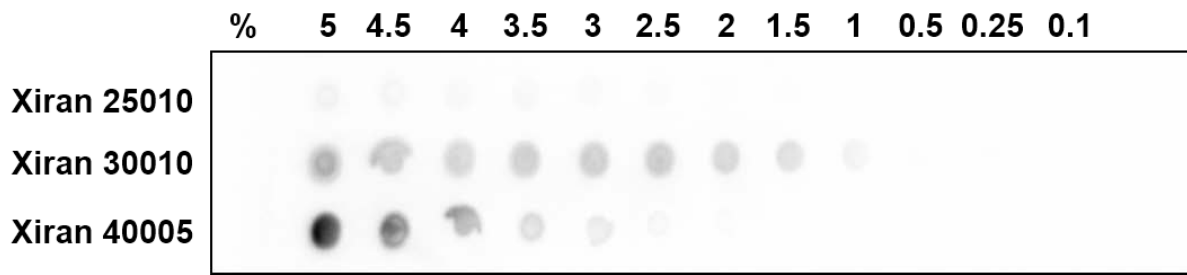


Figure 6.6: Solubilization screen of MC4R using Dot blot. Solubilization screen of Tnao38 membranes containing MC4R with detergent (a) and styrene-maleic acid (b). 2 μ l of solubilized protein was spotted onto a nitrocellulose membrane. Immunostaining was performed using anti-FLAG tag antibody. Analysis of dot blot intensities is shown in Fig. 2.7a,b.

6 Interaction of ARNO-Sec7 with juxtamembrane segment of EGFR

LCN2 (Chapter 3)

```

hMC4R    1  MVNSTHFGMHTSLHLWNRSSYRLHSNASESLGKGYSDGGCYEQLFVSPVFTLVISLL
mMC4R    1  MNSTHFGMYTSLHLWNRSSYGLHGNASESLGKGFHDGGCYEQLFVSPVFTLVISLL

hMC4R    61  ENILVIVAIAKNKNLHSPMYFFICSLAVADMLVSVSNGSETIVITLLNSTDTDAQSFTVN
mMC4R    61  ENILVIVAIAKNKNLHSPMYFFICSLAVADMLVSVSNGSETIVITLLNSTDTDAQSFTVN

hMC4R    121  IDNVIDSVICSSLLASICSLLSIAVDRYFTIFYALQYHNIMTVKRVGIIISCIWAACTVS
mMC4R    121  IDNVIDSVICSSLLASICSLLSIAVDRYFTIFYALQYHNIMTVRRVGIISCIWAACTVS

hMC4R    181  GILFIIYSDSSAVIICLIIMFFTMLALMASLYVHMFLMARLHIKRIAVLPGTGAIROGAN
mMC4R    181  GVLFIYSDSSAVIICLISMFFTMLVLMASLYVHMFLMARLHIKRIAVLPGTGTIRQGTN

hMC4R    241  MKGAILTLILIGVFVVCWAPFFLHLIFYISCPQNPYCVCFMSHFNLYLILIMCNSTIDPL
mMC4R    241  MKGAILTLILIGVFVVCWAPFFLHLIFYISCPQNPYCVCFMSHFNLYLILIMCNAVIDPL

hMC4R    301  IYALRSQELRKTfKEIICCYPLGGICDLSSRY
mMC4R    301  IYALRSQELRKTfKEIICEYPLGGICELSSRY

```

Figure 6.7: Protein sequence alignment of human and murine MC4R. Sequence alignment was performed using Boxshade version 3.21. Black boxes indicate identical residues whereas conserved residues are shaded in grey.

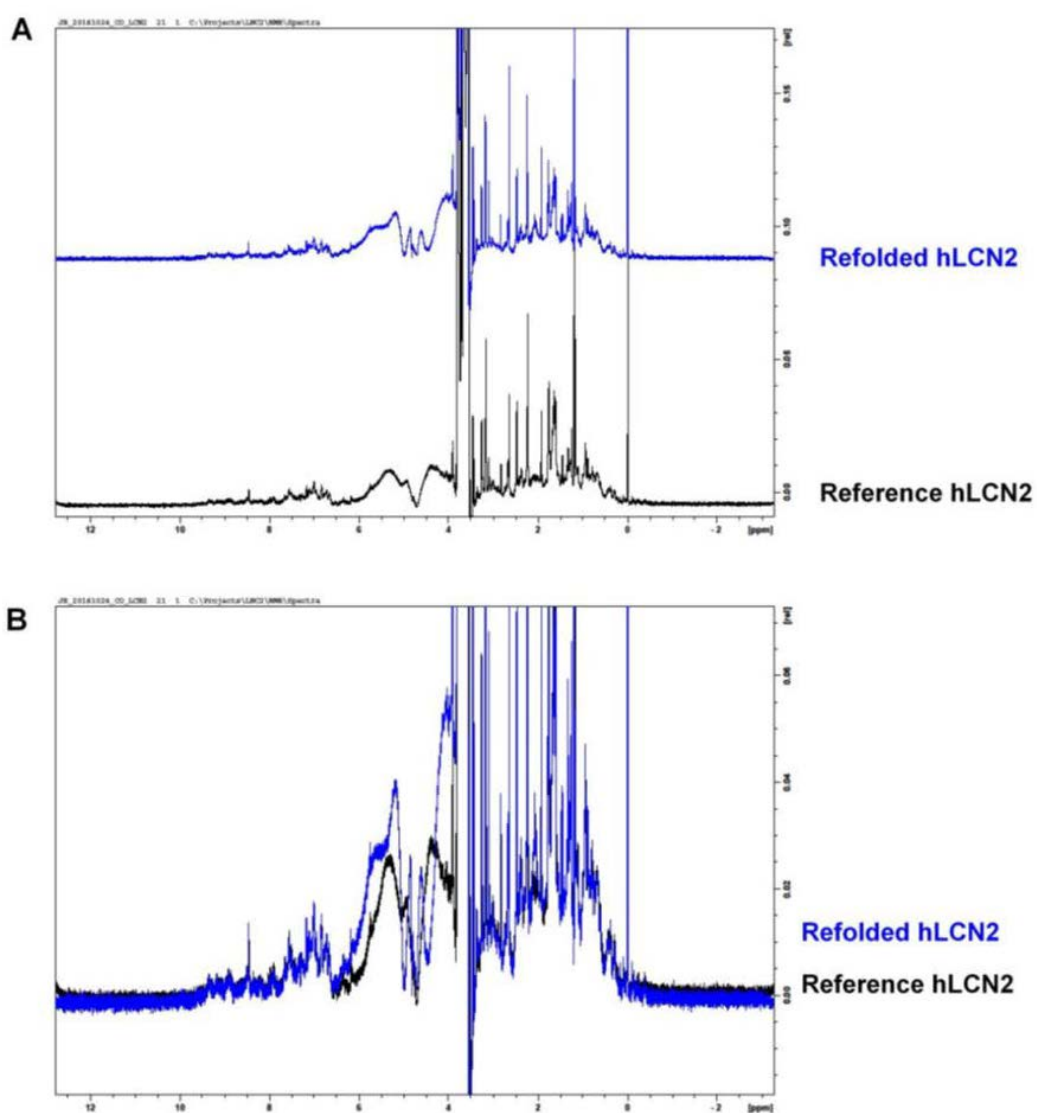


Figure 6.8: Verification of LCN2 refolding by NMR. 1D proton spectrum of purified and refolded human LCN2. A) Magnified region of proton 1D spectra of refolded hLCN2 and reference hLCN2 (Fig. 3.1). B) Overlaid and zoomed in view of the region of proton 1D spectra from A). Measurements were taken on Bruker 700 MHz spectrometer, all samples were supplemented with 10% D₂O and DSS as reference.

6 Interaction of ARNO-Sec7 with juxtamembrane segment of EGFR

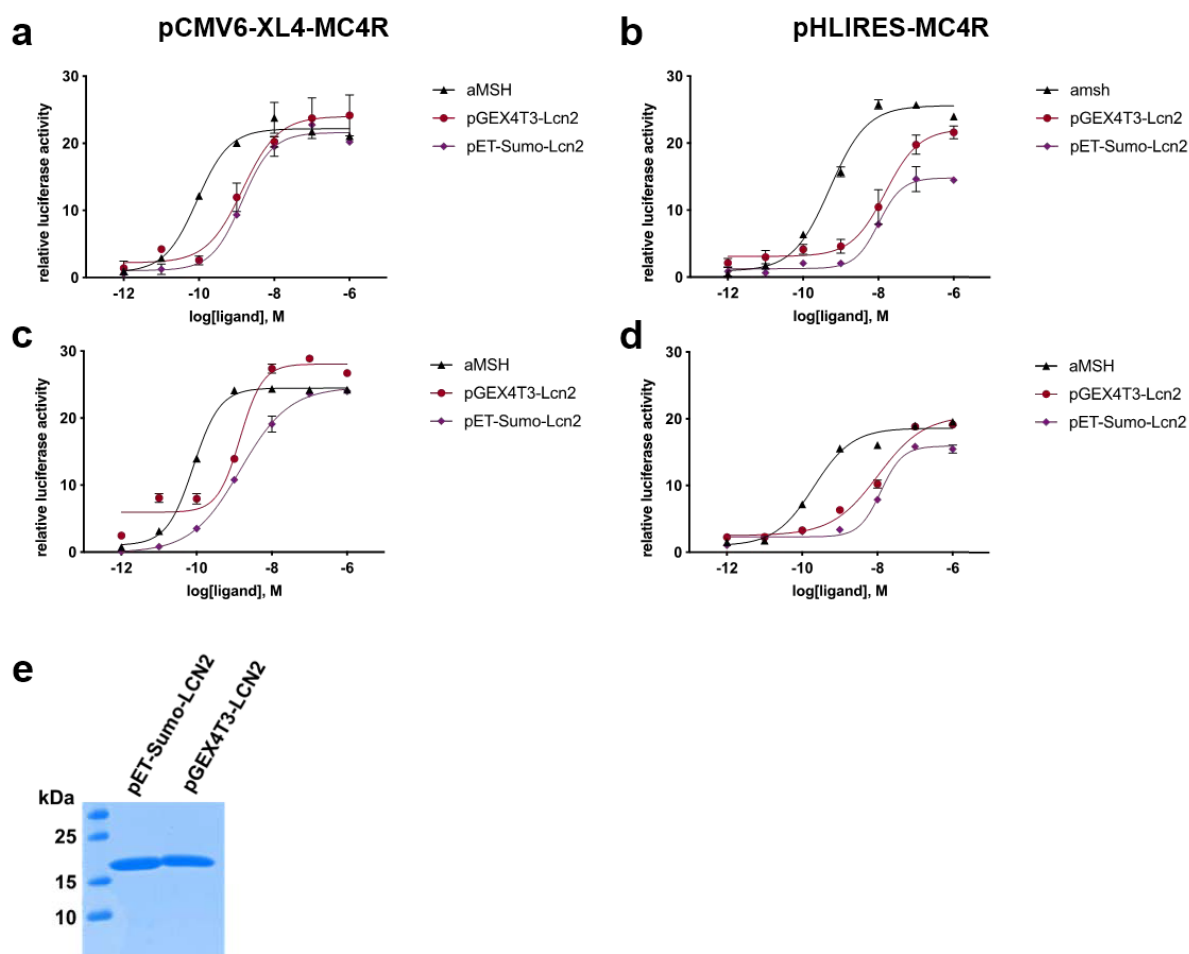


Figure 6.9: Functional characterization of murine LCN2 in HEK293T-MC4R cells by Reporter Gene assay. The assay was performed as described by Mosialou *et al.* [140]. Agonist activity of mLCN2 protein produced in our lab (pET-Sumo-LCN2) and in lab of Mosialou *et al.* (pGEX4T3-LCN2) were tested at HEK293T cells expressing MC4R from our lab (pHLIRES-MC4R, b) and d)) and lab of Mosialou *et al.* (pCMV-XL4-MC4R, a) and c)). 2 independent experiments were performed. e) LCN2 purity was verified by SDS-PAGE.

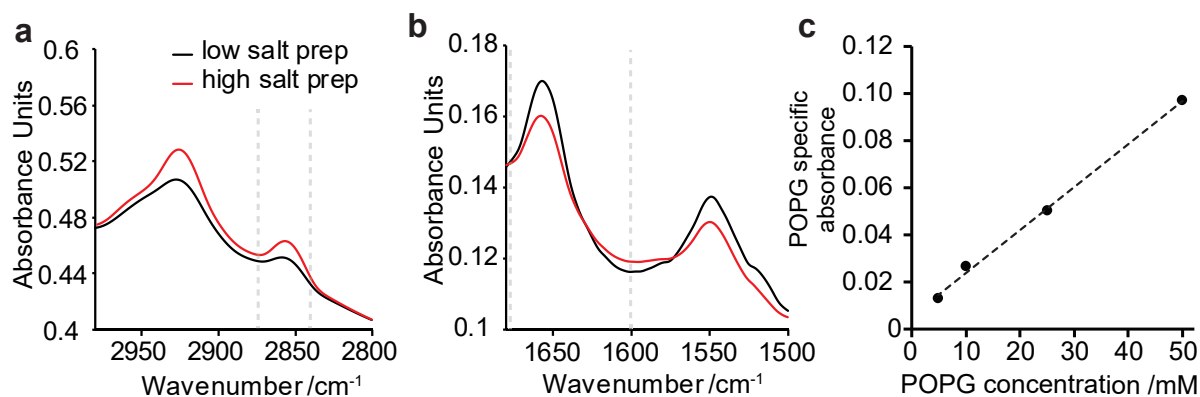
α Syn-LiPs (Chapter 5)

Figure 6.10: FTIR data of α Syn-LiPs after SEC. Spectral regions used for quantification of lipid a) and protein b) amounts. Baseline adjusted spectra of α Syn-LiPs prepared in low- (black) or high-salt (red) conditions are shown. While protein quantification is done automatically (using multiple spectral regions), lipid quantification requires a lipid-specific calibration curve, which we recorded using different concentrations of POPG in constant concentration of Na-choleate c). Final lipid quantification was carried out after subtracting the respective buffer background spectra in triplicate experiments.

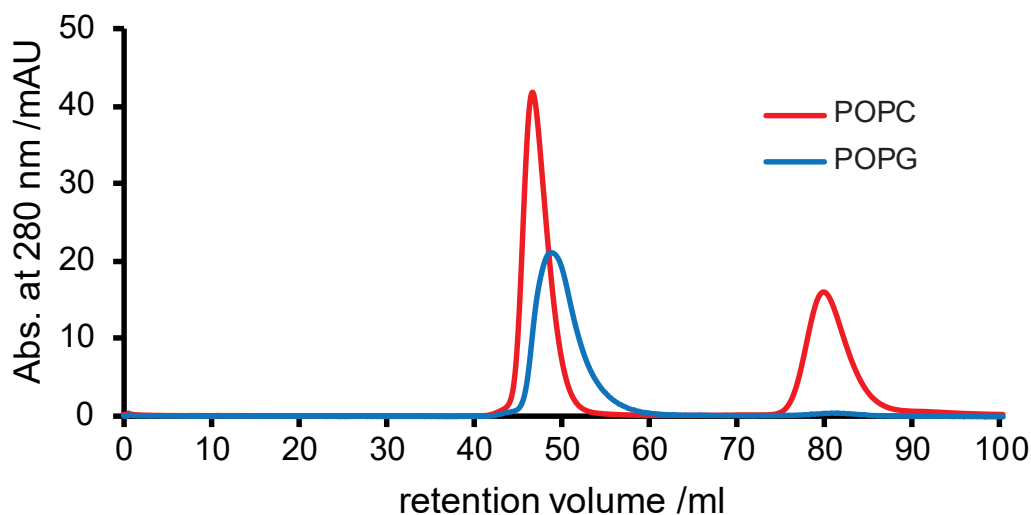


Figure 6.11: Preparative SEC data of freshly prepared α Syn-LiPs assembled with POPC (red) or POPG (blue) lipids. Both preparations were carried out in parallel and under identical (low salt) conditions. In line with results of high-salt treatment of POPG α Syn-LiPs (Fig. 5.1c), the usage of the neutral POPC lipids also results in larger fraction of monomeric α Syn not attached to the LiPs at the used protein-to-lipid ratio of 1:40.

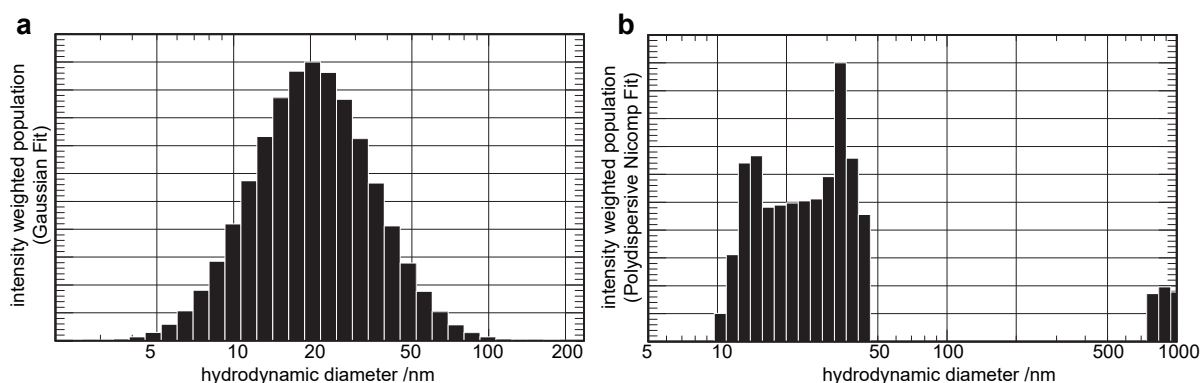


Figure 6.12: DLS data of POG α Syn-LiPs after SEC. Histograms are based on the identical measurement as shown in Fig. 5.1e, but using different fitting algorithms. a) Result of intensity-weighted gaussian fit, assuming a monodisperse particle distribution. The average particle size obtained with this method is similar to the one obtained using microfluidic sizing, which also reports on the average value of all particles (Fig. 5.1f). b) Results of intensity weighted polydispersive fit using the instrument's internal, so called Nicomp, algorithm. The histogram again shows heterogenous particle distribution in the range of 10-50 nm. In addition a fraction of large particles (> 500 nm) with an overall intensity contribution of 16% is detected. Since the DLS measurements were recorded on the same sample, which also shows fibrillar structures in EM images (Fig. 5.3b,e,f), it can be assumed that these structures contribute to the large particle sizes in the DLS histogram. Note that the intensity-weighted distribution is shown, which, due to the large intensity dependence of the DLS signal, translates to a population of below 0.1% fibrillar structures (volume weighted).

ARNO-Sec7 (Chapter 6)

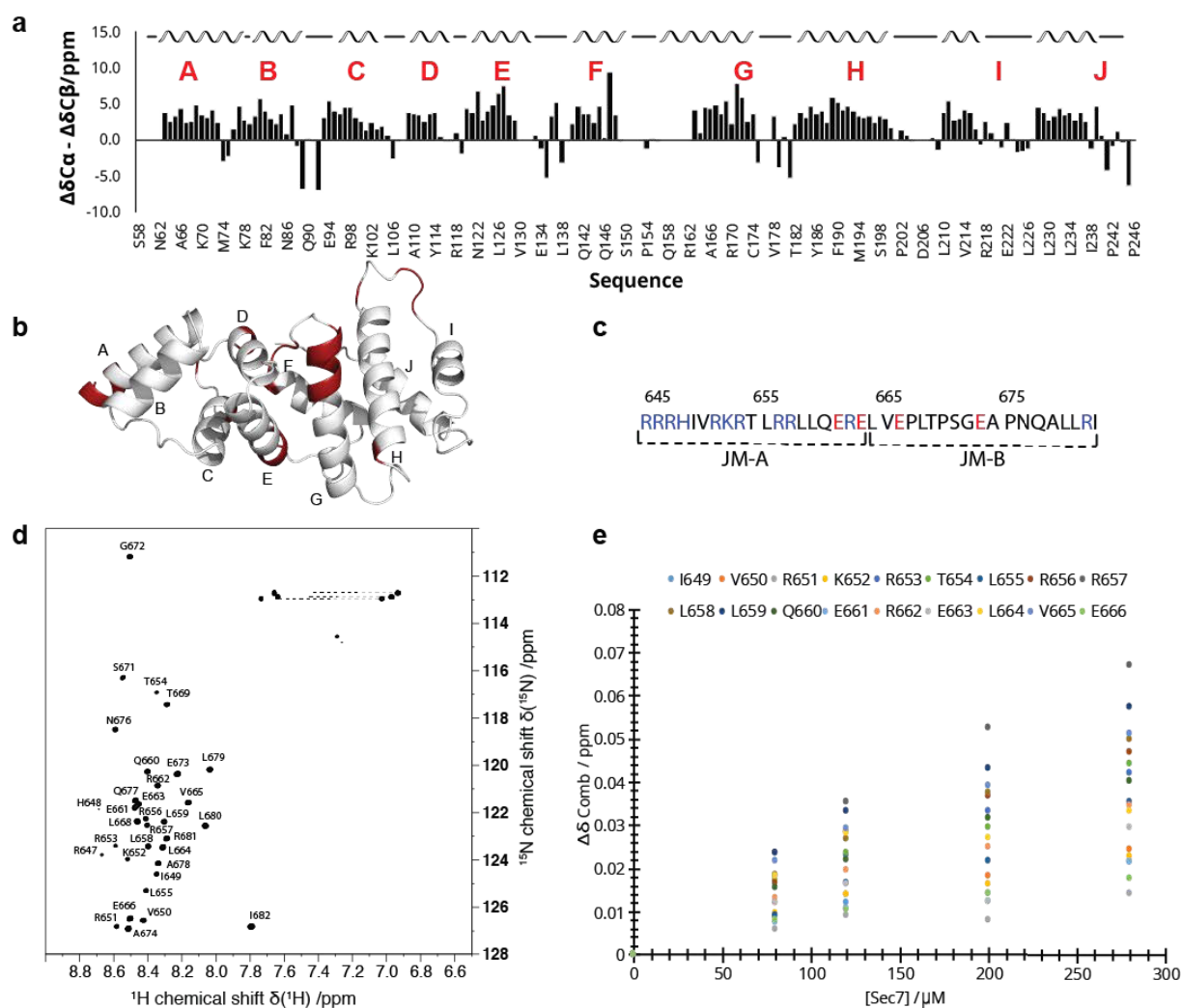


Figure 6.13: related to Fig. 6.1 and Fig. 6.2. CSI-predicted secondary structure of Sec7 based on $^{13}\text{C}_{\alpha}$ and $^{13}\text{C}_{\beta}$, chemical shifts (Chemical Shift Index). Three or more consecutive negative values indicate β -strand while three or more positive values indicate a α -helical structure. On top of the plot the secondary structure as defined by the crystal structure is shown (PDB code: 4JMI (32)) b) Crystal structure of Sec7 depicting the non-assigned residues in red. Helix nomenclature is according to [227]. Data was acquired at 32 °C. c) Sequence of JM highlighting positively and negatively charged residues in blue and red, respectively. JM can be divided into 2 segments: JM-A (residues R645 to E663) and JM-B (residues L664 to 682) (4). For JM, nearly complete backbone resonance assignment was obtained and only the amide resonances of R645 and R646 could not be assigned. d) ^{15}N - ^1H -HSQC with assignment of JM in aqueous solution. Data was acquired at pH 5.5 and 15 °C. e) Combined chemical shift for the JM titration with Sec7, as a function of the sequence. Only the residues affected (corresponding to JM-A) are represented. The concentration of JM was maintained at 40 μM and the concentration of Sec7 varied from 0 to 280 μM (0.0, 2.0, 3.0, 5.0 and 7.0 molar equivalents). Data was acquired at 15 °C in 20 mM sodium phosphate buffer containing 100 mM NaCl, 10% (v/v) D_2O , 0.01% sodium azide and 100 μM DSS, pH 5.5. Due to the absence of a clear plateau (before reaching the solubility limit of the titrant) no residue specific affinities were calculated. The behavior is however in line with K_D values in the high μM range.

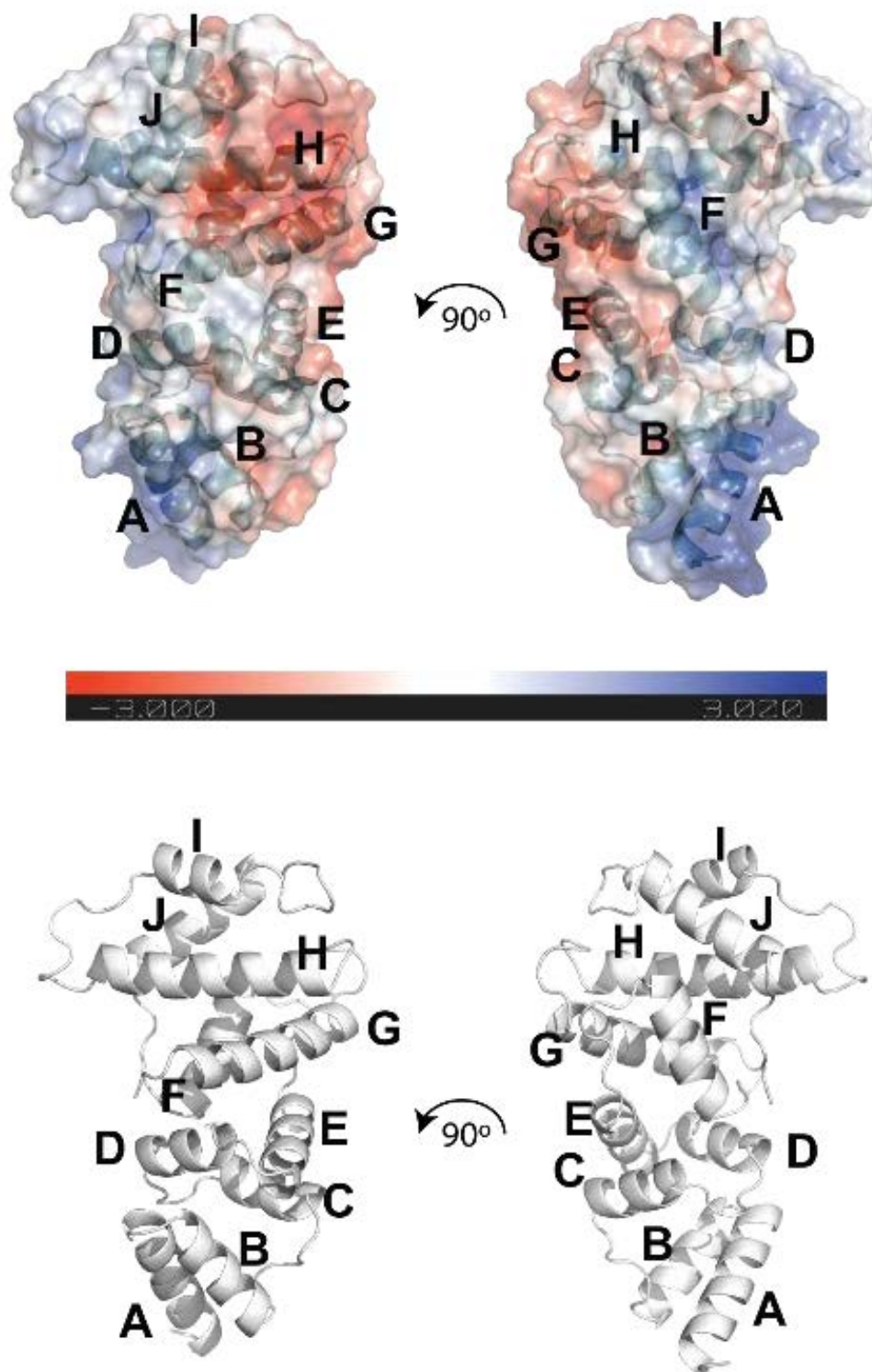


Figure 6.14: related to Fig. 6.2. Electrostatic surface of Sec7. The electrostatic surface was calculated using the APBS Electrostatics module of PyMol. Helix nomenclature is according to [227].

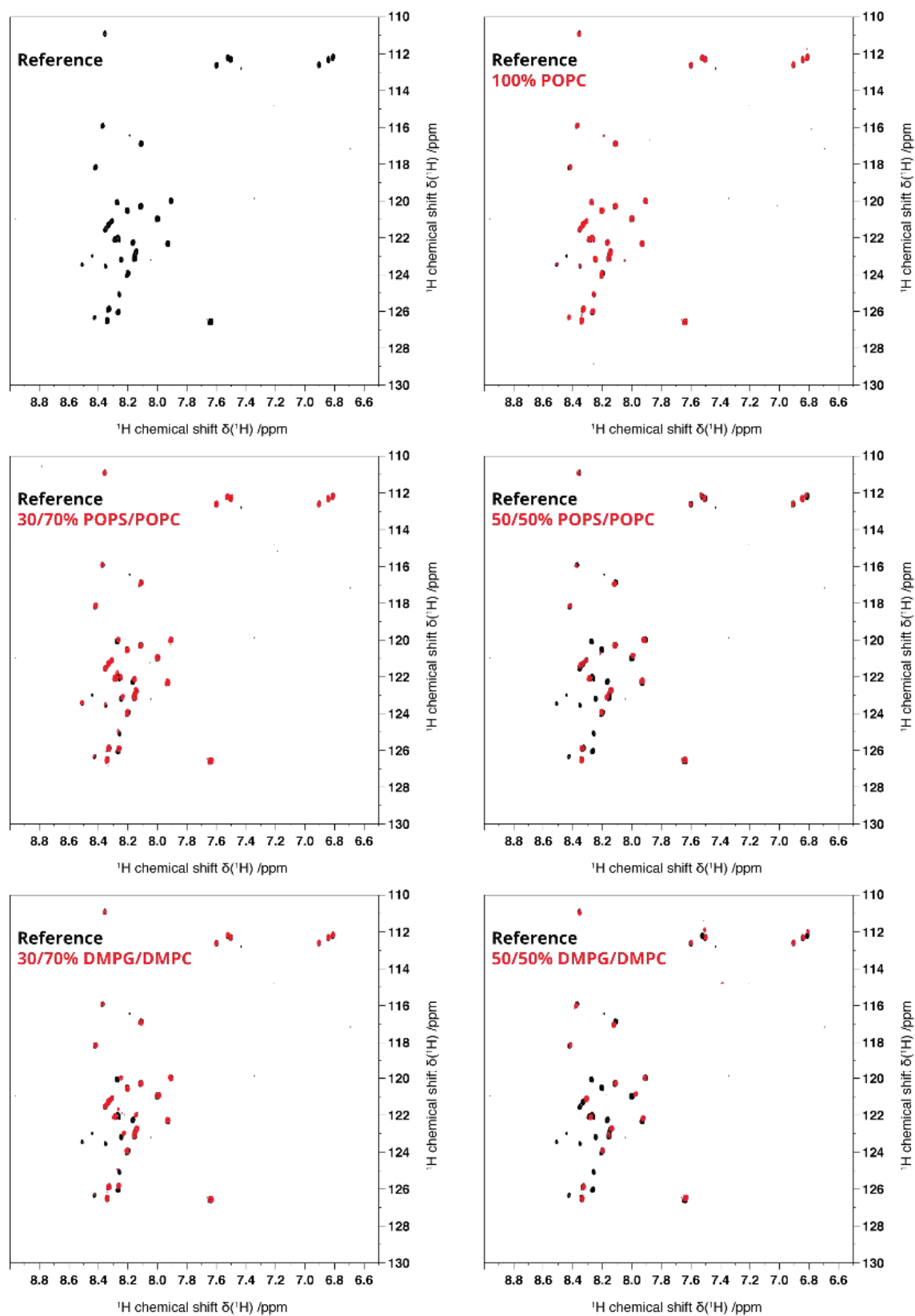


Figure 6.15: related to Fig. 6.3. JM ^{15}N , ^1H -HSQC spectra in the absence (black) and presence of NDs containing the indicated different lipid compositions (red).

6 Interaction of ARNO-Sec7 with juxtamembrane segment of EGFR

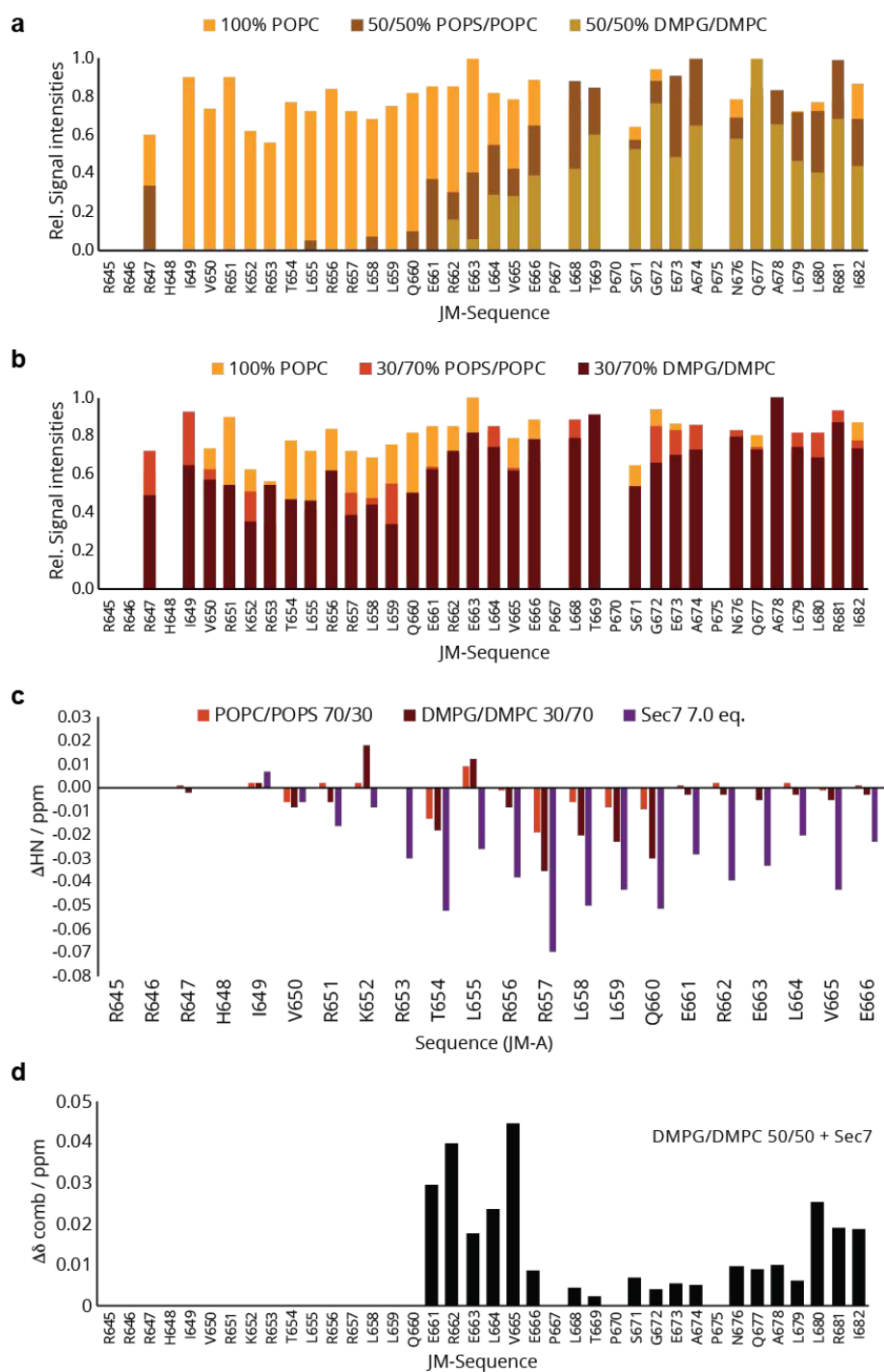


Figure 6.16: related to Fig. 6.4. Interactions of JM with NDs containing different lipids. Relative signal intensities in absence and presence of nanodiscs containing a) 100% POPC, 30/70% POPS/POPC and 30/70% DMPG/DMPC; b) 100% POPC, 50/50% POPS/POPC and 50/50% DMPG/DMPC. c) JM-A amide proton chemical shift deviations upon addition of different interaction partners. The rather uniformly shift towards lower ^1H and ^{15}N frequencies would be in line with an increase in transient α -helical propensity upon Sec7 interaction [223]. d) Combined chemical shift ($\Delta\delta_{\text{comb}}$) perturbations of JM in the presence of 1 equivalent of NDs containing a mixture of 50% DMPG/50% DMPC and of 7 equivalents of Sec7. The resonances of the amide groups up to Q660 are bleached from the $^{15}\text{N}, ^1\text{H}$ -HSQC spectrum upon addition of the NDs (Fig. 6.15) and are not recovered upon addition of Sec7. However, the chemical shift perturbations displayed by residues E661-V665 demonstrate that even in the presence of NDs, Sec7 is able to interact with JM.

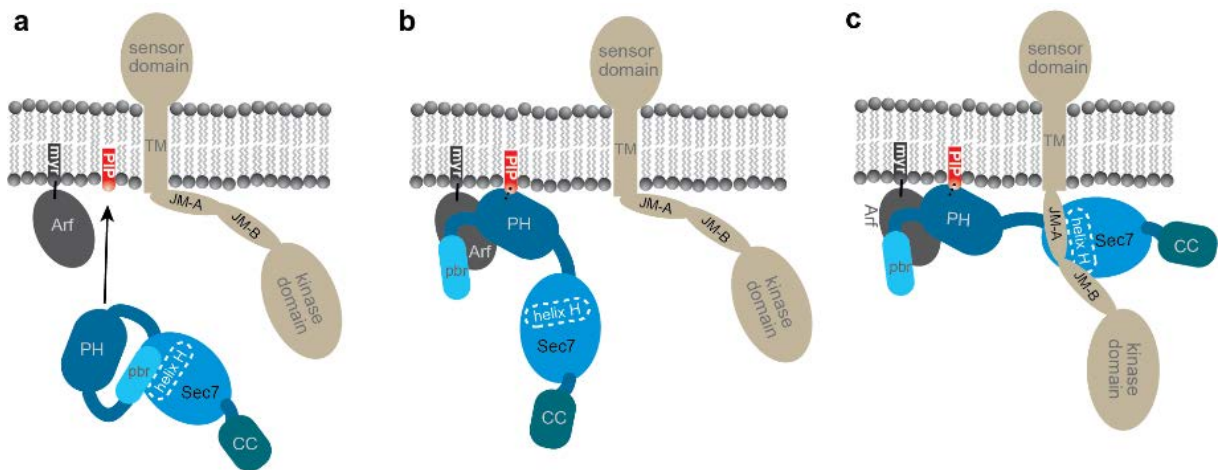


Figure 6.17: related to Fig. 6.2 and Fig. 6.5. **Speculative model of known factors that could promote a potential ARNO-EGFR interaction *in vivo*.** While autoinhibited ARNO does not interact with EGFR-JM (this study), ARNO is recruited to the membrane via an interaction of ARNO-PH and PIP [240] and autoinhibition is reduced via this interaction as well as via interactions of ARNO-PH with membrane located Arf (a,b) [230, 241, 245]. The increased PIP levels found in the proximity of the EGFR [231, 240, 242] could increase co-localization of activated ARNO and EGFR. Previously suggested high linker flexibility in activated ARNO [242] could further facilitate interaction of ARNO-Sec7 with EGFR-JM in a similar manner as found in our *in vitro* studies of the isolated domains.

Bibliography

- [1] Brian K Kobilka. G protein coupled receptor structure and activation. *Biochimica et Biophysica Acta (BBA) - Biomembranes*, 1768(4):794–807, 2007.
- [2] Robert Fredriksson, Malin C Lagerstrom, Lars-Gustav Lundin, and Helgi B Schiøth. The G-protein-coupled receptors in the human genome form five main families. Phylogenetic analysis, paralogon groups, and fingerprints. *Molecular pharmacology*, 63(6):1256–1272, jun 2003.
- [3] A J Venkatakrisnan, Xavier Deupi, Guillaume Lebon, Christopher G Tate, Gebhard F Schertler, and M Madan Babu. Molecular signatures of G-protein-coupled receptors. *Nature*, 494(7436):185–194, feb 2013.
- [4] Andrew L Hopkins and Colin R Groom. The druggable genome., sep 2002.
- [5] Edgar Jacoby, Rochdi Bouhelal, Marc Gerspacher, and Klaus Seuwen. The 7 TM G-protein-coupled receptor target family. *ChemMedChem*, 1(8):761–782, aug 2006.
- [6] Rita Santos, Oleg Ursu, Anna Gaulton, A Patrícia Bento, Ramesh S Donadi, Cristian G Bologna, Anneli Karlsson, Bissan Al-Lazikani, Anne Hersey, Tudor I Oprea, and John P Overington. A comprehensive map of molecular drug targets. *Nature Reviews Drug Discovery*, 16(1):19–34, 2017.
- [7] Clemence Girardet and Andrew A Butler. Neural melanocortin receptors in obesity and related metabolic disorders. *Biochimica et biophysica acta*, 1842(3):482–494, mar 2014.
- [8] K G Mountjoy, M T Mortrud, M J Low, R B Simerly, and R D Cone. Localization of the melanocortin-4 receptor (MC4-R) in neuroendocrine and autonomic control circuits in the brain. *Molecular endocrinology (Baltimore, Md.)*, 8(10):1298–1308, oct 1994.
- [9] W Fan, B A Boston, R A Kesterson, V J Hruby, and R D Cone. Role of melanocortinergic neurons in feeding and the agouti obesity syndrome. *Nature*, 385(6612):165–168, jan 1997.
- [10] D Huszar, C A Lynch, V Fairchild-Huntress, J H Dunmore, Q Fang, L R Berkemeier, W Gu, R A Kesterson, B A Boston, R D Cone, F J Smith, L A Campfield, P Burn, and F Lee. Targeted disruption of the melanocortin-4 receptor results in obesity in mice. *Cell*, 88(1):131–141, jan 1997.
- [11] S.L. Steelman, R.N. Andersen, and R.M. McGregor. A simplified procedure for the preparation of alpha and beta melanocyte-stimulating hormones. *Biochimica et biophysica acta*, 33(1):256–258, may 1959.
- [12] Erica M Haslach, Jay W Schaub, and Carrie Haskell-Luevano. Beta-turn secondary structure and melanocortin ligands. *Bioorganic & medicinal chemistry*, 17(3):952–958, feb 2009.

Bibliography

- [13] U G Sahm, G W Olivier, S K Branch, S H Moss, and C W Pouton. Synthesis and biological evaluation of alpha-MSH analogues substituted with alanine. *Peptides*, 15(7):1297–1302, 1994.
- [14] E E Sugg, W L Cody, Z Abdel-Malek, M E Hadley, and V J Hruby. D-isomeric replacements within the 6-9 core sequence of Ac-[Nle⁴]-alpha-MSH₄₋₁₁-NH₂: a topological model for the solution conformation of alpha-melanotropin. *Biopolymers*, 25(11):2029–2042, nov 1986.
- [15] V J Hruby, B C Wilkes, M E Hadley, F Al-Obeidi, T K Sawyer, D J Staples, A E de Vaux, O Dym, A M Castrucci, and M F Hintz. alpha-Melanotropin: the minimal active sequence in the frog skin bioassay. *Journal of medicinal chemistry*, 30(11):2126–2130, nov 1987.
- [16] K Shizume, A.B. Lerner, and T.B. Fitzpatrick. In vitro bioassay for the melanocyte stimulating hormone. *Endocrinology*, 54(5):553–560, may 1954.
- [17] M.R. Wright and A.B. Lerner. On the movement of pigment granules in frog melanocytes. *Endocrinology*, 66:599–609, apr 1960.
- [18] Baran A Ersoy, Leonardo Pardo, Sumei Zhang, Darren A Thompson, Glenn Millhauser, Cedric Govaerts, and Christian Vaisse. Mechanism of N-terminal modulation of activity at the melanocortin-4 receptor GPCR. *Nature chemical biology*, 8(8):725–730, aug 2012.
- [19] I Sadaf Farooqi, Julia M Keogh, Giles S H Yeo, Emma J Lank, Tim Cheetham, and Stephen O’Rahilly. Clinical spectrum of obesity and mutations in the melanocortin 4 receptor gene. *The New England journal of medicine*, 348(12):1085–1095, mar 2003.
- [20] Ya-Xiong Tao. Constitutive activity in melanocortin-4 receptor: biased signaling of inverse agonists. *Advances in pharmacology (San Diego, Calif.)*, 70:135–154, 2014.
- [21] Kirill Kiselyov, Dong Min Shin, and Shmuel Muallem. Signalling specificity in GPCR-dependent Ca²⁺ signalling. *Cellular signalling*, 15(3):243–253, mar 2003.
- [22] D Lu, D Willard, I R Patel, S Kadwell, L Overton, T Kost, M Luther, W Chen, R P Woychik, and W O Wilkison. Agouti protein is an antagonist of the melanocyte-stimulating-hormone receptor. *Nature*, 371(6500):799–802, oct 1994.
- [23] Katrina A Teare, Richard G Pearson, Kevin M Shakesheff, Geoff Raisman, and John W Haycock. Alpha-MSH inhibits inflammatory signalling in olfactory ensheathing cells. *Neuroreport*, 14(17):2171–2175, dec 2003.
- [24] Juliana Pereira Lopes Gonçalves, Daniel Palmer, and Morten Meldal. MC4R Agonists: Structural Overview on Antiobesity Therapeutics. *Trends in Pharmacological Sciences*, 39(4):402–423, 2018.
- [25] E Lalli and P Sassone-Corsi. Signal transduction and gene regulation: the nuclear response to cAMP. *The Journal of biological chemistry*, 269(26):17359–17362, jul 1994.

-
- [26] Yong-Qi Li, Yogendra Shrestha, Mritunjay Pandey, Min Chen, Ahmed Kablan, Oksana Gavrilova, Stefan Offermanns, and Lee S. Weinstein. Gq/11 α and Gs α mediate distinct physiological responses to central melanocortins. *The Journal of Clinical Investigation*, 126(1):40–49, jan 2016.
- [27] S J Hill, J G Baker, and S Rees. Reporter-gene systems for the study of G-protein-coupled receptors. *Current opinion in pharmacology*, 1(5):526–532, oct 2001.
- [28] Stephen J Hill, Christine Williams, and Lauren T May. Insights into GPCR pharmacology from the measurement of changes in intracellular cyclic AMP; advantages and pitfalls of differing methodologies. *British journal of pharmacology*, 161(6):1266–1275, nov 2010.
- [29] Lenea Nørskov-Lauritsen, Alex Rojas Bie Thomsen, and Hans Bräuner-Osborne. G protein-coupled receptor signaling analysis using homogenous time-resolved Förster resonance energy transfer (HTRF®) technology. *International journal of molecular sciences*, 15(2):2554–2572, feb 2014.
- [30] H Bazin, M Preaudat, E Trinquet, and G Mathis. Homogeneous time resolved fluorescence resonance energy transfer using rare earth cryptates as a tool for probing molecular interactions in biology. *Spectrochimica acta. Part A, Molecular and biomolecular spectroscopy*, 57(11):2197–2211, sep 2001.
- [31] G Mathis. Rare earth cryptates and homogeneous fluoroimmunoassays with human sera. *Clinical chemistry*, 39(9):1953–1959, sep 1993.
- [32] François Degorce, Amy Card, Sharon Soh, Eric Trinquet, Glenn P Knapik, and Bing Xie. HTRF: A technology tailored for drug discovery - a review of theoretical aspects and recent applications. *Current chemical genomics*, 3:22–32, may 2009.
- [33] Dror E Warschawski, Alexandre A Arnold, Maiwenn Beaugrand, Andree Gravel, Etienne Chartrand, and Isabelle Marcotte. Choosing membrane mimetics for NMR structural studies of transmembrane proteins. *Biochimica et biophysica acta*, 1808(8):1957–1974, aug 2011.
- [34] Jonas M Dörr, Stefan Scheidelaar, Martijn C Koorengel, Juan J Dominguez, Marre Schäfer, Cornelis A van Walree, and J Antoinette Killian. The styrene-maleic acid copolymer: a versatile tool in membrane research. *European biophysics journal : EBJ*, 45(1):3–21, jan 2016.
- [35] Jean-Luc Popot. Amphipols, nanodiscs, and fluorinated surfactants: three nonconventional approaches to studying membrane proteins in aqueous solutions. *Annual review of biochemistry*, 79:737–775, 2010.
- [36] Annela M Seddon, Paul Curnow, and Paula J Booth. Membrane proteins, lipids and detergents: not just a soap opera. *Biochimica et biophysica acta*, 1666(1-2):105–117, nov 2004.

- [37] Huan-Xiang Zhou and Timothy A Cross. Influences of membrane mimetic environments on membrane protein structures. *Annual review of biophysics*, 42:361–392, 2013.
- [38] J-L Popot, T Althoff, D Bagnard, J-L Baneres, P Bazzacco, E Billon-Denis, L J Catoire, P Champeil, D Charvolin, M J Cocco, G Cremel, T Dahmane, L M de la Maza, C Ebel, F Gabel, F Giusti, Y Gohon, E Goormaghtigh, E Guittet, J H Kleinschmidt, W Kuhlbrandt, C Le Bon, K L Martinez, M Picard, B Pucci, J N Sachs, C Tribet, C van Heijenoort, F Wien, F Zito, and M Zoonens. Amphipols from A to Z. *Annual review of biophysics*, 40:379–408, 2011.
- [39] Shantha Elter, Thomas Raschle, Sabine Arens, Aldino Viegas, Vladimir Gelev, Manuel Etzkorn, and Gerhard Wagner. The use of amphipols for NMR structural characterization of 7-TM proteins. *The Journal of membrane biology*, 247(9-10):957–964, oct 2014.
- [40] Ulrich H N Durr, Ronald Soong, and Ayyalusamy Ramamoorthy. When detergent meets bilayer: birth and coming of age of lipid bicelles. *Progress in nuclear magnetic resonance spectroscopy*, 69:1–22, feb 2013.
- [41] Regitze R Vold and R.Scott Prosser. Magnetically Oriented Phospholipid Bilayered Micelles for Structural Studies of Polypeptides. Does the Ideal Bicelle Exist? *Journal of Magnetic Resonance, Series B*, 113(3):267–271, 1996.
- [42] K P Howard and S J Opella. High-resolution solid-state NMR spectra of integral membrane proteins reconstituted into magnetically oriented phospholipid bilayers. *Journal of magnetic resonance. Series B*, 112(1):91–94, jul 1996.
- [43] T H Bayburt, J W Carlson, and S G Sligar. Reconstitution and imaging of a membrane protein in a nanometer-size phospholipid bilayer. *Journal of structural biology*, 123(1):37–44, sep 1998.
- [44] Timothy H Bayburt, Yelena V Grinkova, and Stephen G Sligar. Self-Assembly of Discoidal Phospholipid Bilayer Nanoparticles with Membrane Scaffold Proteins. *Nano Letters*, 2(8):853–856, aug 2002.
- [45] Franz Hagn, Manuel Etzkorn, Thomas Raschle, and Gerhard Wagner. Optimized phospholipid bilayer nanodiscs facilitate high-resolution structure determination of membrane proteins. *Journal of the American Chemical Society*, 135(5):1919–1925, feb 2013.
- [46] Timothy J Knowles, Rachael Finka, Corinne Smith, Yu-Pin Lin, Tim Dafforn, and Michael Overduin. Membrane proteins solubilized intact in lipid containing nanoparticles bounded by styrene maleic acid copolymer. *Journal of the American Chemical Society*, 131(22):7484–7485, jun 2009.
- [47] Mohammed Jamshad, Vinciane Grimard, Ilaria Idini, Tim J Knowles, Miriam R Dowle, Naomi Schofield, Pooja Sridhar, Yupin Lin, Rachael Finka, Mark Wheatley, Owen R T

-
- Thomas, Richard E Palmer, Michael Overduin, Cédric Govaerts, Jean-Marie Ruyschaert, Karen J Edler, and Tim R Dafforn. Structural analysis of a nanoparticle containing a lipid bilayer used for detergent-free extraction of membrane proteins. *Nano Research*, 8(3):774–789, 2015.
- [48] Ashley R Long, Catherine C O'Brien, Ketan Malhotra, Christine T Schwall, Arlene D Albert, Anthony Watts, and Nathan N Alder. A detergent-free strategy for the reconstitution of active enzyme complexes from native biological membranes into nanoscale discs. *BMC biotechnology*, 13:41, may 2013.
- [49] Stefan Scheidelaar, Martijn C Koorengevel, Juan Dominguez Pardo, Johannes D Meeldijk, Eefjan Breukink, and J Antoinette Killian. Molecular model for the solubilization of membranes into nanodisks by styrene maleic Acid copolymers. *Biophysical journal*, 108(2):279–290, jan 2015.
- [50] Stefan Scheidelaar, Martijn C Koorengevel, Cornelius A van Walree, Juan J Dominguez, Jonas M Dorr, and J Antoinette Killian. Effect of Polymer Composition and pH on Membrane Solubilization by Styrene-Maleic Acid Copolymers. *Biophysical journal*, 111(9):1974–1986, nov 2016.
- [51] G E Smith, M J Fraser, and M D Summers. Molecular Engineering of the *Autographa californica* Nuclear Polyhedrosis Virus Genome: Deletion Mutations Within the Polyhedrin Gene. *Journal of virology*, 46(2):584–593, may 1983.
- [52] D. C. Kelly. Baculovirus replication. *Journal of General Virology*, 63(1):1–13, nov 1982.
- [53] J L Vaughn, R H Goodwin, G J Tompkins, and P McCawley. The establishment of two cell lines from the insect *Spodoptera frugiperda* (Lepidoptera; Noctuidae). *In vitro*, 13(4):213–217, apr 1977.
- [54] W F Hink. Established insect cell line from the cabbage looper, *Trichoplusia ni*. *Nature*, 226(5244):466–467, may 1970.
- [55] Wouter Bruinzeel, Jeff Yon, Silvio Giovannelli, and Stefan Masure. Recombinant insect cell expression and purification of human beta-secretase (BACE-1) for X-ray crystallography. *Protein expression and purification*, 26(1):139–148, oct 2002.
- [56] Robert R Granados, Guoxun Li, and G W Blissard. Insect cell culture and biotechnology. *Virologica Sinica*, 22(2):83–93, 2007.
- [57] Florian Krammer, Sabine Nakowitsch, Paul Messner, Dieter Palmberger, Boris Ferko, and Reingard Grabherr. Swine-origin pandemic H1N1 influenza virus-like particles produced in insect cells induce hemagglutination inhibiting antibodies in BALB/c mice. *Biotechnology journal*, 5(1):17–23, jan 2010.

- [58] Yoshifumi Hashimoto, Sheng Zhang, and Gary W Blissard. Ao38, a new cell line from eggs of the black witch moth, *Ascalapha odorata* (Lepidoptera: Noctuidae), is permissive for AcMNPV infection and produces high levels of recombinant proteins. *BMC biotechnology*, 10:50, jul 2010.
- [59] Monika Wilde, Miriam Klausberger, Dieter Palmberger, Wolfgang Ernst, and Reingard Grabherr. Tnao38, high five and Sf9—evaluation of host-virus interactions in three different insect cell lines: baculovirus production and recombinant protein expression. *Biotechnology letters*, 36(4):743–749, apr 2014.
- [60] B G Ooi and L K Miller. Regulation of host RNA levels during baculovirus infection. *Virology*, 166(2):515–523, oct 1988.
- [61] J P Burand, M D Summers, and G E Smith. Transfection with baculovirus DNA. *Virology*, 101(1):286–290, feb 1980.
- [62] V A Luckow, S C Lee, G F Barry, and P O Olins. Efficient generation of infectious recombinant baculoviruses by site-specific transposon-mediated insertion of foreign genes into a baculovirus genome propagated in *Escherichia coli*. *Journal of virology*, 67(8):4566–4579, aug 1993.
- [63] Dalibor Milic and Dmitry B Veprintsev. Large-scale production and protein engineering of G protein-coupled receptors for structural studies. *Frontiers in pharmacology*, 6:66, 2015.
- [64] Alexis Elbaz, James H Bower, Demetrius M Maraganore, Shannon K McDonnell, Brett J Peterson, J Eric Ahlskog, Daniel J Schaid, and Walter A Rocca. Risk tables for parkinsonism and Parkinson’s disease. *Journal of clinical epidemiology*, 55(1):25–31, jan 2002.
- [65] J Jankovic. Parkinson’s disease: clinical features and diagnosis. *Journal of neurology, neurosurgery, and psychiatry*, 79(4):368–376, apr 2008.
- [66] Jose A Obeso, Maria Cruz Rodriguez-Oroz, Beatriz Benitez-Temino, Francisco J Blesa, Jorge Guridi, Concepcio Marin, and Manuel Rodriguez. Functional organization of the basal ganglia: therapeutic implications for Parkinson’s disease. *Movement disorders : official journal of the Movement Disorder Society*, 23 Suppl 3:S548–59, 2008.
- [67] Bernd Holdorff. Friedrich Heinrich Lewy (1885-1950) and his work. *Journal of the history of the neurosciences*, 11(1):19–28, mar 2002.
- [68] M G Spillantini, M L Schmidt, V M Lee, J Q Trojanowski, R Jakes, and M Goedert. Alpha-synuclein in Lewy bodies., aug 1997.
- [69] Kelvin C Luk, Victoria Kehm, Jenna Carroll, Bin Zhang, Patrick O’Brien, John Q Trojanowski, and Virginia M-Y Lee. Pathological alpha-synuclein transmission initiates Parkinson-like neurodegeneration in nontransgenic mice. *Science (New York, N.Y.)*, 338(6109):949–953, nov 2012.

-
- [70] Mathias Jucker and Lary C Walker. Self-propagation of pathogenic protein aggregates in neurodegenerative diseases. *Nature*, 501(7465):45–51, sep 2013.
- [71] Marcus D Tuttle, Gemma Comellas, Andrew J Nieuwkoop, Dustin J Covell, Deborah A Berthold, Kathryn D Kloepper, Joseph M Courtney, Jae K Kim, Alexander M Barclay, Amy Kendall, William Wan, Gerald Stubbs, Charles D Schwieters, Virginia M Y Lee, Julia M George, and Chad M Rienstra. Solid-state NMR structure of a pathogenic fibril of full-length human alpha-synuclein. *Nature structural & molecular biology*, 23(5):409–415, may 2016.
- [72] Sara M Butterfield and Hilal A Lashuel. Amyloidogenic protein-membrane interactions: mechanistic insight from model systems. *Angewandte Chemie (International ed. in English)*, 49(33):5628–5654, aug 2010.
- [73] Pavan K Auluck, Gabriela Caraveo, and Susan Lindquist. α -Synuclein: Membrane Interactions and Toxicity in Parkinson’s Disease. *Annual Review of Cell and Developmental Biology*, 26(1):211–233, oct 2010.
- [74] Serena Bellani, Vitor L Sousa, Giuseppe Ronzitti, Flavia Valtorta, Jacopo Meldolesi, and Evelina Chiergatti. The regulation of synaptic function by alpha-synuclein. *Communicative & integrative biology*, 3(2):106–109, mar 2010.
- [75] Aaron D Gitler, Brooke J Bevis, James Shorter, Katherine E Strathearn, Shusei Hamamichi, Linhui Julie Su, Kim A Caldwell, Guy A Caldwell, Jean-Christophe Rochet, J Michael McCaffery, Charles Barlowe, and Susan Lindquist. The Parkinson’s disease protein alpha-synuclein disrupts cellular Rab homeostasis. *Proceedings of the National Academy of Sciences of the United States of America*, 105(1):145–150, jan 2008.
- [76] Nancy M Bonini and Benoit I Giasson. Snaring the function of alpha-synuclein. *Cell*, 123(3):359–361, nov 2005.
- [77] Santiago Esteban-Martín, Jordi Silvestre-Ryan, Carlos W Bertoncini, and Xavier Salvatella. Identification of fibril-like tertiary contacts in soluble monomeric α -synuclein. *Biophysical journal*, 105(5):1192–1198, sep 2013.
- [78] L Stefanis, K E Larsen, H J Rideout, D Sulzer, and L A Greene. Expression of A53T mutant but not wild-type alpha-synuclein in PC12 cells induces alterations of the ubiquitin-dependent degradation system, loss of dopamine release, and autophagic cell death. *The Journal of neuroscience : the official journal of the Society for Neuroscience*, 21(24):9549–9560, dec 2001.
- [79] W S Davidson, A Jonas, D F Clayton, and J M George. Stabilization of alpha-synuclein secondary structure upon binding to synthetic membranes. *The Journal of biological chemistry*, 273(16):9443–9449, apr 1998.

Bibliography

- [80] Tobias S Ulmer, Ad Bax, Nelson B Cole, and Robert L Nussbaum. Structure and dynamics of micelle-bound human alpha-synuclein. *The Journal of biological chemistry*, 280(10):9595–9603, mar 2005.
- [81] Min Zhu, Jie Li, and Anthony L Fink. The association of alpha-synuclein with membranes affects bilayer structure, stability, and fibril formation. *The Journal of biological chemistry*, 278(41):40186–40197, oct 2003.
- [82] Igor Dikiy and David Eliezer. Folding and misfolding of alpha-synuclein on membranes. *Biochimica et biophysica acta*, 1818(4):1013–1018, apr 2012.
- [83] Thibault Viennet, Michael M Wordehoff, Boran Uluca, Chetan Poojari, Hamed Shaykhalishahi, Dieter Willbold, Birgit Strodel, Henrike Heise, Alexander K Buell, Wolfgang Hoyer, and Manuel Etzkorn. Structural insights from lipid-bilayer nanodiscs link alpha-Synuclein membrane-binding modes to amyloid fibril formation. *Communications biology*, 1:44, 2018.
- [84] Naoko Mizuno, Jobin Varkey, Natalie C Kegulian, Balachandra G Hegde, Naiqian Cheng, Ralf Langen, and Alasdair C Steven. Remodeling of lipid vesicles into cylindrical micelles by alpha-synuclein in an extended alpha-helical conformation. *The Journal of biological chemistry*, 287(35):29301–29311, aug 2012.
- [85] Jobin Varkey, Naoko Mizuno, Balachandra G Hegde, Naiqian Cheng, Alasdair C Steven, and Ralf Langen. alpha-Synuclein oligomers with broken helical conformation form lipoprotein nanoparticles. *The Journal of biological chemistry*, 288(24):17620–17630, jun 2013.
- [86] Cedric Eichmann, Silvia Campioni, Julia Kowal, Innokentiy Maslennikov, Juan Gerez, Xiaoxia Liu, Joeri Verasdonck, Nadezhda Nespoitaya, Senyon Choe, Beat H Meier, Paola Picotti, Josep Rizo, Henning Stahlberg, and Roland Riek. Preparation and Characterization of Stable alpha-Synuclein Lipoprotein Particles. *The Journal of biological chemistry*, 291(16):8516–8527, apr 2016.
- [87] Cedric Eichmann, Pratibha Kumari, and Roland Riek. High-density lipoprotein-like particle formation of Synuclein variants., jan 2017.
- [88] Vitali I Stsiapura, Alexander A Maskevich, Valery A Kuzmitsky, Konstantin K Turoverov, and Irina M Kuznetsova. Computational study of thioflavin T torsional relaxation in the excited state. *The journal of physical chemistry. A*, 111(22):4829–4835, jun 2007.
- [89] T Hunter, N Ling, and J A Cooper. Protein kinase C phosphorylation of the EGF receptor at a threonine residue close to the cytoplasmic face of the plasma membrane. *Nature*, 311(5985):480–483, oct 1984.

-
- [90] P Morrison, K Takishima, and M R Rosner. Role of threonine residues in regulation of the epidermal growth factor receptor by protein kinase C and mitogen-activated protein kinase. *The Journal of biological chemistry*, 268(21):15536–15543, jul 1993.
- [91] Monica Red Brewer, Sung Hee Choi, Diego Alvarado, Katarina Moravcevic, Ambra Pozzi, Mark A Lemmon, and Graham Carpenter. The juxtamembrane region of the EGF receptor functions as an activation domain. *Molecular cell*, 34(6):641–651, jun 2009.
- [92] H M Poppleton, G J Wiepz, P J Bertics, and T B Patel. Modulation of the protein tyrosine kinase activity and autophosphorylation of the epidermal growth factor receptor by its juxtamembrane region. *Archives of biochemistry and biophysics*, 363(2):227–236, mar 1999.
- [93] Sami Aifa, Knut Johansen, Ulrika K Nilsson, Bo Liedberg, Ingemar Lundstrom, and Samuel P S Svensson. Interactions between the juxtamembrane domain of the EGFR and calmodulin measured by surface plasmon resonance. *Cellular signalling*, 14(12):1005–1013, dec 2002.
- [94] J Martin-Nieto and A Villalobo. The human epidermal growth factor receptor contains a juxtamembrane calmodulin-binding site. *Biochemistry*, 37(1):227–236, jan 1998.
- [95] Hongbing Li, Svetlana Panina, Amandeep Kaur, Maria J Ruano, Pablo Sanchez-Gonzalez, Jonas M la Cour, Alexander Stephan, Uffe H Olesen, Martin W Berchtold, and Antonio Villalobo. Regulation of the ligand-dependent activation of the epidermal growth factor receptor by calmodulin. *The Journal of biological chemistry*, 287(5):3273–3281, jan 2012.
- [96] Stuart McLaughlin, Steven O Smith, Michael J Hayman, and Diana Murray. An electrostatic engine model for autoinhibition and activation of the epidermal growth factor receptor (EGFR/ErbB) family. *The Journal of general physiology*, 126(1):41–53, jul 2005.
- [97] E Wallin and G von Heijne. Genome-wide analysis of integral membrane proteins from eubacterial, archaean, and eukaryotic organisms. *Protein science : a publication of the Protein Society*, 7(4):1029–1038, apr 1998.
- [98] Philip Thomas and Trevor G Smart. HEK293 cell line: a vehicle for the expression of recombinant proteins. *Journal of pharmacological and toxicological methods*, 51(3):187–200, 2005.
- [99] Ganesh P Subedi, Roy W Johnson, Heather A Moniz, Kelley W Moremen, and Adam Barb. High Yield Expression of Recombinant Human Proteins with the Transient Transfection of HEK293 Cells in Suspension. *Journal of Visualized Experiments*, 106:e53568, dec 2015.
- [100] Tuulia Saarenpaa, Veli-Pekka Jaakola, and Adrian Goldman. Baculovirus-mediated expression of GPCRs in insect cells. *Methods in enzymology*, 556:185–218, 2015.

Bibliography

- [101] Edward A McKenzie and W Mark Abbott. Expression of recombinant proteins in insect and mammalian cells. *Methods (San Diego, Calif.)*, 147:40–49, sep 2018.
- [102] M le Maire, P Champeil, and J V Moller. Interaction of membrane proteins and lipids with solubilizing detergents. *Biochimica et biophysica acta*, 1508(1-2):86–111, nov 2000.
- [103] Daniel N Wiseman, Abigail Otchere, Jaimin H Patel, Romeez Uddin, Naomi L Pollock, Sarah J Routledge, Alice J Rothnie, Cathy Slack, David R Poyner, Roslyn M Bill, and Alan D Goddard. Expression and purification of recombinant G protein-coupled receptors: A review. *Protein Expression and Purification*, 167:105524, 2020.
- [104] Joseph A Lyons, Azadeh Shahsavari, Peter Aasted Paulsen, Bjorn Panyella Pedersen, and Poul Nissen. Expression strategies for structural studies of eukaryotic membrane proteins. *Current opinion in structural biology*, 38:137–144, jun 2016.
- [105] Naomi L Pollock, Sarah C Lee, Jaimin H Patel, Aiman A Gulamhussein, and Alice J Rothnie. Structure and function of membrane proteins encapsulated in a polymer-bound lipid bilayer. *Biochimica et biophysica acta. Biomembranes*, 1860(4):809–817, apr 2018.
- [106] Kailene S Simon, Naomi L Pollock, and Sarah C Lee. Membrane protein nanoparticles: the shape of things to come. *Biochemical Society transactions*, 46(6):1495–1504, dec 2018.
- [107] Sarah C Lee and Naomi L Pollock. Membrane proteins: is the future disc shaped? *Biochemical Society transactions*, 44(4):1011–1018, aug 2016.
- [108] Mark Wheatley, Jack Charlton, Mohammed Jamshad, Sarah J Routledge, Sian Bailey, Penelope J La-Borde, Maria T Azam, Richard T Logan, Roslyn M Bill, Tim R Dafforn, and David R Poyner. GPCR-styrene maleic acid lipid particles (GPCR-SMALPs): their nature and potential. *Biochemical Society transactions*, 44(2):619–623, apr 2016.
- [109] V R Lingappa, F N Katz, H F Lodish, and G Blobel. A signal sequence for the insertion of a transmembrane glycoprotein. Similarities to the signals of secretory proteins in primary structure and function. *The Journal of biological chemistry*, 253(24):8667–8670, dec 1978.
- [110] Supriya Srinivasan, Cecile Lubrano-Berthelier, Cedric Govaerts, Franck Picard, Pamela Santiago, Bruce R Conklin, and Christian Vaisse. Constitutive activity of the melanocortin-4 receptor is maintained by its N-terminal domain and plays a role in energy homeostasis in humans. *The Journal of clinical investigation*, 114(8):1158–1164, oct 2004.
- [111] Barbara J Kelly, Linda A King, and Robert D Possee. Introduction to baculovirus molecular biology. *Methods in molecular biology (Clifton, N.J.)*, 388:25–54, 2007.

-
- [112] K B Seamon, W Padgett, and J W Daly. Forskolin: unique diterpene activator of adenylylate cyclase in membranes and in intact cells. *Proceedings of the National Academy of Sciences*, 78(6):3363 LP – 3367, jun 1981.
- [113] S Nakanishi, A Inoue, T Kita, M Nakamura, A C Chang, S N Cohen, and S Numa. Nucleotide sequence of cloned cDNA for bovine corticotropin-beta-lipotropin precursor. *Nature*, 278(5703):423–427, mar 1979.
- [114] Nicolas Heyder, Gunnar Kleinau, Michal Szczepek, Dennis Kwiatkowski, David Speck, Lucia Soletto, Jose Miguel Cerda-Reverter, Heiko Krude, Peter Kuhnen, Heike Biebermann, and Patrick Scheerer. Signal Transduction and Pathogenic Modifications at the Melanocortin-4 Receptor: A Structural Perspective. *Frontiers in endocrinology*, 10:515, 2019.
- [115] S G Blanchard, C O Harris, O R Ittoop, J S Nichols, D J Parks, A T Truesdale, and W O Wilkison. Agouti antagonism of melanocortin binding and action in the B16F10 murine melanoma cell line. *Biochemistry*, 34(33):10406–10411, aug 1995.
- [116] T M Fong, C Mao, T MacNeil, R Kalyani, T Smith, D Weinberg, M R Tota, and L H Van der Ploeg. ART (protein product of agouti-related transcript) as an antagonist of MC-3 and MC-4 receptors. *Biochemical and biophysical research communications*, 237(3):629–631, aug 1997.
- [117] M M Ollmann, B D Wilson, Y K Yang, J A Kerns, Y Chen, I Gantz, and G S Barsh. Antagonism of central melanocortin receptors in vitro and in vivo by agouti-related protein. *Science (New York, N.Y.)*, 278(5335):135–138, oct 1997.
- [118] Li Guo, Heike Munzberg, Ronald C Stuart, Eduardo A Nillni, and Christian Bjorbaek. N-acetylation of hypothalamic alpha-melanocyte-stimulating hormone and regulation by leptin. *Proceedings of the National Academy of Sciences of the United States of America*, 101(32):11797–11802, aug 2004.
- [119] Shubh Sharma, Alastair S Garfield, Bhavik Shah, Patrick Kleyn, Iliia Ichetovkin, Ida Hatoum Moeller, William R Mowrey, and Lex H T Van der Ploeg. Current Mechanistic and Pharmacodynamic Understanding of Melanocortin-4 Receptor Activation. *Molecules (Basel, Switzerland)*, 24(10), may 2019.
- [120] T K Sawyer, P J Sanfilippo, V J Hruby, M H Engel, C B Heward, J B Burnett, and M E Hadley. 4-Norleucine, 7-D-phenylalanine-alpha-melanocyte-stimulating hormone: a highly potent alpha-melanotropin with ultralong biological activity. *Proceedings of the National Academy of Sciences of the United States of America*, 77(10):5754–5758, oct 1980.
- [121] V J Hruby, D Lu, S D Sharma, A L Castrucci, R A Kesterson, F A Al-Obeidi, M E Hadley, and R D Cone. Cyclic lactam alpha-melanotropin analogues of Ac-Nle4-cyclo[Asp5,

- D-Phe⁷,Lys¹⁰] alpha-melanocyte-stimulating hormone-(4-10)-NH₂ with bulky aromatic amino acids at position 7 show high antagonist potency and selectivity at specific melanocortin receptors. *Journal of medicinal chemistry*, 38(18):3454–3461, sep 1995.
- [122] H B Schioth, R Muceniece, F Mutulis, A A Bouifrouri, I Mutule, and J E Wikberg. Further pharmacological characterization of the selective melanocortin 4 receptor antagonist HS014: comparison with SHU9119. *Neuropeptides*, 33(3):191–196, jun 1999.
- [123] Thomas A Kost, J Patrick Condreay, and Donald L Jarvis. Baculovirus as versatile vectors for protein expression in insect and mammalian cells. *Nature biotechnology*, 23(5):567–575, may 2005.
- [124] V Sarramegn, I Muller, A Milon, and F Talmont. Recombinant G protein-coupled receptors from expression to renaturation: a challenge towards structure. *Cellular and molecular life sciences : CMLS*, 63(10):1149–1164, may 2006.
- [125] J M Neugebauer. Detergents: an overview. *Methods in enzymology*, 182:239–253, 1990.
- [126] Steven E Bane, Javier E Velasquez, and Anne Skaja Robinson. Expression and purification of milligram levels of inactive G-protein coupled receptors in *E. coli*. *Protein expression and purification*, 52(2):348–355, apr 2007.
- [127] Said Eshaghi, Marie Hedren, Marina Ignatushchenko Abdel Nasser, Tove Hammarberg, Anders Thornell, and Par Nordlund. An efficient strategy for high-throughput expression screening of recombinant integral membrane proteins. *Protein science : a publication of the Protein Society*, 14(3):676–683, mar 2005.
- [128] Sonali Gulati, Mohammed Jamshad, Timothy J Knowles, Kerrie A Morrison, Rebecca Downing, Natasha Cant, Richard Collins, Jan B Koenderink, Robert C Ford, Michael Overduin, Ian D Kerr, Timothy R Dafforn, and Alice J Rothnie. Detergent-free purification of ABC (ATP-binding-cassette) transporters. *The Biochemical journal*, 461(2):269–278, jul 2014.
- [129] David J K Swainsbury, Stefan Scheidelaar, Rienk van Grondelle, J Antoinette Killian, and Michael R Jones. Bacterial reaction centers purified with styrene maleic acid copolymer retain native membrane functional properties and display enhanced stability. *Angewandte Chemie (International ed. in English)*, 53(44):11803–11807, oct 2014.
- [130] Jonas M Dorr, Martijn C Koorengel, Marre Schafer, Alexander V Prokofyev, Stefan Scheidelaar, Elwin A W van der Crujisen, Timothy R Dafforn, Marc Baldus, and J Antoinette Killian. Detergent-free isolation, characterization, and functional reconstitution of a tetrameric K⁺ channel: the power of native nanodiscs. *Proceedings of the National Academy of Sciences of the United States of America*, 111(52):18607–18612, dec 2014.
- [131] Sarah C Lee, Tim J Knowles, Vincent L G Postis, Mohammed Jamshad, Rosemary A Parslow, Yu-Pin Lin, Adrian Goldman, Pooja Sridhar, Michael Overduin, Stephen P

-
- Muench, and Timothy R Dafforn. A method for detergent-free isolation of membrane proteins in their local lipid environment. *Nature protocols*, 11(7):1149–1162, jul 2016.
- [132] Xiaoqiang Wang, Karolina Corin, Cyrus Rich, and Shuguang Zhang. Study of two G-protein coupled receptor variants of human trace amine-associated receptor 5. *Scientific reports*, 1:102, 2011.
- [133] David Drew, Mirjam Lerch, Edmund Kunji, Dirk-Jan Slotboom, and Jan-Willem de Gier. Optimization of membrane protein overexpression and purification using GFP fusions. *Nature methods*, 3(4):303–313, apr 2006.
- [134] Philip J Reeves, Jong-Myoung Kim, and H Gobind Khorana. Structure and function in rhodopsin: a tetracycline-inducible system in stable mammalian cell lines for high-level expression of opsin mutants. *Proceedings of the National Academy of Sciences of the United States of America*, 99(21):13413–13418, oct 2002.
- [135] Brian L Cook, Karin E Ernberg, Hyeyoun Chung, and Shuguang Zhang. Study of a synthetic human olfactory receptor 17-4: expression and purification from an inducible mammalian cell line. *PloS one*, 3(8):e2920, aug 2008.
- [136] E Nekrasova, A Sosinskaya, M Natochin, D Lancet, and U Gat. Overexpression, solubilization and purification of rat and human olfactory receptors. *European journal of biochemistry*, 238(1):28–37, may 1996.
- [137] H Biebermann, H Krude, A Elsner, V Chubanov, T Gudermann, and A Gruters. Autosomal-dominant mode of inheritance of a melanocortin-4 receptor mutation in a patient with severe early-onset obesity is due to a dominant-negative effect caused by receptor dimerization. *Diabetes*, 52:2984–2988, 2003.
- [138] A Elsner, P Tarnow, M Schaefer, P Ambrugger, H Krude, A Gruters, and H Biebermann. MC4R oligomerizes independently of extracellular cysteine residues. *Peptides*, 27:372–379, 2006.
- [139] A Levoye, J Dam, M A Ayoub, J L Guillaume, C Couturier, P Delagrangé, and R Jockers. The orphan GPR50 receptor specifically inhibits MT1 melatonin receptor function through heterodimerization. *EMBO Journal*, 25:3012–3023, 2006.
- [140] Ioanna Mosialou, Steven Shikhel, Jian-Min Liu, Antonio Maurizi, Na Luo, Zhenyan He, Yiru Huang, Haihong Zong, Richard A Friedman, Jonathan Barasch, Patricia Lanzano, Liyong Deng, Rudolph L Leibel, Mishaela Rubin, Thomas Nickolas, Wendy Chung, Lori M Zeltser, Kevin W Williams, Jeffrey E Pessin, and Stavroula Kousteni. MC4R-dependent suppression of appetite by bone-derived lipocalin 2. *Nature*, 543(7645):385–390, mar 2017.
- [141] Monzur Murshed. Mechanism of Bone Mineralization. *Cold Spring Harbor perspectives in medicine*, 8(12), dec 2018.

Bibliography

- [142] Isabelle Legroux-Gerot, Jean Vignau, Francis Collier, and Bernard Cortet. Bone loss associated with anorexia nervosa. *Joint bone spine*, 72(6):489–495, dec 2005.
- [143] Madhusmita Misra and Anne Klibanski. The neuroendocrine basis of anorexia nervosa and its impact on bone metabolism. *Neuroendocrinology*, 93(2):65–73, 2011.
- [144] P Ducy, M Amling, S Takeda, M Priemel, A F Schilling, F T Beil, J Shen, C Vinson, J M Rueger, and G Karsenty. Leptin inhibits bone formation through a hypothalamic relay: a central control of bone mass. *Cell*, 100(2):197–207, jan 2000.
- [145] Keertik Fulzele, Ryan C Riddle, Douglas J DiGirolamo, Xuemei Cao, Chao Wan, Dongquan Chen, Marie-Claude Faugere, Susan Aja, Mehboob A Hussain, Jens C Bruning, and Thomas L Clemens. Insulin receptor signaling in osteoblasts regulates postnatal bone acquisition and body composition. *Cell*, 142(2):309–319, jul 2010.
- [146] Daisuke Kajimura, Ha Won Lee, Kyle J Riley, Emilio Arteaga-Solis, Mathieu Ferron, Bin Zhou, Christopher J Clarke, Yusuf A Hannun, Ronald A DePinho, X Edward Guo, J John Mann, and Gerard Karsenty. Adiponectin regulates bone mass via opposite central and peripheral mechanisms through FoxO1. *Cell metabolism*, 17(6):901–915, jun 2013.
- [147] Harry Horsnell and Paul A Baldock. Osteoblastic Actions of the Neuropeptide Y System to Regulate Bone and Energy Homeostasis. *Current osteoporosis reports*, 14(1):26–31, feb 2016.
- [148] Jianwen Wei, Timothy Hanna, Nina Suda, Gerard Karsenty, and Patricia Ducy. Osteocalcin Promotes β -Cell Proliferation During Development and Adulthood Through Gprc6a. *Diabetes*, 63(3):1021–1031, 2014.
- [149] Jae Geun Kim, Ben-Hua Sun, Marcelo O Dietrich, Marco Koch, Gang-Qing Yao, Sabrina Diano, Karl Insogna, and Tamas L Horvath. AgRP Neurons Regulate Bone Mass. *Cell reports*, 13(1):8–14, oct 2015.
- [150] Na Kyung Lee, Hideaki Sowa, Eiichi Hinoi, Mathieu Ferron, Jong Deok Ahn, Cyrille Confavreux, Romain Dacquin, Patrick J Mee, Marc D McKee, Dae Young Jung, Zhiyou Zhang, Jason K Kim, Franck Mauvais-Jarvis, Patricia Ducy, and Gerard Karsenty. Endocrine regulation of energy metabolism by the skeleton. *Cell*, 130(3):456–469, aug 2007.
- [151] Mathieu Ferron, Jianwen Wei, Tatsuya Yoshizawa, Andrea Del Fattore, Ronald A DePinho, Anna Teti, Patricia Ducy, and Gerard Karsenty. Insulin signaling in osteoblasts integrates bone remodeling and energy metabolism. *Cell*, 142(2):296–308, jul 2010.
- [152] Marie-Therese Rached, Aruna Kode, Barbara C Silva, Dae Young Jung, Susan Gray, Helena Ong, Ji-Hye Paik, Ronald A DePinho, Jason K Kim, Gerard Karsenty, and Stavroula Kousteni. FoxO1 expression in osteoblasts regulates glucose homeostasis through regulation of osteocalcin in mice. *The Journal of clinical investigation*, 120(1):357–368, jan 2010.

-
- [153] Shiguang Liu, Rong Guo, Leigh G Simpson, Zhou-Sheng Xiao, Charles E Burnham, and L Darryl Quarles. Regulation of fibroblastic growth factor 23 expression but not degradation by PHEX. *The Journal of biological chemistry*, 278(39):37419–37426, sep 2003.
- [154] Nisan Bhattacharyya, William H Chong, Rachel I Gafni, and Michael T Collins. Fibroblast growth factor 23: state of the field and future directions. *Trends in endocrinology and metabolism: TEM*, 23(12):610–618, dec 2012.
- [155] L Kjeldsen, A H Johnsen, H Sengelov, and N Borregaard. Isolation and primary structure of NGAL, a novel protein associated with human neutrophil gelatinase. *The Journal of biological chemistry*, 268(14):10425–10432, may 1993.
- [156] D R Flower. The lipocalin protein family: structure and function. *The Biochemical journal*, 318 (Pt 1:1–14, aug 1996.
- [157] L Kjeldsen, J B Cowland, and N Borregaard. Human neutrophil gelatinase-associated lipocalin and homologous proteins in rat and mouse. *Biochimica et biophysica acta*, 1482(1-2):272–283, oct 2000.
- [158] David H Goetz, Margaret A Holmes, Niels Borregaard, Martin E Bluhm, Kenneth N Raymond, and Roland K Strong. The neutrophil lipocalin NGAL is a bacteriostatic agent that interferes with siderophore-mediated iron acquisition. *Molecular cell*, 10(5):1033–1043, nov 2002.
- [159] Michael A Bachman, Virginia L Miller, and Jeffrey N Weiser. Mucosal lipocalin 2 has pro-inflammatory and iron-sequestering effects in response to bacterial enterobactin. *PLoS pathogens*, 5(10):e1000622, oct 2009.
- [160] Xuewu Zhang, Jodi Gureasko, Kui Shen, Philip A Cole, and John Kuriyan. An allosteric mechanism for activation of the kinase domain of epidermal growth factor receptor. *Cell*, 125(6):1137–1149, jun 2006.
- [161] M Coles, T Diercks, B Muehlenweg, S Bartsch, V Zolzer, H Tschesche, and H Kessler. The solution structure and dynamics of human neutrophil gelatinase-associated lipocalin. *Journal of molecular biology*, 289(1):139–157, may 1999.
- [162] S T Chu, H J Lin, H L Huang, and Y H Chen. The hydrophobic pocket of 24p3 protein from mouse uterine luminal fluid: fatty acid and retinol binding activity and predicted structural similarity to lipocalins. *The journal of peptide research : official journal of the American Peptide Society*, 52(5):390–397, nov 1998.
- [163] T Bratt, S Ohlson, and N Borregaard. Interactions between neutrophil gelatinase-associated lipocalin and natural lipophilic ligands. *Biochimica et biophysica acta*, 1472(1-2):262–269, oct 1999.

Bibliography

- [164] J. G. Marblestone. Comparison of SUMO fusion technology with traditional gene fusion systems: Enhanced expression and solubility with SUMO. *Protein Science*, 15(1):182–189, 2006.
- [165] J B Cowland and N Borregaard. Molecular characterization and pattern of tissue expression of the gene for neutrophil gelatinase-associated lipocalin from humans. *Genomics*, 45(1):17–23, oct 1997.
- [166] Susanne Triebel, Jörg Bläser, Heinz Reinke, and Harald Tschesche. A 25 kDa α 2-microglobulin-related protein is a component of the 125 kDa form of human gelatinase. *FEBS Letters*, 314(3):386–388, 1992.
- [167] L Yan, N Borregaard, L Kjeldsen, and M A Moses. The high molecular weight urinary matrix metalloproteinase (MMP) activity is a complex of gelatinase B/MMP-9 and neutrophil gelatinase-associated lipocalin (NGAL). Modulation of MMP-9 activity by NGAL. *The Journal of biological chemistry*, 276(40):37258–37265, oct 2001.
- [168] Pia Klausen, Carsten U Niemann, Jack B Cowland, Karen Krabbe, and Niels Borregaard. On mouse and man: neutrophil gelatinase associated lipocalin is not involved in apoptosis or acute response. *European journal of haematology*, 75(4):332–340, oct 2005.
- [169] Javier Mestas and Christopher C W Hughes. Of mice and not men: differences between mouse and human immunology. *Journal of immunology (Baltimore, Md. : 1950)*, 172(5):2731–2738, mar 2004.
- [170] Ana-Isabel Cabedo Martinez, Katharina Weinhäupl, Wing-Kee Lee, Natascha A Wolff, Barbara Storch, Szymon Żerko, Robert Konrat, Wiktor Koźmiński, Kathrin Breuker, Frank Thévenod, and Nicolas Coudevylle. Biochemical and Structural Characterization of the Interaction between the Siderocalin NGAL/LCN2 (Neutrophil Gelatinase-associated Lipocalin/Lipocalin 2) and the N-terminal Domain of Its Endocytic Receptor SLC22A17. *Journal of Biological Chemistry*, 291(6):2917–2930, feb 2016.
- [171] Jillian G Baker, Ian P Hall, and Stephen J Hill. Agonist and inverse agonist actions of beta-blockers at the human beta 2-adrenoceptor provide evidence for agonist-directed signaling. *Molecular pharmacology*, 64(6):1357–1369, dec 2003.
- [172] I Gantz, H Miwa, Y Konda, Y Shimoto, T Tashiro, S J Watson, J DelValle, and T Yamada. Molecular cloning, expression, and gene localization of a fourth melanocortin receptor. *The Journal of biological chemistry*, 268(20):15174–15179, jul 1993.
- [173] Aurawan Vongs, Nicole M Lynn, and Charles I Rosenblum. Activation of MAP kinase by MC4-R through PI3 kinase. *Regulatory peptides*, 120(1-3):113–118, aug 2004.
- [174] Peter Metzger, Bradley Carlson, Hui Sun, Zhenzhong Cui, Oksana Gavrilova, Min Chen, and Lee Weinstein. OR12-3 Mice with MC4R Site Mutation (F51L) Develop Severe Obe-

-
- sity Independent of Gs-alpha/cAMP Signaling. *Journal of the Endocrine Society*, 3(Supplement_1), apr 2019.
- [175] Yong-Qi Li, Yogendra Shrestha, Mritunjay Pandey, Min Chen, Ahmed Kablan, Oksana Gavrilova, Stefan Offermanns, and Lee S Weinstein. G(q/11) α and G(s) α mediate distinct physiological responses to central melanocortins. *The Journal of clinical investigation*, 126(1):40–49, jan 2016.
- [176] Xudong Feng, Dongxian Guan, Thomas Auen, Jae Won Choi, Mario Andres Salazar-Hernandez, Farhana Faruk, Kyle D Copps, and Umut Ozcan. Lipocalin 2 Does Not Play A Role in Celastrol-Mediated Reduction in Food Intake and Body Weight. *Scientific reports*, 9(1):12809, sep 2019.
- [177] Junli Liu, Jaemin Lee, Mario Andres Salazar Hernandez, Ralph Mazitschek, and Umut Ozcan. Treatment of obesity with celastrol. *Cell*, 161(5):999–1011, may 2015.
- [178] Michael Overduin and Bert Klumperman. Advancing membrane biology with poly(styrene-co-maleic acid)-based native nanodiscs. *European Polymer Journal*, 110:63–68, 2019.
- [179] S R Tonge and B J Tighe. Responsive hydrophobically associating polymers: a review of structure and properties. *Advanced drug delivery reviews*, 53(1):109–122, dec 2001.
- [180] Rongfu Zhang, Indra D Sahu, Lishan Liu, Anna Osatuke, Raven G Comer, Carole Dabney-Smith, and Gary A Lorigan. Characterizing the structure of lipodisc nanoparticles for membrane protein spectroscopic studies. *Biochimica et biophysica acta*, 1848(1 Pt B):329–333, jan 2015.
- [181] Paolo Arosio, Thomas Müller, Luke Rajah, Emma V Yates, Francesco A Aprile, Yingbo Zhang, Samuel I A Cohen, Duncan A White, Therese W Herling, Erwin J De Genst, Sara Linse, Michele Vendruscolo, Christopher M Dobson, and Tuomas P J Knowles. Microfluidic Diffusion Analysis of the Sizes and Interactions of Proteins under Native Solution Conditions. *ACS Nano*, 10(1):333–341, jan 2016.
- [182] Emma V Yates, Thomas Muller, Luke Rajah, Erwin J De Genst, Paolo Arosio, Sara Linse, Michele Vendruscolo, Christopher M Dobson, and Tuomas P J Knowles. Latent analysis of unmodified biomolecules and their complexes in solution with attomole detection sensitivity. *Nature chemistry*, 7(10):802–809, oct 2015.
- [183] J Arnaud, O Nobili, and J Boyer. Does the neurotropic action of adrenocorticotrophic hormone involve a lipolytic step? *Biochimica et biophysica acta*, 665(2):244–249, aug 1981.
- [184] Lise Giehm and Daniel E Otzen. Strategies to increase the reproducibility of protein fibrillization in plate reader assays. *Analytical biochemistry*, 400(2):270–281, may 2010.

Bibliography

- [185] Michael M Wordehoff and Wolfgang Hoyer. alpha-Synuclein Aggregation Monitored by Thioflavin T Fluorescence Assay. *Bio-protocol*, 8(14), jul 2018.
- [186] Volodymyr V Shvadchak, Mireille M A E Claessens, and Vinod Subramaniam. Fibril breaking accelerates alpha-synuclein fibrillization. *The journal of physical chemistry. B*, 119(5):1912–1918, feb 2015.
- [187] Silvia Campioni, Guillaume Carret, Sophia Jordens, Lucrece Nicoud, Raffaele Mezzenga, and Roland Riek. The presence of an air-water interface affects formation and elongation of alpha-Synuclein fibrils. *Journal of the American Chemical Society*, 136(7):2866–2875, feb 2014.
- [188] Jeremy Pronchik, Xianglan He, Jason T Giurleo, and David S Talaga. In vitro formation of amyloid from alpha-synuclein is dominated by reactions at hydrophobic interfaces. *Journal of the American Chemical Society*, 132(28):9797–9803, jul 2010.
- [189] Erik Chorell, Emma Andersson, Margery L Evans, Neha Jain, Anna Gotheson, Jorgen Aden, Matthew R Chapman, Fredrik Almqvist, and Pernilla Wittung-Stafshede. Bacterial Chaperones CsgE and CsgC Differentially Modulate Human alpha-Synuclein Amyloid Formation via Transient Contacts. *PloS one*, 10(10):e0140194, 2015.
- [190] Chunjuan Huang, Han Cheng, Shufeng Hao, Hui Zhou, Xujia Zhang, Jianen Gao, Qi-Hong Sun, Hongyu Hu, and Chih-Chen Wang. Heat shock protein 70 inhibits alpha-synuclein fibril formation via interactions with diverse intermediates. *Journal of molecular biology*, 364(3):323–336, dec 2006.
- [191] Michael M Wordehoff, Hamed Shaykhalishahi, Luca Gross, Lothar Gremer, Matthias Stoldt, Alexander K Buell, Dieter Willbold, and Wolfgang Hoyer. Opposed Effects of Di-tyrosine Formation in Soluble and Aggregated alpha-Synuclein on Fibril Growth. *Journal of molecular biology*, 429(20):3018–3030, oct 2017.
- [192] Yuichi Yoshimura, Mats A Holmberg, Predrag Kukic, Camilla B Andersen, Alejandro Mata-Cabana, S Fabio Falsone, Michele Vendruscolo, Ellen A A Nollen, and Frans A A Mulder. MOAG-4 promotes the aggregation of alpha-synuclein by competing with self-protective electrostatic interactions. *The Journal of biological chemistry*, 292(20):8269–8278, may 2017.
- [193] Alexander K Buell, Celine Galvagnion, Ricardo Gaspar, Emma Sparr, Michele Vendruscolo, Tuomas P J Knowles, Sara Linse, and Christopher M Dobson. Solution conditions determine the relative importance of nucleation and growth processes in alpha-synuclein aggregation. *Proceedings of the National Academy of Sciences of the United States of America*, 111(21):7671–7676, may 2014.
- [194] Ricardo Gaspar, Georg Meisl, Alexander K Buell, Laurence Young, Clemens F Kaminski, Tuomas P J Knowles, Emma Sparr, and Sara Linse. Secondary nucleation of monomers

on fibril surface dominates alpha-synuclein aggregation and provides autocatalytic amyloid amplification. *Quarterly reviews of biophysics*, 50:e6, jan 2017.

- [195] Celine Galvagnion, Alexander K Buell, Georg Meisl, Thomas C T Michaels, Michele Vendruscolo, Tuomas P J Knowles, and Christopher M Dobson. Lipid vesicles trigger alpha-synuclein aggregation by stimulating primary nucleation. *Nature chemical biology*, 11(3):229–234, mar 2015.
- [196] Robert Vacha, Sara Linse, and Mikael Lund. Surface effects on aggregation kinetics of amyloidogenic peptides. *Journal of the American Chemical Society*, 136(33):11776–11782, aug 2014.
- [197] Jiajie Diao, Jacqueline Burre, Sandro Vivona, Daniel J Cipriano, Manu Sharma, Minjoung Kyoung, Thomas C Sudhof, and Axel T Brunger. Native alpha-synuclein induces clustering of synaptic-vesicle mimics via binding to phospholipids and synaptobrevin-2/VAMP2. *eLife*, 2:e00592, apr 2013.
- [198] Giuliana Fusco, Tillmann Pape, Amberley D Stephens, Pierre Mahou, Ana Rita Costa, Clemens F Kaminski, Gabriele S Kaminski Schierle, Michele Vendruscolo, Gianluigi Veglia, Christopher M Dobson, and Alfonso De Simone. Structural basis of synaptic vesicle assembly promoted by alpha-synuclein. *Nature communications*, 7:12563, sep 2016.
- [199] James W P Brown, Georg Meisl, Tuomas P J Knowles, Alexander K Buell, Christopher M Dobson, and Celine Galvagnion. Kinetic barriers to alpha-synuclein protofilament formation and conversion into mature fibrils. *Chemical communications (Cambridge, England)*, 54(56):7854–7857, jul 2018.
- [200] Matthew Johnson, Arthur T Coulton, Michael A Geeves, and Daniel P Mulvihill. Targeted amino-terminal acetylation of recombinant proteins in *E. coli*. *PLoS one*, 5(12):e15801, dec 2010.
- [201] Venu M Nemani, Wei Lu, Victoria Berge, Ken Nakamura, Bibiana Onoa, Michael K Lee, Farrukh A Chaudhry, Roger A Nicoll, and Robert H Edwards. Increased expression of alpha-synuclein reduces neurotransmitter release by inhibiting synaptic vesicle recluster- ing after endocytosis. *Neuron*, 65(1):66–79, jan 2010.
- [202] Igor Dikiy and David Eliezer. N-terminal acetylation stabilizes N-terminal helicity in lipid- and micelle-bound alpha-synuclein and increases its affinity for physiological mem- branes. *The Journal of biological chemistry*, 289(6):3652–3665, feb 2014.
- [203] Giuliana Fusco, Alfonso De Simone, Tata Gopinath, Vitaly Vostrikov, Michele Vendruscolo, Christopher M Dobson, and Gianluigi Veglia. Direct observation of the three regions in alpha-synuclein that determine its membrane-bound behaviour. *Nature communica- tions*, 5:3827, may 2014.

Bibliography

- [204] Elizabeth Rhoades, Trudy F Ramlall, Watt W Webb, and David Eliezer. Quantification of alpha-synuclein binding to lipid vesicles using fluorescence correlation spectroscopy. *Biophysical journal*, 90(12):4692–4700, jun 2006.
- [205] E Jo, J McLaurin, C M Yip, P St George-Hyslop, and P E Fraser. alpha-Synuclein membrane interactions and lipid specificity. *The Journal of biological chemistry*, 275(44):34328–34334, nov 2000.
- [206] Christina R Bodner, Christopher M Dobson, and Ad Bax. Multiple tight phospholipid-binding modes of alpha-synuclein revealed by solution NMR spectroscopy. *Journal of molecular biology*, 390(4):775–790, jul 2009.
- [207] Francois-Xavier Theillet, Andres Binolfi, Beata Bekei, Andrea Martorana, Honor May Rose, Marchel Stuiver, Silvia Verzini, Dorothea Lorenz, Marleen van Rossum, Daniella Goldfarb, and Philipp Selenko. Structural disorder of monomeric alpha-synuclein persists in mammalian cells. *Nature*, 530(7588):45–50, feb 2016.
- [208] Ami Citri and Yosef Yarden. EGF-ERBB signalling: towards the systems level. *Nature reviews. Molecular cell biology*, 7(7):505–516, jul 2006.
- [209] Mark A Lemmon, Joseph Schlessinger, and Kathryn M Ferguson. The EGFR family: not so prototypical receptor tyrosine kinases. *Cold Spring Harbor perspectives in biology*, 6(4):a020768–a020768, apr 2014.
- [210] Natalia Jura, Nicholas F Endres, Kate Engel, Sebastian Deindl, Rahul Das, Meindert H Lamers, David E Wemmer, Xuewu Zhang, and John Kuriyan. Mechanism for activation of the EGF receptor catalytic domain by the juxtamembrane segment. *Cell*, 137(7):1293–1307, jun 2009.
- [211] Parijat Sengupta, Eran Bosis, Esther Nachliel, Menachem Gutman, Steven O Smith, Gyongyi Mihalyne, Irina Zaitseva, and Stuart McLaughlin. EGFR juxtamembrane domain, membranes, and calmodulin: kinetics of their interaction. *Biophysical journal*, 96(12):4887–4895, jun 2009.
- [212] C Cochet, G N Gill, J Meisenhelder, J A Cooper, and T Hunter. C-kinase phosphorylates the epidermal growth factor receptor and reduces its epidermal growth factor-stimulated tyrosine protein kinase activity. *The Journal of biological chemistry*, 259(4):2553–2558, feb 1984.
- [213] R J Davis and M P Czech. Tumor-promoting phorbol diesters cause the phosphorylation of epidermal growth factor receptors in normal human fibroblasts at threonine-654. *Proceedings of the National Academy of Sciences of the United States of America*, 82(7):1974–1978, apr 1985.
- [214] B Friedman, A R Jr Frackelton, A H Ross, J M Connors, H Fujiki, T Sugimura, and M R Rosner. Tumor promoters block tyrosine-specific phosphorylation of the epidermal growth

-
- factor receptor. *Proceedings of the National Academy of Sciences of the United States of America*, 81(10):3034–3038, may 1984.
- [215] Kristina W Thiel and Graham Carpenter. Epidermal growth factor receptor juxtamembrane region regulates allosteric tyrosine kinase activation. *Proceedings of the National Academy of Sciences of the United States of America*, 104(49):19238–19243, dec 2007.
- [216] Xin Li, Yao Huang, Jing Jiang, and Stuart J Frank. ERK-dependent threonine phosphorylation of EGF receptor modulates receptor downregulation and signaling. *Cellular signalling*, 20(11):2145–2155, nov 2008.
- [217] Gang Cai, Liang Zhu, Xing Chen, Kevin Sun, Caini Liu, Ganes C Sen, George R Stark, Jun Qin, and Xiaoxia Li. TRAF4 binds to the juxtamembrane region of EGFR directly and promotes kinase activation. *Proceedings of the National Academy of Sciences of the United States of America*, 115(45):11531–11536, nov 2018.
- [218] Anke Bill, Anton Schmitz, Katharina Konig, Lukas C Heukamp, Jeffrey S Hannam, and Michael Famulok. Anti-proliferative effect of cytohesin inhibition in gefitinib-resistant lung cancer cells. *PloS one*, 7(7):e41179, 2012.
- [219] Tao Pan, Junfeng Sun, Jiyi Hu, Yiwang Hu, Jun Zhou, Zhigang Chen, Dong Xu, Wenhong Xu, Shu Zheng, and Suzhan Zhang. Cytohesins/ARNO: the function in colorectal cancer cells. *PloS one*, 9(3):e90997–e90997, mar 2014.
- [220] Tao Pan, Junfeng Sun, Jun Zhou, Zhixuan Fu, Yiwang Hu, Shu Zheng, and Suzhan Zhang. Function and mode of action of cytohesins in the epidermal growth factor pathway in colorectal cancer cells. *Oncology letters*, 5(2):521–526, feb 2013.
- [221] Amy Doerner, Rebecca Scheck, and Alanna Schepartz. Growth Factor Identity Is Encoded by Discrete Coiled-Coil Rotamers in the EGFR Juxtamembrane Region. *Chemistry & biology*, 22(6):776–784, jun 2015.
- [222] Lijuan He and Kalina Hristova. Consequences of replacing EGFR juxtamembrane domain with an unstructured sequence. *Scientific reports*, 2:854, 2012.
- [223] Mark V Berjanskii and David S Wishart. Unraveling the meaning of chemical shifts in protein NMR. *Biochimica et biophysica acta. Proteins and proteomics*, 1865(11 Pt B):1564–1576, nov 2017.
- [224] Kiattawee Choowongkamon, Cathleen R Carlin, and Frank D Sonnichsen. A structural model for the membrane-bound form of the juxtamembrane domain of the epidermal growth factor receptor. *The Journal of biological chemistry*, 280(25):24043–24052, jun 2005.
- [225] Konstantin S Mineev, Stanislava V Panova, Olga V Bocharova, Eduard V Bocharov, and Alexander S Arseniev. The Membrane Mimetic Affects the Spatial Structure and Mobility

- of EGFR Transmembrane and Juxtamembrane Domains. *Biochemistry*, 54(41):6295–6298, oct 2015.
- [226] S F Betz, A Schnuchel, H Wang, E T Olejniczak, R P Meadows, B P Lipsky, E A Harris, D E Staunton, and S W Fesik. Solution structure of the cytohesin-1 (B2-1) Sec7 domain and its interaction with the GTPase ADP ribosylation factor 1. *Proceedings of the National Academy of Sciences of the United States of America*, 95(14):7909–7914, jul 1998.
- [227] E Mossessova, J M Gulbis, and J Goldberg. Structure of the guanine nucleotide exchange factor Sec7 domain of human arno and analysis of the interaction with ARF GTPase. *Cell*, 92(3):415–423, feb 1998.
- [228] Jad Rouhana, Francois Hoh, Sebastien Estaran, Corinne Henriquet, Yvan Boublik, Aziz Kerkour, Romain Trouillard, Jean Martinez, Martine Pugniere, Andre Padilla, and Alain Chavanieu. Fragment-based identification of a locus in the Sec7 domain of Arno for the design of protein-protein interaction inhibitors. *Journal of medicinal chemistry*, 56(21):8497–8511, nov 2013.
- [229] J Cherfils, J Menetrey, M Mathieu, G Le Bras, S Robineau, S Beraud-Dufour, B Antony, and P Chardin. Structure of the Sec7 domain of the Arf exchange factor ARNO. *Nature*, 392(6671):101–105, mar 1998.
- [230] Jonathan P DiNitto, Anna Delprato, Meng-Tse Gabe Lee, Thomas C Cronin, Shaohui Huang, Adilson Guilherme, Michael P Czech, and David G Lambright. Structural basis and mechanism of autoregulation in 3-phosphoinositide-dependent Grp1 family Arf GTPase exchange factors. *Molecular cell*, 28(4):569–583, nov 2007.
- [231] Khairul Bariyyah Abd Halim, Heidi Koldso, and Mark S P Sansom. Interactions of the EGFR juxtamembrane domain with PIP2-containing lipid bilayers: Insights from multi-scale molecular dynamics simulations. *Biochimica et biophysica acta*, 1850(5):1017–1025, may 2015.
- [232] George Hedger, Mark S P Sansom, and Heidi Koldso. The juxtamembrane regions of human receptor tyrosine kinases exhibit conserved interaction sites with anionic lipids. *Scientific reports*, 5:9198, mar 2015.
- [233] Ryo Maeda, Takeshi Sato, Kenji Okamoto, Masataka Yanagawa, and Yasushi Sako. Lipid-Protein Interplay in Dimerization of Juxtamembrane Domains of Epidermal Growth Factor Receptor. *Biophysical journal*, 114(4):893–903, feb 2018.
- [234] Pablo Sanchez-Gonzalez, Karim Jellali, and Antonio Villalobo. Calmodulin-mediated regulation of the epidermal growth factor receptor. *The FEBS journal*, 277(2):327–342, jan 2010.

-
- [235] Aldino Viegas, Thibault Viennet, and Manuel Etzkorn. The power, pitfalls and potential of the nanodisc system for NMR-based studies. *Biological chemistry*, 397(12):1335–1354, dec 2016.
- [236] Francesc Tebar, Priam Villalonga, Tatiana Sorkina, Neus Agell, Alexander Sorkin, and Carlos Enrich. Calmodulin regulates intracellular trafficking of epidermal growth factor receptor and the MAPK signaling pathway. *Molecular biology of the cell*, 13(6):2057–2068, jun 2002.
- [237] Anton Arkhipov, Yibing Shan, Rahul Das, Nicholas F Endres, Michael P Eastwood, David E Wemmer, John Kuriyan, and David E Shaw. Architecture and membrane interactions of the EGF receptor. *Cell*, 152(3):557–569, jan 2013.
- [238] Erika Kovacs, Julie Anne Zorn, Yongjian Huang, Tiago Barros, and John Kuriyan. A structural perspective on the regulation of the epidermal growth factor receptor. *Annual review of biochemistry*, 84:739–764, 2015.
- [239] Nicholas F Endres, Rahul Das, Adam W Smith, Anton Arkhipov, Erika Kovacs, Yongjian Huang, Jeffrey G Pelton, Yibing Shan, David E Shaw, David E Wemmer, Jay T Groves, and John Kuriyan. Conformational coupling across the plasma membrane in activation of the EGF receptor. *Cell*, 152(3):543–556, jan 2013.
- [240] Lee Ann Cohen, Akira Honda, Peter Varnai, Fraser D Brown, Tamas Balla, and Julie G Donaldson. Active Arf6 recruits ARNO/cytohesin GEFs to the PM by binding their PH domains. *Molecular biology of the cell*, 18(6):2244–2253, jun 2007.
- [241] Daniele Stalder, Helene Barelli, Romain Gautier, Eric Macia, Catherine L Jackson, and Bruno Antonny. Kinetic studies of the Arf activator Arno on model membranes in the presence of Arf effectors suggest control by a positive feedback loop. *The Journal of biological chemistry*, 286(5):3873–3883, feb 2011.
- [242] Ioannis E Michailidis, Radda Rusinova, Anastasios Georgakopoulos, Yibang Chen, Ravi Iyengar, Nikolaos K Robakis, Diomedes E Logothetis, and Lia Baki. Phosphatidylinositol-4,5-bisphosphate regulates epidermal growth factor receptor activation. *Pflugers Archiv : European journal of physiology*, 461(3):387–397, mar 2011.
- [243] Ye Wang, Jing Gao, Xingdong Guo, Ti Tong, Xiaoshan Shi, Lunyi Li, Miao Qi, Yajie Wang, Mingjun Cai, Janguang Jiang, Chenqi Xu, Hongbin Ji, and Hongda Wang. Regulation of EGFR nanocluster formation by ionic protein-lipid interaction. *Cell research*, 24(8):959–976, aug 2014.
- [244] Takeshi Sato, Payal Pallavi, Urszula Golebiewska, Stuart McLaughlin, and Steven O Smith. Structure of the membrane-reconstituted transmembrane-juxtamembrane peptide EGFR(622-660) and its interaction with Ca²⁺/calmodulin. *Biochemistry*, 45(42):12704–12714, oct 2006.

- [245] I G Denisov, Y V Grinkova, A A Lazarides, and S G Sligar. Directed self-assembly of monodisperse phospholipid bilayer Nanodiscs with controlled size. *Journal of the American Chemical Society*, 126(11):3477–3487, mar 2004.
- [246] T K Ritchie, Y V Grinkova, T H Bayburt, I G Denisov, J K Zolnerciks, W M Atkins, and S G Sligar. Chapter 11 - Reconstitution of membrane proteins in phospholipid bilayer nanodiscs. *Methods in enzymology*, 464:211–231, 2009.
- [247] D S Wishart, C G Bigam, J Yao, F Abildgaard, H J Dyson, E Oldfield, J L Markley, and B D Sykes. ^1H , ^{13}C and ^{15}N chemical shift referencing in biomolecular NMR. *Journal of biomolecular NMR*, 6(2):135–140, sep 1995.
- [248] Rochus L.J. Keller. *In The Computer Aided Resonance Assignment Tutorial*. CANTINA Verlag, 2004.
- [249] Frank H Schumann, Hubert Riepl, Till Maurer, Wolfram Gronwald, Klaus-Peter Neidig, and Hans Robert Kalbitzer. Combined chemical shift changes and amino acid specific chemical shift mapping of protein-protein interactions. *Journal of biomolecular NMR*, 39(4):275–289, dec 2007.
- [250] Toshio Yamazaki, Weontae Lee, Cheryl H Arrowsmith, D R Muhandiram, and Lewis E Kay. A Suite of Triple Resonance NMR Experiments for the Backbone Assignment of ^{15}N , ^{13}C , ^2H Labeled Proteins with High Sensitivity. *Journal of the American Chemical Society*, 116(26):11655–11666, dec 1994.
- [251] D S Wishart, B D Sykes, and F M Richards. The chemical shift index: a fast and simple method for the assignment of protein secondary structure through NMR spectroscopy. *Biochemistry*, 31(6):1647–1651, feb 1992.

List of Abbreviations

| | |
|--------------------------------|--|
| ^1H - ^{15}N | Hydrogen-1-Nitrogen-15 (in respect to NMR spectra) |
| 2YT | Yeast extract tryptone medium, double strength |
| AC | Adenylyl cyclase |
| ACTH | Adrenocorticotrophic hormone |
| AFM | Atomic force microscopy |
| AgRP | Agouti-related Peptide |
| α -MSH | alpha-melanocyte-stimulating hormone |
| ARNO | ADP ribosylation factor nucleotide binding-site opener |
| ASP | Agouti signaling protein |
| α Syn | α Synuclein |
| α Syn-LiPs | α Syn-lipid particles |
| CaM | Calmodulin |
| cAMP | Cyclic adenosine monophosphate |
| CD | Circular dichroism |
| CRE | cAMP response element |
| DDM | n-Dodecyl β -D-maltoside |
| DLS | Dynamic light scattering |
| DMPC | 1,2-Dimyristoyl-sn-glycero-3-phosphocholine |
| DMPG | 1,2-Dimyristoyl-sn-glycero-3-phosphorylglycerol |
| DNA | Desoxyribonucleic acid |
| DSS | 4,4-dimethyl-4-silapentanesulfonic acid |
| DTT | Dithiothreitol |
| <i>E. coli</i> | <i>Escherichia coli</i> |
| EDTA | Ethylenediaminetetraacetic acid |
| EGFR | Epidermal Growth Factor |
| EM | Electron microscopy |
| FITR | Fourier transform infrared spectroscopy |
| FRET | Förster resonance energy transfer |
| <i>g</i> | G-force |
| GPCR | G protein-coupled receptor |
| G-protein | Guanine triphosphate binding protein |
| GST | Glutathione S-transferase |
| GTP | Guanosine triphosphate |
| HEK | Human embryonic kidney |
| HEPES | 4-(2-hydroxyethyl)-1-piperazineethanesulfonic acid |
| HSQC | Heteronuclear single quantum coherence (NMR) |
| HTRF | Homogenous Time-Resolved Fluorescence |
| IBMX | 3-isobutyl-1-methylxanthine |
| ICD | Intracellular Domain |

List of Abbreviations

| | |
|--------------------|--|
| IMAC | Immobilized metal ion affinity chromatography |
| IPTG | Isopropyl β -D-1-thiogalactopyranoside |
| JM | Juxtamembrane (segment of EGFR) |
| kDa | Kilodalton |
| LCN2 | Lipocalin 2 |
| M | Molar, mol/l ⁻¹ |
| MC4R | Melanocortin-4 receptor |
| MDS | Microfluidic diffusional sizing |
| MSH | Melanocyte-stimulating hormone |
| MSP | Membrane scaffold protein |
| MST | Microscale Thermophoresis |
| MWCO | Molecular weight cutoff |
| ND | Nanodisc |
| NDP- α -MSH | [Nle 4, D-Phe 7]- α -MSH |
| Ni-NTA | Nickel nitrilotriacetic acid |
| NMR | Nuclear magnetic resonance (spectroscopy) |
| NPY | Neuropeptide Y |
| PCR | Polymerase chain reaction |
| PD | Parkinson's Disease |
| pH | Potentia Hydrogenii |
| PKA | Protein kinase A |
| POMC | Proopiomelanocortin |
| POPC | 1-palmitoyl-2-oleoyl-sn-glycero-3-phosphocholine |
| POPG | 1-palmitoyl-2-oleoyl-sn-glycero-3-phosphoglycerol |
| SDS | Sodium-dodecyl-sulfate |
| SDS-PAGE | Sodium dodecyl sulfate polyacrylamide gel electrophoresis |
| SEC | Size exclusion chromatography |
| Sf9 | <i>Spodoptera frugiperda</i> 9 cell line |
| SMA | Styrene-maleic acid |
| SMALP | SMA-lipid particles |
| SUMO | Small Ubiquitin-like Modifier |
| TEMED | Tetramethylethylenediamin |
| TEV | Tobacco etch virus |
| ThT | Thioflavin T |
| Tnao38 | <i>Trichoplusia ni Ascalapha odorata</i> 38 cell line |
| TOCSY | Total correlation spectroscopy (NMR) |
| Tris-HCl | Tris(hydroxymethyl)aminomethane, adjusted with hydrochloric acid |
| TROSY | Transverse relaxation optimized spectroscopy (NMR) |
| v/v | Volume/volume (ratio) |
| w/v | Weight/volume (ratio) |

Danksagung

Ich möchte mich in erster Linie bei meinem Doktorvater Dr. Manuel Etzkorn bedanken, der mir die Doktorarbeit in seiner Arbeitsgruppe ermöglicht hat. Danke für deine unermüdliche Unterstützung, deine Geduld sowie für eine entspannte und professionelle Arbeitsatmosphäre. Du hattest immer ein offenes Ohr bei Fragen und Problemen und ich bin sehr froh, dich als meinen Betreuer zu haben.

Ich danke Prof. Dr. Karl-Erich Jaeger für die Übernahme der Zweitkorrektur und Prof. Dr. Dieter Willbold, der mir die Möglichkeit gegeben hat, meine Arbeit in seinem Institut durchzuführen. Bei Prof. Dr. Reza Ahmadian möchte ich mich für die Nutzung seiner Räumlichkeiten und für die Unterstützung danken.

Büro 78 möchte ich für die vortreffliche Stimmung danken, ich werde es vermissen, mir mit euch das Büro zu teilen. Anne Pfitzer möchte ich zum einen für das Korrekturlesen und zum anderen für die zahlreichen unterhaltsamen Momente danken. Ich kann mir keine bessere Büronachbarin vorstellen.

Ein großer Dank geht an die gesamte AG Etzkorn und meine Laborkollegen für ihre Unterstützung und viele interessante Diskussionen. Julian Victor, Jan Börggräfe und Thibault Vinnenet, Michael Wördehoff, Shantha Elter und Sabine Schriek danke ich für die tolle Zusammenarbeit und den fruchtbaren wissenschaftlichen Austausch. Rebecca Schlößer, Claire Ortman und Alla Tripailo danke ich für die sehr angenehme Zusammenarbeit während ihrer Bachelorarbeits- bzw. Praktikumszeit.

Ganz besonders möchte ich mich bei meiner Freundin Nina bedanken, die mich jetzt schon seit einigen Jahren in jeder Lebenssituation unterstützt. Danke für dein Verständnis und deine Geduld, was ich besonders gegen Ende dieses Projekts stark in Anspruch genommen habe. Ich danke meiner ganzen Familie, insbesondere Peter und Petra für ihre Unterstützung und die vielen schönen Momente.

Zum Schluss möchte ich allen Mitgliedern des Instituts für Physikalische Biologie für die vielen gemeinsamen Abende, die tolle Atmosphäre und die große Hilfsbereitschaft danken.

Erklärung

Ich versichere an Eides Statt, dass die Dissertation von mir selbständig und ohne unzulässige fremde Hilfe unter Beachtung der „Grundsätze zur Sicherung guter wissenschaftlicher Praxis an der Heinrich-Heine-Universität Düsseldorf“ erstellt worden ist.

Die Dissertation wurde in der vorgelegten oder in ähnlicher Form noch bei keiner anderen Institution eingereicht. Ich habe bisher keine erfolglosen Promotionsversuche unternommen.

Datum, Ort

Marcel Falke